

Experimental Study of the $K^+ \rightarrow \pi^0 \mu^+ \nu_\mu \gamma$ Decay

FUJIWARA, Tsunehiro

Abstract

In the BNL-E787 experiment, the data corresponding to $3.5 \times 10^{11} K^+$ decays at rest were collected in order to study the radiative $K_{\mu 3\gamma}$ decay $K^+ \rightarrow \pi^0 \mu^+ \nu_\mu \gamma$. A total of 9.4×10^4 triggered events were collected, and 40 candidate events remained after imposing all the selection criteria with the background expectation of (16.5 ± 2.7) events. The branching ratio was obtained to be $Br(K^+ \rightarrow \pi^0 \mu^+ \nu_\mu \gamma) = (1.58 \pm 0.46(stat) \pm 0.08(sys)) \times 10^{-5}$ for $E_\gamma > 30$ MeV and $\theta_{\mu\gamma} > 20^\circ$ where E_γ is the energy of the emitted photon and $\theta_{\mu\gamma}$ is the angle between the muon and the photon in the K^+ rest frame, which is consistent with the standard model prediction ($Br = 2.0 \times 10^{-5}$).

Acknowledgments

Firstly, I would like to express gratitude to my former supervisor, Prof. N. Sasao for his helps and support. He always stimulated my interests in particle physics throughout undergraduate and graduate periods. I would like to express great thanks to Prof. T. Nakaya for undertaking supervisor-position in this time of doctorate application.

I am obliged to all the E787/E949 collaborators. In particular, I would like to express appreciation and mourning to deceased Professor emeritus S. Sugimoto, who was one of the spokespersons of the E787/E949 experiments. He offered the opportunity to join the the E787/E949 experiments and always encouraged and supported me. I would like to express special thanks to Prof. T. Komatsubara. I appreciate his continuous advice was crucial for me to finish this analysis and complete this thesis. I would also like to express special thanks to Prof. T. Nomura. I appreciate his patient assistance was also crucial. I would also like to express great thanks to Dr. L.S. Littenberg, Dr. S.H. Kettel, Dr. M.V. Diwan, Dr. G. Redlinger, Dr. R.C. Strand, Dr. J.S. Frank, Prof. D.A. Bryman, Dr. T. Numao, Dr. A. Konaka, Prof. T. Nakano, Prof. T. Sato, Prof. M. Kobayashi, Prof. Y. Yoshimura, Prof. T. Shinkawa, Prof. Y. Tamagawa, Dr. N. Muramatsu, Dr. T. Tsunemi, Dr. T. Yoshioka, Dr. T. Sekiguchi, Dr. K. Mizouchi, and Mr. E. Ohashi for their precious comments and/or helpful suggestions.

I would also like to thank all the members, including staffs, students, and secretaries, in the high energy physics group of the department of physics in Kyoto university, who were sharing same periods with me.

Finally, I would like to express the best gratitude to my parents for their support.

Contents

1	Introduction	1
1.1	Overview	1
1.2	Theoretical description of $K^+ \rightarrow \pi^0 \mu^+ \nu_\mu \gamma$	1
1.3	$K^+ \rightarrow \pi^0 \mu^+ \nu_\mu \gamma$ in Chiral Perturbation Theory	3
1.4	T violation	4
1.5	Experimental status	5
2	BNL-E787 Experiment	7
2.1	E787 Detector System	7
2.1.1	Beamline and Beam Counters	7
2.1.2	Target	10
2.1.3	Drift Chamber	12
2.1.4	Range Stack	13
2.1.5	Barrel Veto	13
2.1.6	Endcap Detector	15
2.2	Trigger	16
2.3	Data Acquisition	17
2.4	Data taking	18
2.5	E787 Monte Carlo simulation (UMC)	19
3	Offline Analysis	20
3.1	Event reconstruction	20
3.1.1	charged track reconstruction	20
3.1.2	photon reconstruction	21
3.1.3	Kinematic fit	24
3.2	Calibration	27
3.2.1	BV visible fraction	27
3.2.2	parameters for BV z-measurement	27
3.2.3	parameters for kinematic fitting	29
3.3	smearing of the observables in Monte Carlo	35
3.3.1	BV energy	35
3.3.2	BV z-offset	35
3.3.3	smearing for charged track	36
4	Event Selection	41
4.1	Primary selection	41
4.2	Selection of muon	42
4.2.1	range-momentum relation cuts	42
4.2.2	$\frac{dE}{dx}$ cut	42

4.3	Selection of photons	43
4.3.1	number-of-photon cut (NG3)	43
4.3.2	Photon timing cut	43
4.3.3	photon veto cuts	44
4.3.4	<i>egcut</i> cut	44
4.3.5	fused cluster cut	47
4.3.6	e^+ bremsstrahlung cut	49
4.4	Kinematic fit	49
4.4.1	$K_{\mu 3\gamma}$ likelihood cut	49
4.4.2	$K_{\mu 3}$ likelihood cut	49
4.5	Cuts after the kinematic fit	51
4.5.1	missing energy cut	51
4.5.2	$M_{\mu\nu}$ cut	51
4.5.3	θ_ν cut	53
4.6	Data reduction	53
4.7	Signal region	53
4.7.1	E_γ cut	53
4.7.2	$\theta_{\mu\gamma}$ cut	53
5	Background expectation	55
5.1	Background sources	55
5.2	$K_{\mu 3}$ background	56
5.3	$K_{\pi 2\gamma}$ background	58
5.4	$K_{e3(\gamma)}$ background	58
5.5	$K_{\pi 3}$ background	60
5.5.1	overview	60
5.5.2	Bifurcation technique	60
5.5.3	Photon inefficiency of the BV	61
5.5.4	Photon inefficiency of the other subsystems	63
5.5.5	Fused cluster in the BV	63
5.5.6	summary of the $K_{\pi 3}$ background	66
5.6	Summary of the background levels	66
6	Sensitivity for $K^+ \rightarrow \pi^0 \mu^+ \nu_\mu \gamma$	67
6.1	Acceptance factors	67
6.2	Accidental loss	69
6.3	K^+ stop efficiency	70
6.3.1	F_s from the $K_{\pi 2\gamma}$ branching ratio	71
6.3.2	F_s from the $K_{\pi 3}$ branching ratio	72
6.3.3	Summary on the K^+ stop efficiency	73
6.4	Summary on the sensitivity	73
7	Signal events	75
8	Systematic uncertainties	80
8.1	visible fraction of the BV	80
8.2	BV z-measurement	82
8.3	BV Z-offset smearing	82
8.4	BV energy smearing	84

8.5	charged track smearing	84
8.6	dE/dx cut in the Range Stack	85
8.7	range-momentum relation cut	86
8.8	e^+ bremsstrahlung cut	87
8.9	photon timing cut	88
8.10	summary	89
9	Discussions	90
10	Conclusion	92
A	Chiral Perturbation Theory	93
B	The $K_{\mu 3\gamma}$ amplitude at $O(p^4)$ in ChPT	95
B.1	Preliminaries	95
B.2	$V_{\mu\nu}^+$	96
B.3	$A_{\mu\nu}^+$	97
B.4	F_{ν}^+	98
C	Beam cuts	99
D	Target cuts	101

List of Figures

1.1	$K_{\mu 3\gamma}$ decay diagrams	2
1.2	Loop diagrams, from $\mathcal{L}^{(2)}$, for $K_{\mu 3}$ at $O(p^4)$ in ChPT. The weak boson W^+ should be connecting to μ^+ and ν_μ . For $K_{\mu 3\gamma}$, the photon should be appended on all charged lines and on all vertices.	4
1.3	Spectra of $K^+ \rightarrow \pi^0 \mu^+ \nu_\mu \gamma$ observables based on ChPT at $O(p^4)$ in this study: muon momentum (top left), cosine of $\theta_{\mu\gamma}$ (top right), E_γ (bottom left), and neutrino energy (bottom right). The unhatched and hatched histograms represent the distributions before and after imposing the conditions $E_\gamma > 30$ MeV and $\theta_{\mu\gamma} > 20^\circ$	5
1.4	Spectra of $K^+ \rightarrow \pi^0 \mu^+ \nu_\mu \gamma$ observables given by Braguta, Likhoded and Chalov in Fig. 3 of [18]; muon momentum (top left), E_γ (top right), pion momentum (bottom left), and cosine of $\theta_{\mu\gamma}$ (bottom right). Though not explicitly described in [18], the conditions $E_\gamma > 30$ MeV and $\theta_{\mu\gamma} > 20^\circ$ should have been imposed.	6
2.1	Side view of the E787 detector	8
2.2	Schematic plan view of the LESB3 beamline, which consisted of two dipole magnets (D1, D2), two separators, and ten quadrupole magnets (Q1, \dots , Q10).	9
2.3	Schematic side view of the upper-half of the E787 detector (left); design of the Čerenkov counter (right).	9
2.4	Schematic view of B4	10
2.5	Cross-sectional view of the kaon stopping target.	11
2.6	Schematic side view of the target, I-counters, and V-counters.	11
2.7	Schematic view of UTC.	12
2.8	Cross-sectional view of the E787 detector.	14
2.9	Cross sectional (left) and schematic (right) views of the CsI endcap calorimeter.	15
2.10	DAQ System in the E787 experiment in 1998.	17
2.11	Range vs momentum distribution of the charged track in the 3γ -trigger data.	18
3.1	Example of the BV clustering	21
3.2	Hit position (z) along the beam axis in the BV; the total length (190 cm) of the BV module is denoted as “L”.	22
3.3	Momentum (left), kinetic energy (middle), and range (right) of the π^+ tracks in the events used for the BV energy calibration. The arrows indicate the region accepted as the π^+ track from $K_{\pi 2}$	27
3.4	π^0 energy calculated from the sum of the energies of two photons (left) and the invariant mass of the two photons (right) from $K_{\pi 2}$. The red lines indicate the nominal values.	28
3.5	Linear fit of the ADC-based and TDC-based z measurements to a BV module (left); x-axis and y-axis are $\frac{1}{2} \log(\frac{A_1}{A_2})$ and $\kappa(T_1 - T_2)/2$, respectively. Distribution of the attenuation length from all the 192 BV modules (right).	29

3.6	Range vs momentum plots of the charged tracks in the sample for tuning kinematic fitting before (top left) and after imposing the selection criteria for $K_{\mu 3}$ (bottom left) and $K_{\pi 3}$ (bottom right) in this section, respectively. In the plot for $K_{\pi 3}$, the condition $P < 133\text{MeV}/c$ is not imposed.	31
3.7	Distributions of stretch functions for the 10 parameters in the kinematic fit on the $K_{\mu 3}$ assumption (from top left to bottom left) and the χ^2 probability distributions from 0 to 1(bottom middle) and from 0.05 to 1(bottom right).	32
3.8	Distributions of stretch functions for the 13 parameters in the kinematic fitting with the $K_{\pi 3}$ assumption (from top left to bottom left) and the χ^2 probability distributions from 0 to 1(bottom middle) and from 0.05 to 1 (bottom right).	33
3.9	$M_{\gamma\gamma}$ distributions of the π^0 from the $K_{\mu 3}$ (left) and $K_{\pi 3}$ (right) events.	34
3.10	χ^2 probability distributions of the Monte Carlo $K_{\pi 2\gamma}$ events by setting the smearing parameters P_{smearing} to 0.001, 0.46, 0.55, and 0.69 (from left to right).	35
3.11	Z position of the photons in BV. Z accuracy for real data (top left), Z accuracy for MC data without smearing (top center), and Z accuracy for MC data after smearing (top right); Z_{TDC} accuracy for real data (middle left), Z_{TDC} accuracy for MC data without smearing (middle center), and Z_{TDC} accuracy for MC data after smearing (middle right); Z_{ADC} accuracy for real data (bottom left), Z_{ADC} accuracy for MC data without smearing (bottom center), and Z_{ADC} accuracy for MC data after smearing (bottom right).	37
3.12	Distribution of stretch functions of the 10 observables (from to left to bottom left) and the χ^2 probability (bottom middle) of the $K_{\mu 3}$ -assumed kinematic fit for Monte Carlo $K_{\mu 3}$ data.	38
3.13	Distribution of stretch functions of the 13 observables (from top left to bottom left) and χ^2 probability (bottom middle) of the $K_{\pi 3}$ -assumed kinematic fit for Monte Carlo $K_{\pi 3}$ data.	39
3.14	Distribution of stretch functions of the 13 observables (from top left to bottom left) and χ^2 probability (bottom middle) of the $K_{\mu 3\gamma}$ -assumed kinematic fit for Monte Carlo $K_{\mu 3\gamma}$ data.	40
4.1	Distributions of the variable dr_ratio in $K^+ \rightarrow \pi^0\mu^+\nu_\mu\gamma$ (left) and in $K^+ \rightarrow \pi^+\pi^0\gamma$ (right) in Monte Carlo.	43
4.2	Distributions of the variable edf for the muon (left) and electron (right) tracks generated by the Monte Carlo simulation.	44
4.3	Photon timing relative to the charged track time Δt_γ in real data (left) and in Monte Carlo (right).	45
4.4	Photon energy versus Z position of the showers in the BV in real data (top left) and Monte Carlo $K^+ \rightarrow \pi^+\pi^0\gamma$ events (top right), where the curves in the plots indicate the cut realized by $egcut > 22\text{MeV}$; distributions of the variable $egcut$ in real data (bottom left) and Monte Carlo (bottom right).	46
4.5	Plots of the variables $DPSQ$ vs $CHKSPZ$ for the $K_{\mu 3\gamma}$ events (left) and $K_{\pi 3}$ background events (right) generated by the Monte Carlo simulation. The events in the red rectangle area ($DPSQ > 30$ and $CHKSPZ < 20$) were selected. The blue rectangle area ($18 < CHKSPZ < 60$ and $DPSQ < 21$) will be used in the $K_{\pi 3}$ background studies to tag the $K_{\pi 3}$ fused-cluster backgrounds.	48
4.6	Distributions of the variable $amings$ in $K^+ \rightarrow \pi^0\mu^+\nu_\mu\gamma$ events (left), and in $K^+ \rightarrow \pi^0e^+\nu_e$ events (right) generated by Monte Carlo simulation.	49
4.7	Distribution of $Prob(\chi^2_{K_{\mu 3\gamma}})$ from the events generated by Monte Carlo simulation	50

4.8	Distributions of $Prob(\chi^2_{K_{\mu 3}})$ for the $K_{\mu 3\gamma}$ events (left) and $K_{\mu 3}$ events (right) generated by Monte Carlo simulation.	50
4.9	Distributions of E_ν from the $K_{\mu 3\gamma}$ events (left) and the $K_{\pi 2\gamma}$ events (right) generated by Monte Carlo simulation.	51
4.10	Distributions of the $M_{\mu\nu}$ from the $K_{\mu 3\gamma}$ events (left) and the $K_{\pi 2\gamma}$ events (right) generated by Monte Carlo simulation	52
4.11	Distribution of E_γ in the $K_{\mu 3\gamma}$ events generated by Monte Carlo simulation.	54
4.12	Distributions of the cosine of $\theta_{\mu\gamma}$ in the $K_{\mu 3\gamma}$ events generated by Monte Carlo simulation.	54
5.1	Momentum distribution of the charged particles from K^+ decays at rest. The solid histogram shows the distribution of the muon from $K_{\mu 3\gamma}$	55
5.2	Δt_γ distributions of the two photons to form the π^0 (left) and of the radiative photon (right) in real data.	56
5.3	Distribution in $\cos \theta_{\mu\gamma}$ vs E_γ of events selected as the $K_{\mu 3}$ -1 backgrounds. The box indicates the signal region.	57
5.4	Missing energy distributions of real data (black) and $K_{\pi 2\gamma}$ (red) and $K_{\pi 3}$ (yellow) Monte Carlo for the charged tracks that satisfied the range-momentum relation of the π^+ . In this plot, the missing energy cut $E_\gamma < 60$ MeV was not applied	58
5.5	Range vs momentum plot of the charged tracks selected as the e^+ track events (left); distribution of the variable edf used in the dE/dx cut for the e^+ track events (right).	59
5.6	Pictorial explanation of the bifurcation method.	61
5.7	Bifurcation chart for the $K_{\pi 3}$ background through the inefficiency of the BV.	62
5.8	Distribution in $\cos \theta_{\mu\gamma}$ vs E_γ of events selected as the $K_{\pi 3}$ BV inefficiency background. The box indicates the signal region.	62
5.9	Bifurcation chart for the $K_{\pi 3}$ background through the inefficiency of the other sub-systems.	64
5.10	Bifurcation chart for the $K_{\pi 3}$ background through the fused cluster in the BV.	65
5.11	Distributions of the missing energy E_ν vs $chkcc1$ (left) and $\cos \theta_{min}$ vs $chkcc1$ (right) in the Monte Carlo $K_{\pi 3}$ events.	65
6.1	Momentum distributions (left): histogram with error (data), red histogram ($K_{\pi 3}$ M.C.), blue histogram ($K_{\pi 2\gamma}$ M.C.), black histogram ($K_{\pi 3}$ M.C. and $K_{\pi 2\gamma}$ M.C. are combined); dr_{π} distribution (right): the region defined by the arrow is the π -band region.	73
7.1	Cosine of $\theta_{\mu\gamma}$ vs E_γ plots of the events with all analysis cuts imposed in real data (left) and in the sample generated by Monte Carlo $K_{\mu 3\gamma}$ simulation (right). The box indicates the signal region.	75
7.2	Distributions of $Prob(\chi^2_{K_{\mu 3\gamma}})$ from the events in the signal region in real data (left) and in the sample generated by Monte Carlo $K_{\mu 3\gamma}$ simulation (right). All selection cuts excepts for the cut $Prob(\chi^2_{K_{\mu 3\gamma}}) > 0.1$ are imposed.	76
7.3	$M_{\gamma\gamma}$ distribution of the π^0 from the events in the signal region in real data (left) and the sample generated by Monte Carlo $K_{\mu 3\gamma}$ simulation (right).	77

7.4	Spectra of the $K_{\mu 3\gamma}$ candidates: E_γ (top left), π^0 energy (top right), E_ν (bottom left), and muon momentum (bottom right). In each plot, the circles with error bars represent the distributions of the 40 events observed in the signal region. The cuts $E_\gamma > 30$ MeV and $E_\nu > 60$ MeV have been imposed in the analysis. The unhatched histograms represents the distribution of the Monte Carlo $K_{\mu 3\gamma}$ events with the central value of the measured branching ratio plus all the background distributions, and should be compared to the circles with error bars.	78
7.5	Missing energy (E_γ) vs range difference (dr_ratio) plots of the events with all analysis cuts imposed in real data (top left), and in the samples generated by Monte Carlo $K_{\pi 2\gamma}$ (top right), $K_{\pi 3}$ (bottom left), and $K_{\mu 3\gamma}$ (bottom right) simulation. Note that the Monte Carlo simulation in not scaled to real data.	79
8.1	Variation in the visible fraction: distributions of the energy sum of the two photons from π^0 in $K_{\pi 2}$ by changing the visible fraction from -2.0% to +2.0% by a 1.0% step.	81
8.2	Variation in the z-offset smearing: distributions of the z-position accuracy. The “Sigma” obtained from the Gaussian fit was monitored by changing the smearing parameter.	83
8.3	edf distributions used in the dE/dx cut: $K_{\mu 3}$ from the real data (left) and Monte Carlo $K_{\mu 3}$ decays (right).	85
8.4	dr_ratio distribution for the muon tracks in real data (left); dr_ratio distribution of muon track in Monte Carlo Data (right).	86
8.5	$amings$ distributions of the electron events in real data (left) and in the Monte Carlo K_{e3} events (right).	87

List of Tables

1.1	$Br(K_{\mu 3\gamma}, E_\gamma > 30 \text{ MeV}, \theta_{\mu^+\gamma} > 20^\circ)$ for different conditions in ChPT.	4
2.1	Monte Carlo production summary	19
3.1	Resolutions on the muon observables assumed in the kinematic fit on the $K_{\mu 3\gamma}$ assumption.	30
3.2	Resolutions on the photon observables assumed in the kinematic fit on the $K_{\mu 3\gamma}$ assumption.	30
4.1	Photon veto requirements.	44
4.2	Data reduction after imposing each of the cuts in this chapter	53
5.1	Expected background levels in the signal region. “Data” and “MC” in the right-most column indicate whether real data or Monte Carlo simulation were used for the estimation, respectively.	66
6.1	Acceptance factors for the muon trigger component based on Monte Carlo simulation.	67
6.2	Acceptance factors for the photon trigger component based on Monte Carlo simulation.	67
6.3	Acceptance factors for the primary selection based on Monte Carlo simulation.	68
6.4	Acceptance factors for the selection of muon and photons based on Monte Carlo simulation.	68
6.5	Acceptance factors for the kinematic fit based on Monte Carlo simulation.	69
6.6	Acceptance factors for the cuts after the kinematic fit based on Monte Carlo simulation.	69
6.7	Acceptance factors for the signal region based on Monte Carlo simulation.	70
6.8	Acceptance factors for the primary selection based on the data sample of $K^+ \rightarrow \mu^+ \nu_\mu$ decays.	70
6.9	Acceptance factors for the accidental loss based on the data samples of $K_{\mu 2}$ decays and scattered beam pions, respectively.	70
6.10	Data reduction and acceptance factors for the $K_{\pi 2\gamma}$ measurement.	72
6.11	Acceptance factors for the $K_{\mu 3\gamma}$ decay in the kinematic region $E_\gamma > 20 \text{ MeV}$	74
8.1	systematic error evaluation related to visible fraction in the BV	80
8.2	Systematic uncertainty related to the z measurement in the BV	82
8.3	Systematic uncertainty related to the z-offset smearing in the Z measurement in the BV.	82
8.4	Systematic uncertainty related to the photon energy smearing parameter of the BV	84
8.5	Systematic uncertainty related to the charged track smearing parameter	84
8.6	Systematic uncertainty related to the dE/dx cut.	85

8.7	Systematic uncertainty related to the cut position of the muon band.	86
8.8	Systematic uncertainty related to the range-momentum relation cut	86
8.9	Systematic uncertainty related to amings cut	87
8.10	photon timing cut position:	88
8.11	Systematic uncertainty related to the photon timing	88
8.12	Summary of systematic uncertainties in the sensitivities.	89
B.1	Coefficients for loop integrals	96

Chapter 1

Introduction

1.1 Overview

In the energy region below 1 GeV, perturbative method of QCD cannot well be applied to the strong interactions of mesons. Chiral Perturbation Theory (ChPT) [1, 2, 3, 4], in which the quark fields are represented instead by the pseudoscalar-meson fields and the Lagrangian is constructed based on chiral symmetry and with the interactions of Nambu-Goldstone bosons, is an effective-field approach to QCD in the low energy region. Using this theory, decay diagrams involving kaons and pions can be calculated [5, 6, 7].

The decay $K^+ \rightarrow \pi^0 \mu^+ \nu_\mu \gamma$ ($K_{\mu 3\gamma}$) is due to radiative effects in the semi-leptonic transition of $K^+ \rightarrow \pi^0 \mu^+ \nu_\mu$ decay ($K_{\mu 3}$), and is represented in the diagrams in Fig. 1.1. In addition to Internal Bremsstrahlung, which is QED radiative corrections to $K_{\mu 3}$, the decay can proceed via Structure-Dependent radiative decay (SD), which involves the emission of a photon from the intermediate states in the $V-A$ hadronic current from K^+ to π^0 . The decay is dominated by Inner Bremsstrahlung in the kinematic region where the energy of the emitted photon, E_γ , and the opening angle between μ and the photon, $\theta_{\mu\gamma}$, in the K^+ rest frame are small. Thus, lower bounds on E_γ and $\theta_{\mu\gamma}$ are usually imposed.

The first theoretical study of $K_{\mu 3\gamma}$ was made in 1969-70 [8, 9, 10] by using soft-photon theorems [11, 12, 13] and the hypothesis of partially conserved axial-vector current (PCAC). Radiative semi-leptonic kaon decays in ChPT were systematically studied in 1992-93 [14, 15]. The branching ratio for $K_{\mu 3\gamma}$ is predicted to be 2.0×10^{-5} for $E_\gamma > 30$ MeV and $\theta_{\mu\gamma} > 20^\circ$ at $O(p^4)$ in ChPT, and the relative size of SD contribution is around 8 %. No prediction to $K_{\mu 3\gamma}$ has been provided from other strong-interaction theories in the low energy region such as dispersion relations and large-N QCD. We would be able to test ChPT by a measurement of the decay, which is the motivation of the study described in this thesis.

1.2 Theoretical description of $K^+ \rightarrow \pi^0 \mu^+ \nu_\mu \gamma$

For the low energies involved in the semileptonic kaon decays, the momentum dependence of the W-boson propagator connecting to the lepton-neutrino pair in the final state can be neglected and be replaced by the Fermi constant G_F . The matrix element for the decay $K^+(p) \rightarrow \pi^0(p') l^+(p_l) \nu_l(p_n) \gamma(q)$ is written as [14, 15],

$$T = \frac{G_F}{\sqrt{2}} e V_{us}^* \epsilon^\mu(q)^* \left\{ (V_{\mu\nu}^+ - A_{\mu\nu}^+) \times \ell^\nu + F_\nu^+ \times \bar{u}(p_n) \gamma^\nu (1 - \gamma_5) \frac{(m_l - \not{p}_l - \not{q})}{2p_l q} \gamma_\mu \nu(p_l) \right\},$$

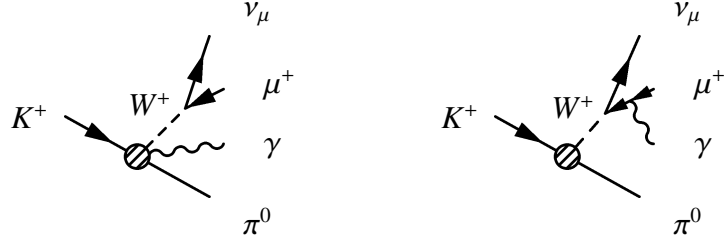


Figure 1.1: $K_{\mu 3\gamma}$ decay diagrams.

where V_{us} is a Kobayashi-Maskawa matrix element that is equal to $\sin \theta_C$ (θ_C : Cabibbo angle) and $\epsilon^\mu(q)$ is the photon polarization vector. The first term corresponds to Fig. 1.1 (left), which includes the Bremsstrahlung off the K^+ ; $V_{\mu\nu}^+$ and $A_{\mu\nu}^+$ are the tensors in the transition from K^+ to π^0 with a photon emission and $\ell^\nu \equiv \bar{u}(p_n)\gamma^\nu(1 - \gamma_5)v(p_l)$ is the leptonic-current vector in the charged weak interaction. The second term corresponds to Fig. 1.1 (right), which is the decay due to the lepton Bremsstrahlung; F_ν^+ is the matrix element for the $K^+ \rightarrow \pi^0 \mu^+ \nu_\mu$ decay and the remaining parts in the second term represent a photon emission from the lepton.

The hadronic tensors $V_{\mu\nu}^+$ and $A_{\mu\nu}^+$ are defined as

$$V_{\mu\nu}^+ = i \int d^4x e^{iqx} \langle \pi^0(p') | T \{ V_\mu^{em}(x) V_\nu^{4-i5}(0) \} | K^+(p) \rangle$$

and

$$A_{\mu\nu}^+ = i \int d^4x e^{iqx} \langle \pi^0(p') | T \{ V_\mu^{em}(x) A_\nu^{4-i5}(0) \} | K^+(p) \rangle ,$$

where

$$\begin{aligned} V_\mu^{4-i5} &\equiv \bar{q}\gamma_\mu \frac{1}{2}(\lambda_4 - i\lambda_5)q = \bar{s}\gamma_\mu u , \\ A_\mu^{4-i5} &\equiv \bar{q}\gamma_\mu \gamma_5 \frac{1}{2}(\lambda_4 - i\lambda_5)q = \bar{s}\gamma_\mu \gamma_5 u , \\ V_\mu^{em} &\equiv \bar{q}\gamma_\mu Qq , \\ Q &\equiv \begin{bmatrix} 2/3 & 0 & 0 \\ 0 & -1/3 & 0 \\ 0 & 0 & -1/3 \end{bmatrix} . \end{aligned}$$

The tensor $V_{\mu\nu}^+$ is further separated into two parts:

$$V_{\mu\nu}^+ = \hat{V}_{\mu\nu}^+ + \frac{p_\mu}{pq} F_\nu^+ ,$$

where the second term corresponds to the Bremsstrahlung off the K^+ . Due to the theorems in radiative corrections, $\hat{V}_{\mu\nu}^+$ is finite for the infrared limit ($q \rightarrow 0$) and is transverse ($q^\mu \hat{V}_{\mu\nu}^+ = 0$), and the axial-vector amplitude $A_{\mu\nu}^+$ is also finite in the infrared limit. Thus, the matrix element for $K_{\mu 3\gamma}$ can be written as:

$$T = \frac{G_F}{\sqrt{2}} e V_{us}^* \epsilon^\mu(q)^* \left\{ (\hat{V}_{\mu\nu}^+ - A_{\mu\nu}^+) \times \ell^\nu + F_\nu^+ \times \bar{u}(p_n)\gamma^\nu(1 - \gamma_5) \left(\frac{p_\mu}{pq} - \frac{(p_l + q - m_l)\gamma_\mu}{2p_l q} \right) v(p_l) \right\} .$$

Explicitly speaking, in the theoretical descriptions of semileptonic kaon decays, the first term in the product of $(\hat{V}_{\mu\nu}^+ - A_{\mu\nu}^+)$ and ℓ^ν is called "Structure Dependent" and the second term proportional to F_ν^+ is called "Inner Bremsstrahlung".

When the photon is on-shell ($q^2 = 0$), Lorentz and parity invariance together with gauge invariance should work and the tensors $\hat{V}_{\mu\nu}^+$, $A_{\mu\nu}^+$ and F_ν^+ are decomposed into:

$$\begin{aligned}\hat{V}_{\mu\nu}^+ &= V_1 \left(g_{\mu\nu} - \frac{W_\mu q_\nu}{qW} \right) + V_2 \left(p'_\mu q_\nu - \frac{p'q}{qW} W_\mu q_\nu \right) + V_3 \left(p'_\mu W_\nu - \frac{p'q}{qW} W_\mu W_\nu \right) + V_4 \left(p'_\mu p'_\nu - \frac{p'q}{qW} W_\mu p'_\nu \right), \\ A_{\mu\nu}^+ &= i\epsilon_{\mu\nu\rho\sigma} (A_1 p'^\rho q^\sigma + A_2 q^\rho W^\sigma) + i\epsilon_{\mu\lambda\rho\sigma} p'^\lambda q^\rho W^\sigma (A_3 W_\nu + A_4 p'_\nu), \\ F_\nu^+ &= C_1 p'_\nu + C_2 (p - p')_\nu,\end{aligned}$$

where $W \equiv (p_l + p_n)$ is equal to $(p - p' - q)$. The four vector amplitudes V_i , the four axial amplitudes A_i , and the two $K_{\mu 3\gamma}$ form factors C_i are functions of scalar variables in the $K_{\mu 3\gamma}$ kinematics, and are Lorentz-invariant and chosen to be real.

The square of the matrix element T , summed over photon and lepton polarization, is necessary to simulate the $K_{\mu 3\gamma}$ decay. FORTRAN computing codes for the calculation, provided in Appendix E of Chapter 3 of the DAΦNE Physics Handbook [5], were used.

In the kinematic region of small photon-energy and small $\theta_{\mu\gamma}$ (collinear lepton and photon), the matrix element T is dominated by Inner Bremsstrahlung. In order to enhance the SD contribution and obtain the theoretical information in $(\hat{V}_{\mu\nu}^+ - A_{\mu\nu}^+)$, the branching ratio for $K_{\mu 3\gamma}$ in the kinematic region $E_\gamma > 30$ MeV and $\theta_{\mu\gamma} > 20^\circ$, $Br(K_{\mu 3\gamma}, E_\gamma > 30 \text{ MeV}, \theta_{\mu^+\gamma} > 20^\circ)$, is used in both the theoretical and experimental studies.

1.3 $K^+ \rightarrow \pi^0 \mu^+ \nu_\mu \gamma$ in Chiral Perturbation Theory

The essential features of ChPT needed for studying kaon decays [16] are summarized in Appendix A.

To the leading order in ChPT, at $O(p^2)$ where p represents the external momenta of Nambu-Goldstone bosons, the diagrams are from the lowest order Lagrangian $\mathcal{L}^{(2)}$ at the tree level of the meson fields. The tensors $V_{\mu\nu}^+$, $A_{\mu\nu}^+$, and F_ν^+ are [7, 14]:

$$\begin{aligned}V_{\mu\nu}^+ &= \frac{1}{\sqrt{2}} \left[g_{\mu\nu} + \frac{(p' + W)_\mu (2p' + W)_\nu}{pq} \right], \\ A_{\mu\nu}^+ &= 0, \\ F_\nu^+ &= \frac{1}{\sqrt{2}} (p + p')_\nu.\end{aligned}$$

$V_{\mu\nu}^+$ is not equal to $\frac{p_\mu}{pq} F_\nu^+$, which implies that the SD contribution to $K_{\mu 3\gamma}$ exists at $O(p^2)$ in ChPT. $Br(K_{\mu 3\gamma}, E_\gamma > 30 \text{ MeV}, \theta_{\mu^+\gamma} > 20^\circ)$ is predicted to be 1.9×10^{-5} .

To the next-to-leading order in ChPT, at $O(p^4)$, there are three types of contributions: (1) $\mathcal{L}^{(2)}$ and the higher-order Lagrangian $\mathcal{L}^{(4)}$ at the tree level, (2) chiral-anomaly \mathcal{L}_{anom} to $A_{\mu\nu}^+$, and (3) $\mathcal{L}^{(2)}$ at the loop level. The loop diagrams at $O(p^4)$ in ChPT are shown in Fig. 1.2. The tensors $V_{\mu\nu}^+$, $A_{\mu\nu}^+$, and F_ν^+ , calculated by Bijmens, Ecker and Gasser in [14, 15], are summarized in Appendix B. $V_{\mu\nu}^+$ depends on the coupling constants L_9 and L_{10} (and mostly on L_9) in $\mathcal{L}^{(4)}$. $Br(K_{\mu 3\gamma}, E_\gamma > 30 \text{ MeV}, \theta_{\mu^+\gamma} > 20^\circ)$ is predicted to be 2.1×10^{-5} when the contribution of the loop diagrams was neglected, and to be 2.0×10^{-5} with the full $O(p^4)$ amplitude. The theoretical predictions are summarized in Table.1.1. The ChPT effects of $O(p^4)$ is non-trivial but, to obtain the information on the coupling constants and the loop effects in ChPT, a precise measurement should be made.

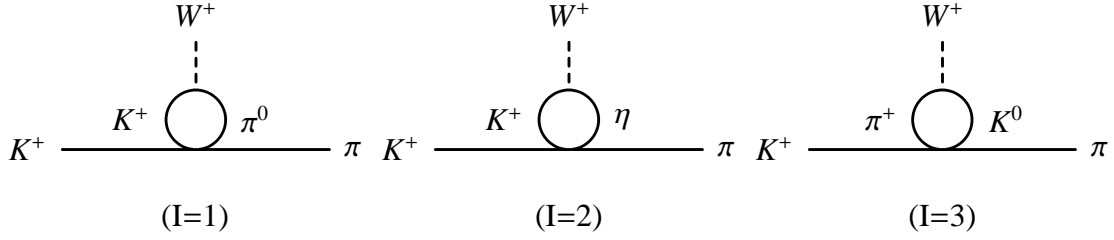


Figure 1.2: Loop diagrams, from $\mathcal{L}^{(2)}$, for $K_{\mu 3}$ at $O(p^4)$ in ChPT. The weak boson W^+ should be connecting to μ^+ and ν_μ . For $K_{\mu 3\gamma}$, the photon should be appended on all charged lines and on all vertices.

			Branching ratio
leading order (LO)	$O(p^2)$	$\mathcal{L}^{(2)}$ -tree	1.9×10^{-5}
next-to-LO, partial	$O(p^4)$ without loop	$\mathcal{L}^{(2)}$ -tree, $\mathcal{L}^{(4)}$ -tree, \mathcal{L}_{anom}	2.1×10^{-5}
next-to-LO	full $O(p^4)$ amplitude	$\mathcal{L}^{(2)}$ -tree, $\mathcal{L}^{(4)}$ -tree, \mathcal{L}_{anom} , $\mathcal{L}^{(2)}$ -loop	2.0×10^{-5}

Table 1.1: $Br(K_{\mu 3\gamma}, E_\gamma > 30 \text{ MeV}, \theta_{\mu^+\gamma} > 20^\circ)$ for different conditions in ChPT.

The tensors to be used for the square of the matrix element T in the FORTRAN codes were extracted by using *Mathematica*, a computer algebra system. The spectra of $K_{\mu 3\gamma}$ observables based on ChPT at $O(p^4)$ are shown in Fig. 1.3¹. It was confirmed that the $K_{\mu 3\gamma}$ spectra generated by the codes are consistent with the spectra in $E_\gamma > 30 \text{ MeV}$ and $\theta_{\mu\gamma} > 20^\circ$ given by different authors (Fig. 3 in “T-odd correlation in the $K_{\mu 3\gamma}$ decay” by Braguta, Likhoded and Chalov [18], reproduced in Fig. 1.4).

1.4 T violation

Another topic concerning the physics of $K^+ \rightarrow \pi^0 \mu^+ \nu_\mu \gamma$ is the violation of time reversal (T-violation), which can be tested by a T-odd observable $\xi \equiv P_\gamma \cdot (P_\mu \times P_\pi)/M_K^3$ [19]. The asymmetry of ξ is defined as $A_\xi \equiv \frac{N_+ - N_-}{N_+ + N_-}$, where N_+ and N_- are the numbers of decay with $\xi > 0$ and $\xi < 0$, respectively. At the tree level there are no T-odd contributions. A_ξ is expected to be 1.14×10^{-4} due to the electromagnetic final state interactions at the level of one-loop diagrams within the standard model [18].

The model-independent Lagrangian of the four-fermion interaction can be expressed as

$$\begin{aligned}
L = & \frac{G_F}{\sqrt{2}} \sin \theta_c [\bar{s} \gamma^\alpha (1 - \gamma_5) u \bar{\nu} \gamma_\alpha (1 - \gamma_5) l + g_s \bar{s} u \bar{\nu} (1 + \gamma_5) l + g_p \bar{s} \gamma_5 u \bar{\nu} (1 + \gamma_5) l \\
& + g_v \bar{s} \gamma^\alpha u \bar{\nu} \gamma_\alpha (1 - \gamma_5) l + g_a \bar{s} \gamma^\alpha \gamma_5 u \bar{\nu} \gamma_\alpha (1 - \gamma_5) l],
\end{aligned}$$

where θ_c is the Cabibbo angle, and g_s , g_p , g_v , and g_a are the scalar, pseudoscalar, vector, and pseudovector constants, respectively. Using this Lagrangian, the matrix element for $K^+ \rightarrow \pi^0 \mu^+ \nu_\mu \gamma$ T is obtained. Integrating $|T|^2$ in the kinematical region of $E_\gamma > 30 \text{ MeV}$ and $\theta_{\mu\gamma} > 20^\circ$, the

¹The effect of the lower bound on $\theta_{\mu\gamma}$ is not significant; this condition is indispensable in the study of the $K^+ \rightarrow \pi^0 e^+ \nu_e \gamma$ decay [17].

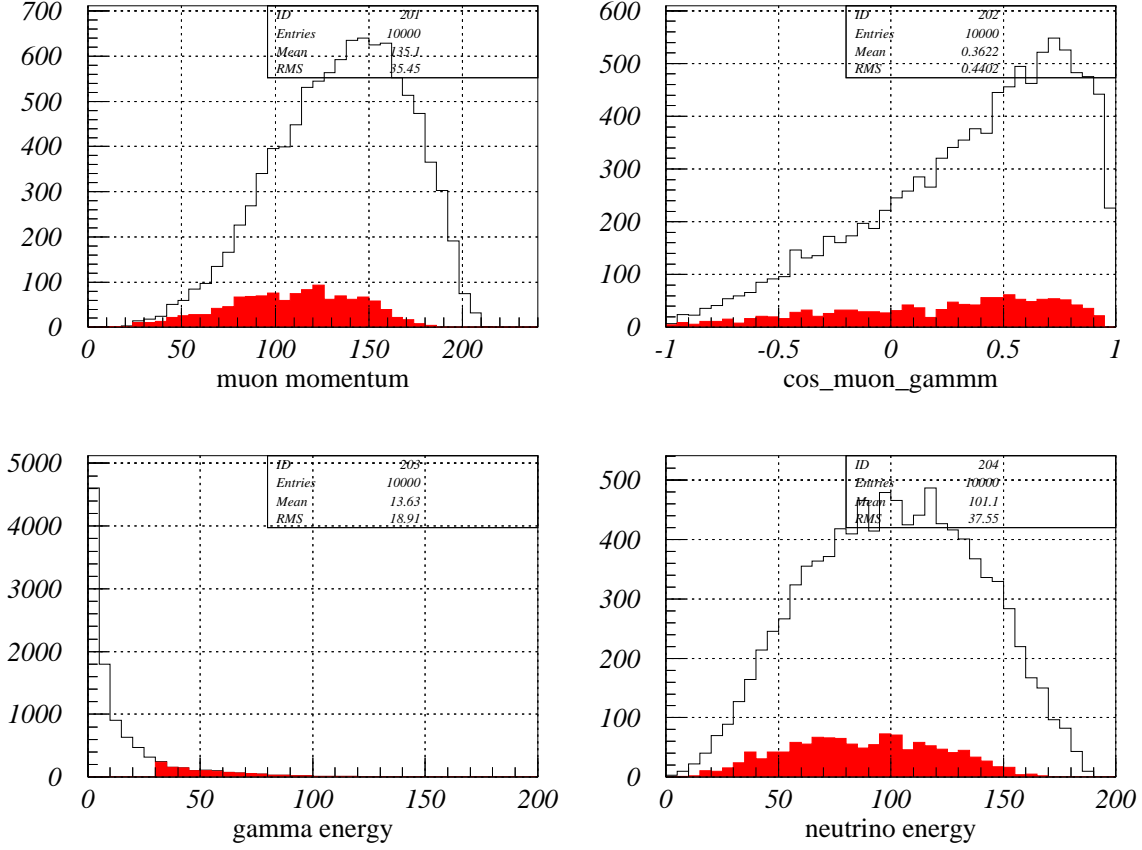


Figure 1.3: Spectra of $K^+ \rightarrow \pi^0 \mu^+ \nu_\mu \gamma$ observables based on ChPT at $O(p^4)$ in this study: muon momentum (top left), cosine of $\theta_{\mu\gamma}$ (top right), E_γ (bottom left), and neutrino energy (bottom right). The unhatched and hatched histograms represent the distributions before and after imposing the conditions $E_\gamma > 30$ MeV and $\theta_{\mu\gamma} > 20^\circ$.

following asymmetry is obtained;

$$A_\xi = -[3.6 \times 10^{-3} \text{Im}(g_s) + 1.2 \times 10^{-2} \text{Im}(g_p) + 1.0 \times 10^{-2} \text{Im}(g_v + g_a)].$$

As an example of the physics beyond the standard model, in the extensions based on the $SU(2)_L \times SU(2)_R \times U(1)$ gauge group in which each generation of fermions is formed in $SU(2)_L \times SU(2)_R$ doublets, the upperbound on the A_ξ is estimated to be 2.6×10^{-4} [20]. Although this upper-limit is comparable to the asymmetry within standard model, T-violation measurement will give restrictions on new physics. Unfortunately, the current experimental sensitivity does not allow us to study the T-violation in the $K^+ \rightarrow \pi^0 \mu^+ \nu_\mu \gamma$ decay.

1.5 Experimental status

The first experimental search for $K^+ \rightarrow \pi^0 \mu^+ \nu_\mu \gamma$ was performed by a heavy-liquid bubble-chamber experiment with K^+ decays at rest in 1973, and an upper limit $Br(K_{\mu 3 \gamma}, E_\gamma > 30 \text{ MeV}) < 6.1 \times 10^{-5}$

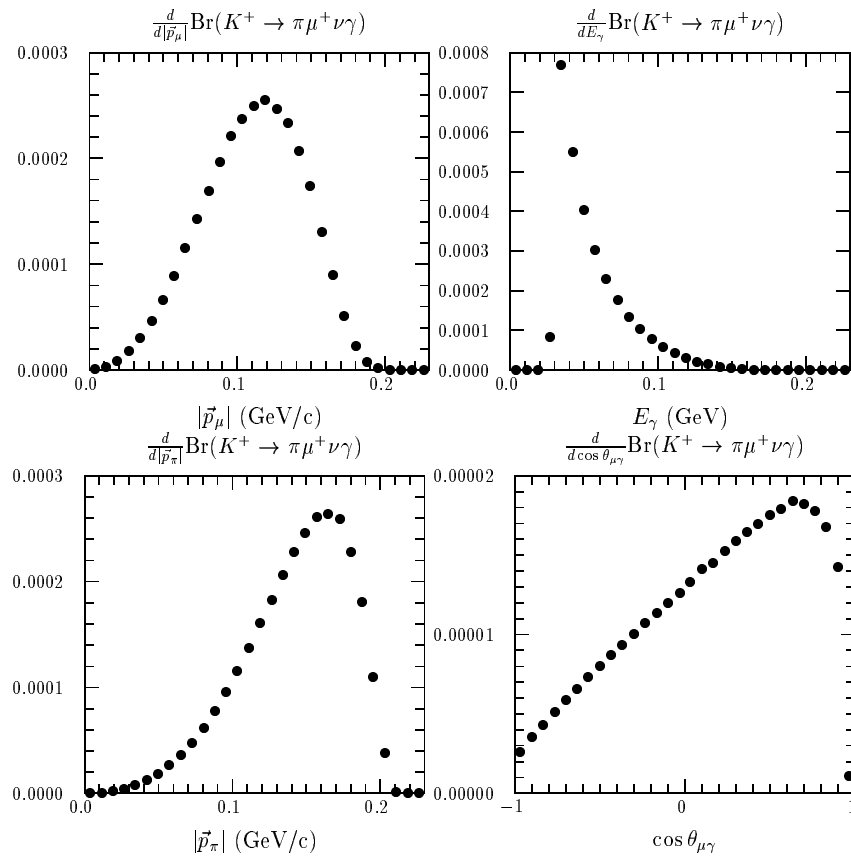


Figure 1.4: Spectra of $K^+ \rightarrow \pi^0 \mu^+ \gamma \gamma$ observables given by Braguta, Likhoded and Chalov in Fig. 3 of [18]; muon momentum (top left), E_γ (top right), pion momentum (bottom left), and cosine of $\theta_{\mu\gamma}$ (bottom right). Though not explicitly described in [18], the conditions $E_\gamma > 30\text{MeV}$ and $\theta_{\mu\gamma} > 20^\circ$ should have been imposed.

at the 90% confidence level (C.L.) was reported in [21].

Recently, two experiments reported their measurements. One was the ISTRA+ experiment with K^- decays in flight. The results were [22]

$$\begin{aligned} Br(K_{\mu 3\gamma})/Br(K_{\mu 3}) &= [0.270 \pm 0.029(stat) \pm 0.026(syst)] \times 10^{-2} \quad (5 < E_\gamma < 30 \text{ MeV}), \\ Br(K_{\mu 3\gamma})/Br(K_{\mu 3}) &= [4.48 \pm 0.68(stat) \pm 0.99(syst)] \times 10^{-4} \quad (30 < E_\gamma < 60 \text{ MeV}). \end{aligned}$$

Based on these values, the Particle Data Group cited $Br(K_{\mu 3\gamma}, 30 < E_\gamma < 60 \text{ MeV})$ as $(1.5 \pm 0.4) \times 10^{-5}$ [23].

The other was the E470 experiment at the KEK 12 GeV Proton Synchrotron. The results were [24]

$$Br(K_{\mu 3\gamma}, E_\gamma > 30\text{MeV}, \theta_{\mu^+\gamma} > 20^\circ) = [2.4 \pm 0.5(stat) \pm 0.6(syst)] \times 10^{-5}.$$

These results are consistent with the theoretical expectations in Table 1.1. In ISTRA+, T-odd asymmetry was measured as:

$$A_\xi = -0.03 \pm 0.13.$$

Chapter 2

BNL-E787 Experiment

The measurement of the $K_{\mu 3\gamma}$ decay in this thesis was performed by using the E787 apparatus at the Alternating Gradient Synchrotron (AGS) of Brookhaven National Laboratory (BNL) in the US. The purpose of the BNL-E787 experiment [25, 26] was to study the rare decay $K^+ \rightarrow \pi^+ \nu \bar{\nu}$ with K^+ decay at rest. The main components of the detector (Fig. 2.1) [27] was a spectrometer and an array of plastic scintillation counters, with 2π solid-angle coverage, for measuring the kinematics of charged particles and a hermetic photon-detection system surrounding the kaon stopping target. Inside the iron yoke, 1.0 Tesla magnetic field was made by the solenoidal magnet. The detector subsystems as well as the trigger, data acquisition, and Monte Carlo simulation are explained in the sections of this chapter. Numerical values in this chapter were for the running conditions of the E787 experiment in 1998 used in this analysis. The resolutions of the E787 detector on the muon and photon observables are achieved in the kinematic fit, and are described in Chapter 3.

2.1 E787 Detector System

2.1.1 Beamline and Beam Counters

AGS is a proton synchrotron which utilizes strong focusing by alternating-gradient magnetic fields. AGS was operated in 1998 with the beam intensity of about 40Tp (40×10^{12} protons) per pulse. A half of the protons were delivered to the E787 experiment. The proton beam was accelerated to 24 GeV, and was slow-extracted with the 2.2-second spill length in the beam cycle of 4.2 seconds; thus, the duty factor was $2.2/4.2 = 52\%$.

The slow-extracted proton beam bombarded the kaon production target. The target was made of 6cm-long platinum. The beam channel was designed to collect the particles produced from the target to the 0 degree. Among the secondary particles π^+ was much copious than K^+ ; the beamline named LESB3 was designed to enhance the K^+ to π^+ ratio in the low momentum region. The LESB3 layout is shown in Fig. 2.2 [28], and the beamline provided a flux of 0.5M K^+ /Tp on target. The main feature of LESB3 was double-stage separation with two electrostatic separators; the K/π ratio was improved to be > 3 . From the LESB3, 710 MeV/c K^+ beam was delivered to the E787 detector in 1998. The momentum was chosen so that high beam yield was maintained below the energy threshold of hyperon production in the degrader.

The K^+ beam enter the Čerenkov counter (labeled as Č in Fig. 2.3). In this Čerenkov counter, lucite ($n = 1.49$) was adopted for the radiator and K^+ was discriminated from π^+ by using the difference of the Čerenkov angles. Čerenkov lights emitted from π^+ were trapped inside the radiator by internal total reflection and reached the inner 14 photomultipliers (“pion PMTs”) by conical mirrors, while Čerenkov lights emitted from K^+ went through radiator, reflected at parabolic mirror, and were detected by the outer 14 photomultipliers (“kaon PMTs”). Both pion PMTs and kaon

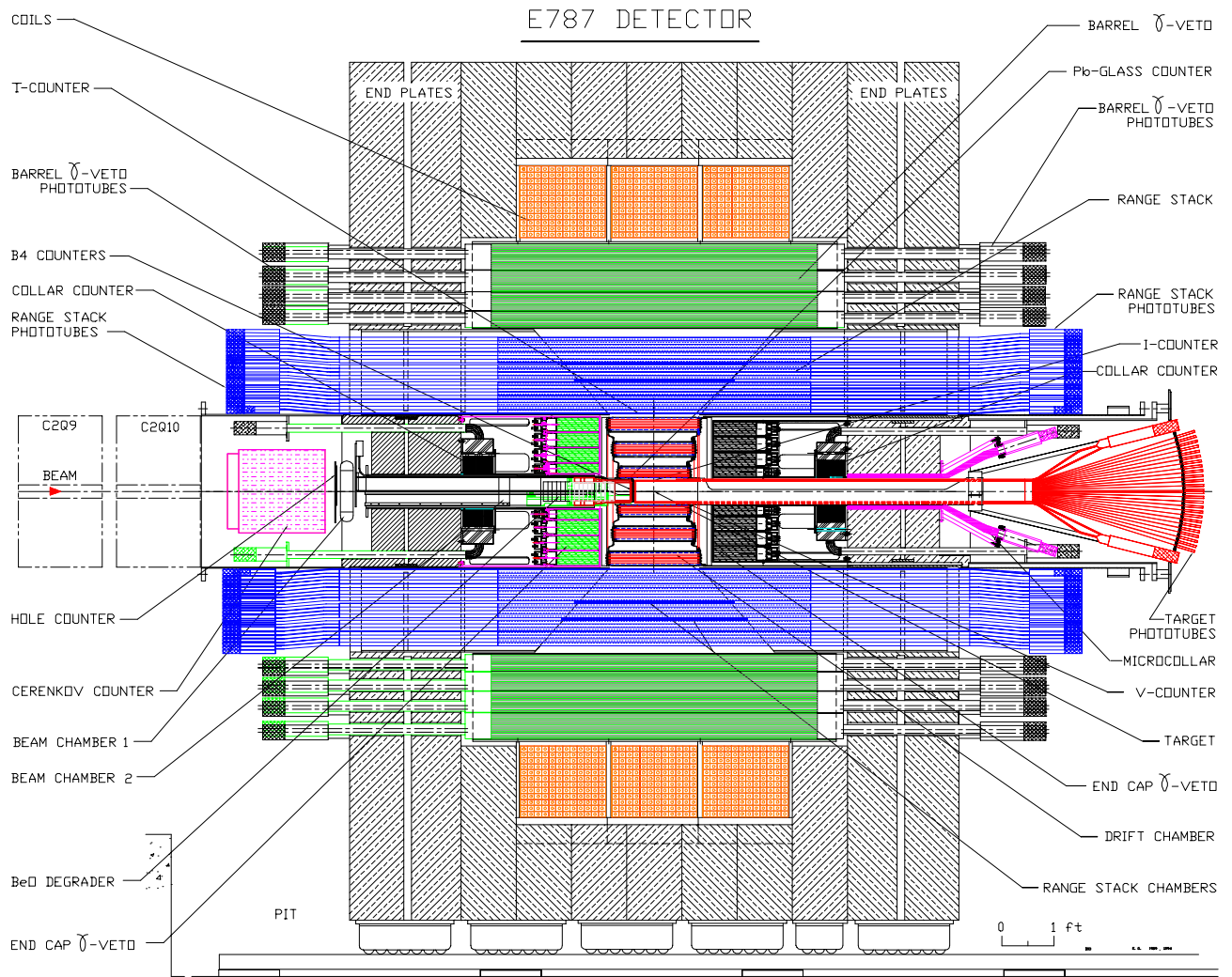


Figure 2.1: Side view of the E787 detector.

PMTs were EMI9945KB. When the number of coincident hits of kaon (pion) PMTs was greater than 5, the particle was identified as kaon (pion).

After the Čerenkov counter, kaons were detected by two sets of multi-wire proportional chambers named as BWPC1 and BWPC2. BWPC1 and BWPC2 were located at 168.5 cm and 68.5 cm, respectively, upstream of the B4 counter. Each of BWPCs has three sense-wire planes. In BWPC1, sense-wires were vertical (x), and $\pm 45^\circ$ (u, v) tilted to the vertical axis; in BWPC2, sense-wires were vertical (x), and $\pm 60^\circ$ (u, v) tilted to the vertical axis. The sense-wires were 12 μm diameter gold-plated tungsten. The cathode foils of BWPC1 (BWPC2) were 25 μm (8 μm single-sided) thick aluminized mylar coated with carbon. The BWPC1 had 144 (x), 60 (u), and 60 (v) readout channels; the BWPC2 had 32 readout channels for each plane. The anode-cathode distance in BWPC1 (BWPC2) was 3.18 mm (1.6 mm). Both BWPC1 and BWPC2 were filled with a recirculated mixture of Tetrafluoromethane (CF_4) (80%) and isobutane (C_4H_{10})(20%). A BWPC hit was reconstructed with coincident hits of the wires in two or three planes. The average time of the hits was used to find an extra particle coming into the detector at the kaon decay time.

After passing through the BWPCs, kaons gradually lost their energy in the degrader and came to rest in the kaon stopping target. The degrader was made of BeO, which was adopted because of its low atomic number and high density. This feature reduced the effects of multiple scattering in the degrader.

After the degrader and just in front the stopping target, the B4 counter was located. B4 con-

sisted of two layers of plastic scintillators, and each layer was divided into 8 “finger” counters in the $\pm 45^\circ$ direction as shown in Fig. 2.4. B4 determined the beam $x - y$ position just before entering the target. Since kaons were slowed down in the degrader, they left more energy than pions in B4. The dE/dx of the particle measured in B4 was used to identify the beam particles.

About 28% of the incident K^+ 's reached the target and satisfied the trigger condition KB (explained in section.2.2(p.16)). The number of KB in the spill was 1.8M (0.8 MHz).

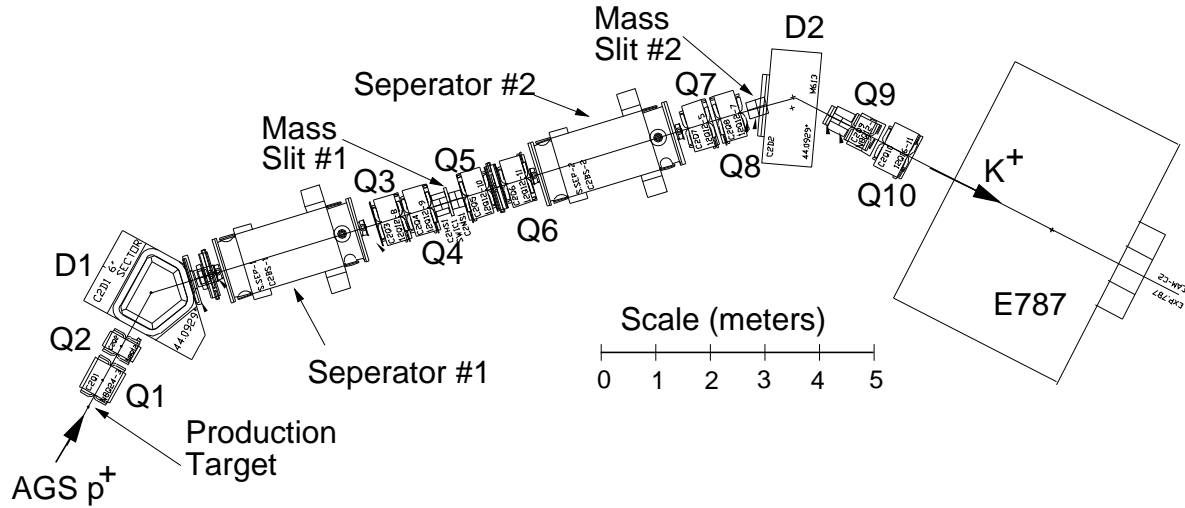


Figure 2.2: Schematic plan view of the LESB3 beamline, which consisted of two dipole magnets (D1, D2), two separators, and ten quadrupole magnets (Q1, \dots , Q10).

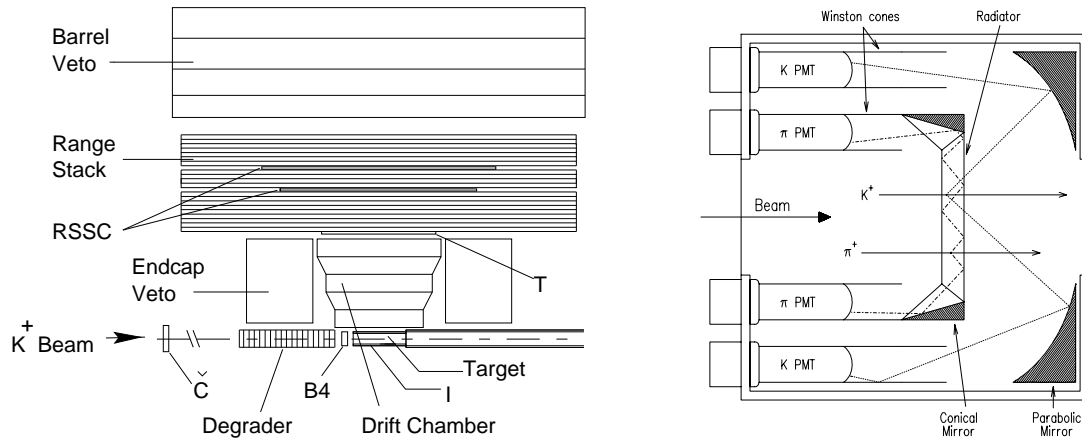


Figure 2.3: Schematic side view of the upper-half of the E787 detector (left); design of the Čerenkov counter (right).

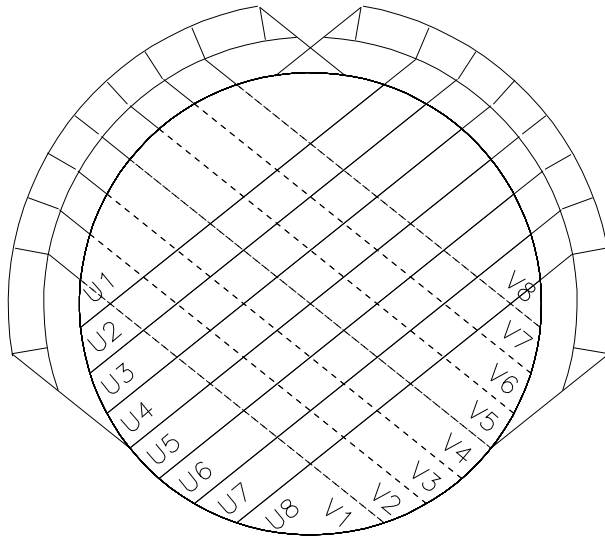


Figure 2.4: Schematic view of B4

2.1.2 Target

The kaon stopping target consisted of a bundle of plastic scintillating fibers (Fig. 2.5). The 413 primary fibers (Bicron BCF10), which were 5 mm squared and 3.1 m long, were stacked to form the main region of the target. The surrounding region was covered by two types of fibers with smaller cross sections so that the target became a 12 cm-diameter cylinder; these fibers were called as “edge fibers”. Each primary fiber was read out at the end by the Hamamatsu R1635-02 photomultipliers (PMTs). The signals from edge fibers were grouped to 16 PMTs. The PMT output signals were fed to ADC, TDC and 500 MHz waveform digitizer based on CCD [29].

The charged particles from the kaon decay at rest passed through a layer of six plastic scintillation counters (6.4 mm thick and 24 cm long) surrounding the target. The counters were named the I-counters (IC), and defined the active volume of the stopping target. The outside of the lightguides of the I-counters was surrounded by the six scintillation counters (5 mm thick and 200 cm long) named the V-counters (VC), which defined the fiducial region of the target in the beam direction as shown in Fig. 2.6. All of the reconstructed events should have an I-counter hit from a charged particle and should not have a V-counter hit. Each counter of IC and VC was read by EMI 9945KB PMT whose signal were fed to ADC, TDC, and 500MHz transient digitizer (TD) [30]. The timing of I-counter hit was also used to ensure K^+ decayed at rest by comparing to the Kaon Čerenkov hit timing at online level.

The target, I-counters and V-counters also worked to detect a part of an electromagnetic shower due to an extra photon from the kaon decay.

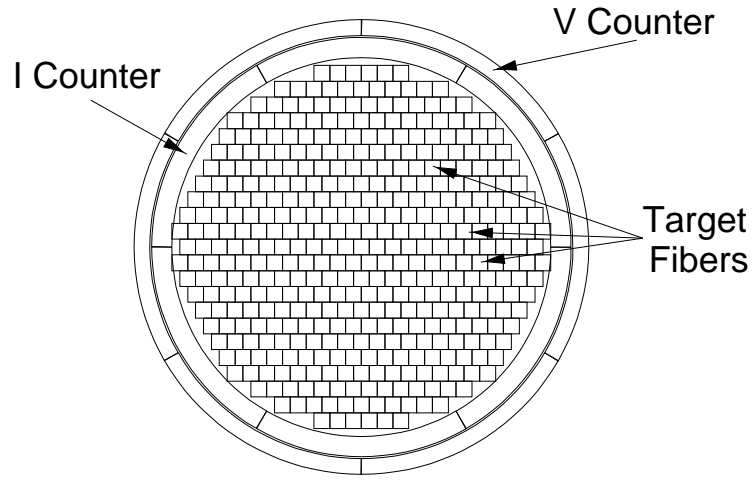


Figure 2.5: Cross-sectional view of the kaon stopping target.

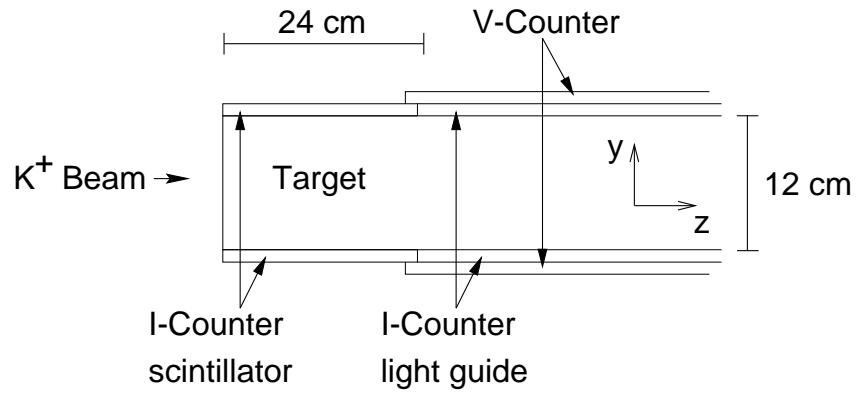


Figure 2.6: Schematic side view of the target, I-counters, and V-counters.

2.1.3 Drift Chamber

The momentum of charged particles was primarily measured by the central drift chamber named Ultra Thin Chamber (UTC) [31]. UTC covered a cylindrical region of 50.8 cm long with the radius of 43 cm, which means 2π solid angle coverage. UTC consisted of five “superlayers”, and each superlayer was separated by a thin Kapton foil. These foils were supported by the difference of gas pressure. The innermost, middle, and outermost superlayers were active regions, in which $20\ \mu\text{m}$ tungsten anode-wires (set at 2 kV) and $100\ \mu\text{m}$ aluminum cathode-wires (grounded) were stretched so that each drift-chamber cell became $11\ \text{mm} \times 19\ \text{mm}$ square. The active superlayers were filled with a 49.8%:49.8%:0.4% mixture of argon, ethane, and ethanol gas, and the inactive superlayers were filled with nitrogen gas. The cell was half shifted in each layer so that the “left-right ambiguity” of a particle passing around the wire was solved. Signals from anode wires were fed to TDC after preamp, and xy-position information was obtained from the timing information. Using the position information in each superlayer, the track on the plane perpendicular to the beam direction (xy-plane) was reconstructed. The Kapton foils had 7mm-wide copper strips and worked as cathode. The strips were tilted by 45 degrees with respect to the beam direction (z-direction), and the positions on the cathode provided the track along the beam direction(rz-plane). The UTC position resolutions were about $175\ \mu\text{m}$ in xy-plane and 1 mm for z. Combining the information in the xy- and rz-planes, the momentum and dip angle of the charged particles were obtained in the offline analysis. The momentum resolution was estimated as 0.9% for μ^+ and π^+ in a range of 150 - 250 MeV/c. The overall mass of UTC amounted to 2×10^{-3} radiation lengths.

E787 Central Tracking Drift Chamber

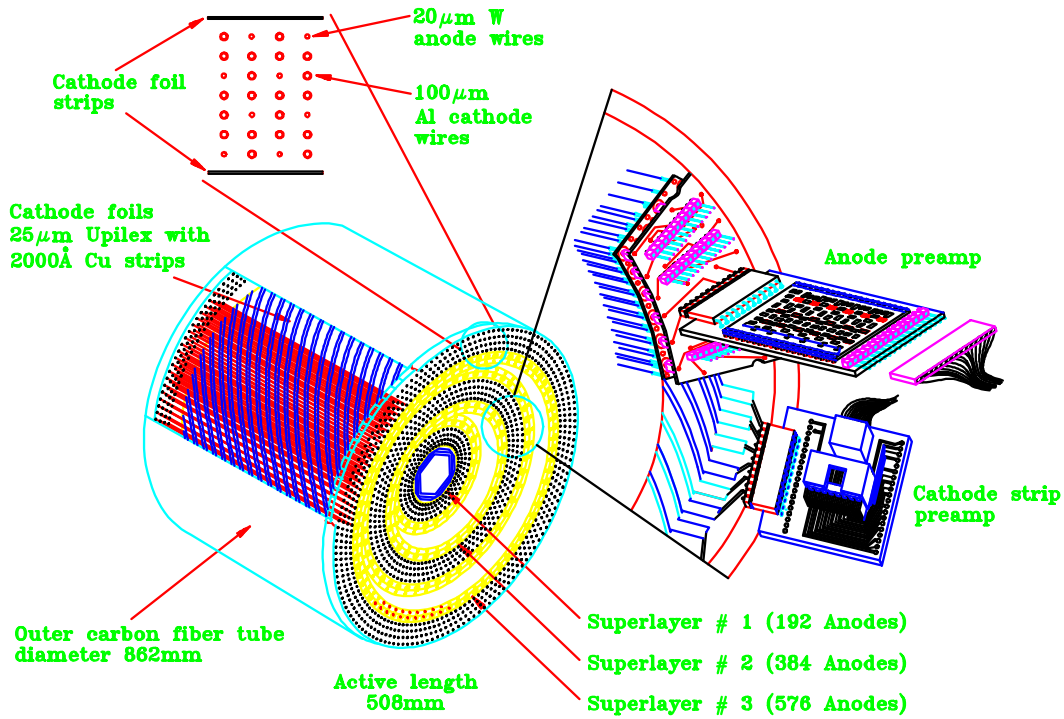


Figure 2.7: Schematic view of UTC.

2.1.4 Range Stack

The range stack (RS) in the E787 detector was an array of plastic scintillators (Bicron BC408) surrounding the UTC region. The charged decay products passed through UTC and lost the energy in the RS. The RS provided a measurement of range and kinetic energy of the charged particle which came to rest in it. The radial region for the RS was segmented into 24 azimuthal sectors and 21 radial layers (Fig. 2.8), totaling one radiation length. The RS counters in the innermost layer (T-counters), which defined the solid angle acceptance for the charged track in the RS, were 0.635 cm thick and 52 cm long. The subsequent RS counters were 1.905 cm thick and 182 cm long. The RS counter where the charged track came to rest was called the “stopping counter.” All the RS counters were read out by EMI 9945KB PMTs on both ends. The output pulse-shapes were recorded by 500MHz-sampling transient digitizers (TDs) [30]; each of TDs was based on two interleaved 250 MHz 8-bit flash ADCs. In addition to providing precise time and energy information for reconstructing the π^+ track, the TDs make it possible to observe the $\pi^+ \rightarrow \mu^+ \rightarrow e^+$ decay chain in the RS stopping counter when the π^+ track identification is needed in the offline analysis for the $K^+ \rightarrow \pi^+ \nu \bar{\nu}$ decay. Two layers of straw-tube tracking chambers were embedded in between the 10th and 11th RS layers and between 14th and 15th RS layers, respectively, but were unused in the $K_{\mu 3\gamma}$ measurement.

2.1.5 Barrel Veto

The “Barrel Veto” photon detector (BV) was a sandwich-type sampling calorimeter with lead and plastic scintillator plates. In total, 96 modules of the BV were installed in the layout of azimuthally-segmented twenty-four sectors divided by four radial layers (Fig. 2.8). Each module was composed of 1mm-thick lead and 5mm-thick plastic scintillator, and the numbers of layers in the module were 16, 18, 23, and 21 for the modules in the same sector. This amounted to 14.5 radiation lengths from the view of the target region. The active length of the scintillators along the beam direction was 190 cm. The gap between any two modules was designed to face away from the target; this configuration was to reduce the photon detection inefficiency due to the gap.

The scintillation light in each module was detected by PMTs (EMI-9821KB) in both ends through the acrylic lightguides. Each signal from the PMT was divided and fed into the discriminator, ADC and the analog fan-in module. The output from the discriminator was send to TDC. The signals from the eight BV modules in the adjacent two sectors were integrated separately for the upstream and downstream ends by the fan-in module to produce their analog sum. The outputs from the analog sum were fed to the discriminator with the energy threshold corresponding to about 5 MeV of visible energy per end. The discriminator outputs were OR-ed for either end, and then fed to the multiplicity logic unit (LeCroy MALU 4413), in which the number of continuous hits of the BV modules was counted online and used for the trigger condition to count the number of electromagnetic showers in the BV. The time resolution of individual BV counter was measured to be 1.2 ns. The energy resolution of BV system was estimated to $\Delta E/E = 1.61/\sqrt{E(\text{MeV})}$.

In the $K_{\mu 3\gamma}$ measurement in this thesis, all of the three photons in the final state from the decay were detected in the BV. The events in which the electromagnetic shower of a photon started before reaching the BV (e.g. within in the RS) were removed by the trigger and the offline analysis.

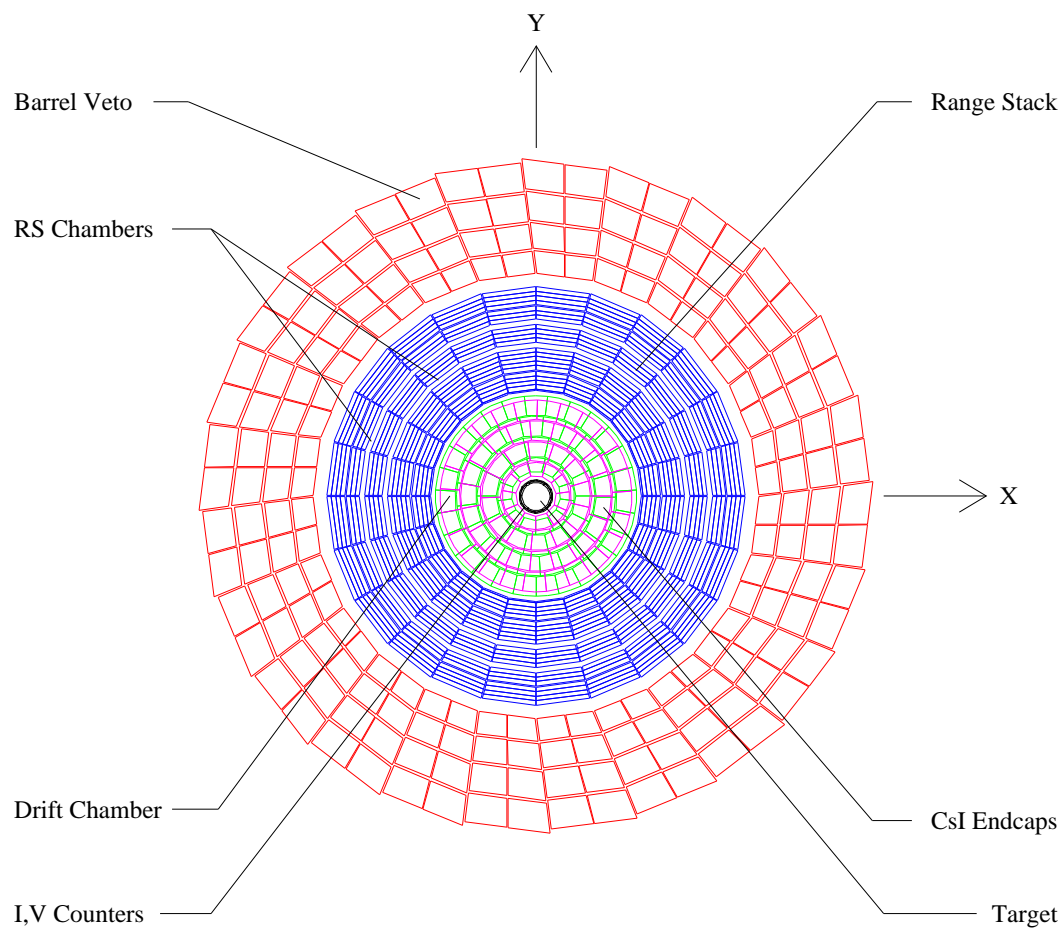


Figure 2.8: Cross-sectional view of the E787 detector.

2.1.6 Endcap Detector

Two endcap calorimeters [32] and additional calorimeters for filling minor openings along the beam direction (collar counters, micro-collar counters, and beam hole counters) were used for detecting extra particles including photons. The two endcaps consisted of undoped CsI crystals, which was 25cm-long (13.5 radiation lengths) and whose cross section was pentagonal. They formed four rings around the beam axis (Fig. 2.9); seventy-five and sixty-eight crystals were used for the upstream and downstream endcaps, respectively. The crystals were directly coupled by 2-inch and 3-inch fine mesh PMTs (Hamamatsu R5543 (3inch) and R5545 (2inch)) [33] through a Sylgrad cookie and UV transmitting optical filter. This filter passed the fast component of the CsI scintillation light exclusively. Fine mesh PMTs were used in order to maintain the high gain in the 1.0 Tesla magnetic field. The signals from PMTs were fed to ADC, CFD (Constant Fraction Discriminator) to TDC, and 500-MHz CCD-based waveform digitizers as in the readout of the target. The OR of the output signals from CFD, whose threshold was 20 MeV, was used for the photon veto in the trigger (*EC* (section2.2)).

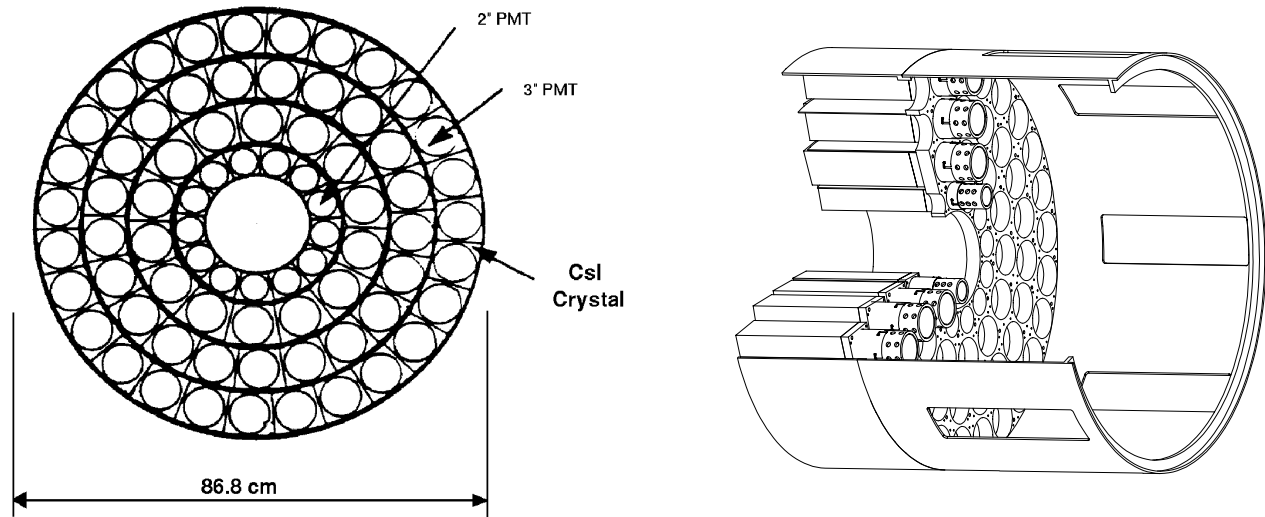


Figure 2.9: Cross sectional (left) and schematic (right) views of the CsI endcap calorimeter.

2.2 Trigger

Several trigger conditions were designed for the purposes of selecting specific decay modes, calibrating detector subsystems, doing acceptance studies, and so on. In the later part of the 1998 run, a new physics trigger named as “ 3γ trigger” was implemented for the study of radiative K^+ decays including $K_{\mu 3\gamma}$. The definition was represented as:

$$3\gamma \equiv KB \cdot DC \cdot T\bullet 2 \cdot (3_{ct} + 4_{ct}) \cdot \overline{(7_{ct} + 8_{ct})} \cdot \overline{(9 + \dots + 21)} \cdot \overline{EC} \cdot HEX \cdot NG3 \cdot prescale.$$

Each term corresponds to the logical condition determined by the corresponding detector subsystem. The symbol “ \cdot ” means the logical product, and the symbol “ $+$ ” used in the $3_{ct} + 4_{ct}$ and $(9 + \dots + 21)$ means the logical sum. The overline used in $\overline{(7_{ct} + 8_{ct})}$, $\overline{(9 + \dots + 21)}$ and \overline{EC} means inversion. These logical operations are realized on the trigger board.

KB means the Kaon Beam condition and was defined as the logical product of Kaon Čerenkov (CK), B4 counter (B4), the target (TTsum), and the spill gate. The definition can be translated as “during the beam spill time, a kaon goes through the Čerenkov counter and the B4 counter, and then stops in the target”. DC means the Delayed Coincidence and was satisfied when the hit timing of I-counter was at least 2nsec later than the kaon beam timing determined by the Čerenkov counter. $T\bullet 2$ means the coincidence of hits of the T-counter and layer 2 counter in the same sector of RS. “ $(3_{ct} + 4_{ct}) \cdot \overline{(7_{ct} + 8_{ct})}$ ” in the trigger means that only tracks for which the RS stopping counter was located in the 3rd to the 6th layer, corresponding to the muons with momentum in 100-160 MeV/c, were accepted. “ n_{ct} ” used in the $3_{ct} + 4_{ct}$ means the hit of the \underline{n} -th RS layer associated with the charged track. The association was satisfied when the sector of the \underline{n} -th layer was in the same or clockwise-next sector of $T\bullet 2$. “ n ” used in the $\overline{(9 + \dots + 21)}$ means the hit of any RS sector in the \underline{n} -th RS layer. Thus, $\overline{(9 + \dots + 21)}$ means that no energy larger than the level of minimum ionizing particles was observed from the 9-th to the 21-th layer of the RS at the kaon decay time. EC means the EndCap veto. \overline{EC} assures that no hit more than 20 MeV was observed in the endcap detectors. HEX is called the hextant cut, which was the online photon veto in RS. The twenty-four sectors were beforehand separated into six(hexa-) regions and each region was called as hextant. HEX was true when no activity more than 10 MeV was detected in all hextants except for one or two hextant where the charged track was located. $NG3$ means the BV condition which was satisfied when Number of Gamma counted online was equal to or greater than 3. The number of electromagnetic showers in the BV was counted by the multiplicity logic unit described in Sec. 2.1.5. The prescaler was set to 5 to reduce the trigger rate.

In this analysis, other triggers such as $Kpi2(1)$, $Kpi2(2)$, $Km2(1)$ and $piscat$ were used. These trigger conditions were defined as follows [34], and were also prescaled properly to reduce the trigger rates.

$$\begin{aligned} Kpi2(1) &\equiv KB \cdot T\bullet 2 \cdot (6_{ct} + 7_{ct}) \cdot \overline{(19_{ct} + 20_{ct} + 21_{ct})} \\ Kpi2(2) &\equiv KB \cdot IC \cdot DC \cdot T\bullet 2 \cdot (6_{ct} + 7_{ct}) \cdot \overline{(19_{ct} + 20_{ct} + 21_{ct})} \cdot HEX \cdot L1.1 \cdot L1.2 \\ Kmu2(1) &\equiv KB \cdot T\bullet 2 \cdot (6_{ct} + 7_{ct}) \cdot (19_{ct} + 20_{ct} + 21_{ct}) \\ piscat &\equiv piB \cdot \overline{DC} \cdot IC \cdot T\bullet 2 \cdot (6_{ct} + 7_{ct}) \cdot \overline{(20 + 21)} \cdot \overline{EC + BV} \cdot HEX \end{aligned}$$

piB was satisfied when pion PMTs (instead of the kaon PMTs) in the Čerenkov counter had a hit in the KB definition. $L1.1$ and $L1.2$ were higher level triggers which enabled the π^+ identification in the $Kpi2(2)$ trigger by exploiting $\pi^+ \rightarrow \mu^+$ decay in the RS stopping counter with TD information.

2.3 Data Acquisition

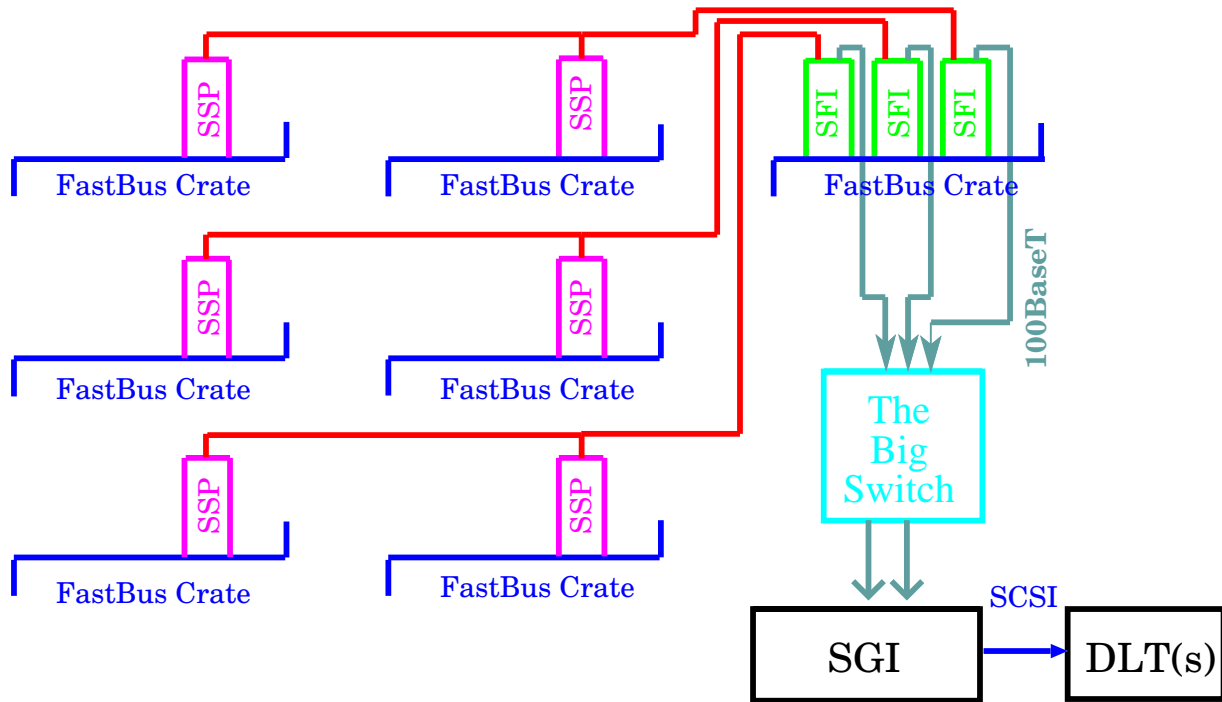


Figure 2.10: DAQ System in the E787 experiment in 1998.

All the modules such as ADC, TDC, TD and CCD were set in the Fastbus crates (Fig. 2.10). The data were stored in SSP (Slac Scanner Processor) in each Fastbus crate. The recorded data were transferred to Struck 340/SFI controller during off spill time. Struck 340 was embedded with VME. The VxWorks on the CPU (Motorola MVME2604) enabled multi-task operation, so that data-collection and data-transfer were performed in the same time. The data were transferred to the workstation (SGI Challenge) via Ethernet (100BaseT) and were recorded to the DLT tapes. The event size was about 100KByte due to the waveform information in TD and CCD.

2.4 Data taking

The 3γ trigger data was taken from September 17 to December 31 in 1998. The number of 3γ trigger events was 9.3836×10^6 , which corresponded to the data size of 1 TByte.

The number of K^+ decay during the running period was 1.7447×10^{12} . Taking into account the prescale factor of 5, the effective number of K^+ decays in this measurement was 3.4894×10^{11} .

The range vs momentum distribution of the charged track in the events obtained by the 3γ trigger is shown in Fig.2.11. The reconstruction of charged track and details of background sources are explained in the forthcoming chapters. It is worth mentioning that the $K^+ \rightarrow \pi^+\pi^0$ ($K_{\pi 2}$) decay cluster had a broad distribution in the range because, in these events, π^+ had nuclear interaction in the RS before losing all the kinetic energy due to minimum-ionization loss with the Bethe-Bloch formula. This phenomenon was unexpectedly large, but was easily removed by requiring that the momentum, which was properly measured in UTC, should be smaller than the monochromatic peak of 205 MeV/c.

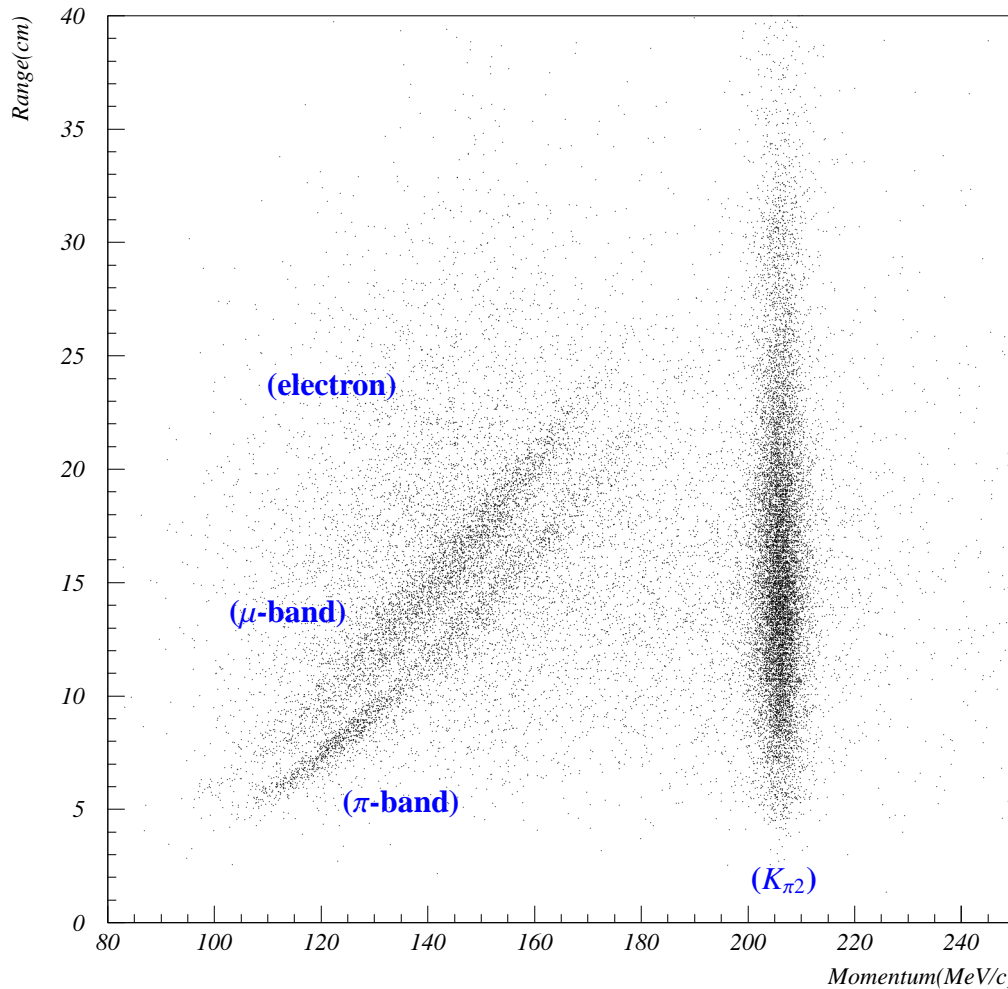


Figure 2.11: Range vs momentum distribution of the charged track in the 3γ -trigger data.

2.5 E787 Monte Carlo simulation (UMC)

The Monte Carlo simulation package (UMC) was developed for the E787 experiment based on EGS4 [35]. Since only the electromagnetic shower simulation is implemented in EGS4, other physics processes such as particle decays and π/μ interactions in the materials were introduced to the EGS4 framework. The energy deposits of a charged track were calculated based on the Bethe-Bloch formula. The resulting scintillation light (and the visible energy) was estimated by the Birk formula, in which the light output L of organic scintillators is described as

$$\frac{dL}{dx} \propto \frac{dE/dx}{1 + k_B dE/dx}$$

with $k_B = 0.01 \text{ g / MeV} \cdot \text{cm}^2$ [36].

In this analysis, several K^+ decay modes were simulated for the acceptance calculation and background estimation. The $K_{\mu 3\gamma}$, $K_{\mu 3}$, $K^+ \rightarrow \pi^0 e^+ \nu_e (K_{e3})$, $K^+ \rightarrow \pi^+ \pi^0 \pi^0 (K_{\pi 3})$, $K^+ \rightarrow \pi^+ \pi^0 \gamma (K_{\pi 2\gamma})$, $K^+ \rightarrow \mu^+ \nu_\mu (K_{\mu 2})$ and $K^+ \rightarrow \pi^+ \pi^0 (K_{\pi 2})$ decays in the E787 detector were generated by UMC.

For three or four body decay, the decay matrix elements should be calculated. The computer codes for the squared matrix element of the $K_{\mu 3\gamma}$ decay were taken from the DAΦNE Physics Handbook [5]. The $K_{\mu 3\gamma}$ Monte Carlo data were generated in the kinematic region $E_\gamma > 20 \text{ MeV}$. For the matrix element of $K^+ \rightarrow \pi^+ \pi^0 \pi^0$, the following formula was used:

$$|M|^2 \propto 1 + g \frac{(s_3 - s_0)}{m_{\pi^+}^2} + h \left[\frac{(s_3 - s_0)}{m_{\pi^+}^2} \right]^2 + k \left[\frac{(s_2 - s_1)}{m_{\pi^+}^2} \right]^2,$$

where $s_i \equiv (P_K - P_i)^2 = (m_K - m_i)^2 - 2m_K T_i$, $s_0 \equiv \frac{1}{3} \sum s_i = \frac{1}{3}(m_K^2 + m_1^2 + m_2^2 + m_3^2)$ and i indicates the i -th pion. π^+ was chosen as the third pion ($i = 3$). The values $g = 0.626$, $h = 0.52$, and $k = 0.0054$ were taken from Reviews of Particle Physics [23].

The total numbers of events in the Monte Carlo production are summarized in Table 2.1.

mode	#generated events	conditions	trigger	resource (CPU TIME)(sec)
$K_{\mu 3\gamma}$	1.0000×10^9	$E_\gamma > 20 \text{ MeV}$	3γ	3.6×10^7
$K_{\mu 3}$	2.9743×10^{10}	nothing	3γ	7.3×10^8
$K_{\pi 3}$	4.300×10^9	nothing	3γ	1.4×10^8
$K_{\pi 2\gamma}(\text{IB})$	3.000×10^9	$20 < T_{\pi^+} < 95 \text{ MeV}$	3γ	1.0×10^8
$K_{\pi 2\gamma}(\text{DE})$	2.500×10^8	$20 < T_{\pi^+} < 95 \text{ MeV}$	3γ	8.7×10^5
K_{e3}	3.910×10^8	nothing	3γ	1.3×10^7
$K_{\mu 2}$	6.0×10^4	nothing	Kmu2(1)	9.1×10^2
$K_{\pi 2}$	1.0×10^5	nothing	Kpi2(1)	2.5×10^3

Table 2.1: Monte Carlo production: “CPU TIME” corresponds to the time consumption with a CPU of Intel(R) Xeon(TM) 2.80GHz enabled hyper-threading.

Chapter 3

Offline Analysis

With the “ 3γ trigger” in E787, we collected the events of the K^+ decay with a charged track of short range in the RS (corresponding to the muons with momentum 100-160 MeV/c) and three photons in the BV detector in the final state. We selected the $K^+ \rightarrow \pi^0 \mu^+ \nu_\mu \gamma$ candidate events from them by several steps of offline analysis, which are described in this chapter.

The system of coordinates of the E787 detector in this analysis was defined as follows. The origin of the coordinates was at the center of the detector. The z axis and y axis were defined along the beam direction and to the vertical direction, respectively. The x axis, in the horizontal direction, was defined so that the system satisfied the right-handed coordination.

3.1 Event reconstruction

3.1.1 charged track reconstruction

The procedure of charged track reconstruction in this analysis is the same as that used in the standard E787 analysis. Three detector subsystems: the target, UTC and RS were used to reconstruct the momentum (P), range (equivalent cm of plastic scintillator, R) and the kinetic energy (T).

The target pattern recognition was made by examining the time, energy and position of the fibers which had both ADC and TDC hits. The “kaon fibers” were determined by selecting the fibers which had larger energy deposit (typically ≥ 4 MeV) at the B4 time and were located beside the extrapolated track from UTC. The kaon decay vertex was determined by taking the kaon fiber that was closest to the extrapolated track; the z coordinate was calculated from the track position at the fiber. The “track fibers” were selected by taking the fibers which had small energy deposit, consistent with minimum ionizing particles, at the time of kaon decay from the μ^+ track in RS and which were located along the extrapolated track.

The UTC track reconstruction was made separately in the xy and rz planes. In the xy plane, a circle was fitted to the positions calculated from the drift distance in each sense-wire hit. In the rz plane, a straight line was fitted by using cathode strip hits, and the polar angle of the charged track was obtained. The momentum in UTC was calculated from the radius of the circle in the xy fit and the polar angle in the rz fit.

The RS counters hit by the charged track was selected from the counters whose timing was closest in time to the online $T \cdot 2$ timing (detector strobe). Starting from the T-counter hit and the 2nd layer counter hit, the RS hit of the outer layer in the same sector was considered to be the next hit of the track. If no hit was found in the same sector, the hit of the same or outer layer and in the adjacent sector (to the clockwise direction, for the transportation of positively charged particle in the magnetic field) was identified as the hit of the same track. If no more hit was found by this algorithm, the last counter was recognized as the RS stopping counter. In order to calculate the

range of a charged track in the RS, the technique of track fitting was adopted. Transportation of a charged track in the RS was simulated with the muon assumption in the $K^+ \rightarrow \pi^0 \mu^+ \nu_\mu \gamma$ analysis, by losing energy with the Bethe-Bloch formula and by bending in the 1 Tesla magnetic field. By varying the momentum and the incident angle of the track at the innermost radius of the RS, track transportation was repeated until the track matched the sector crossing points in the RS and the energy loss in the stopping counter. The χ^2 probability was calculated to evaluate the quality of the fitting. In the rz plane, the agreement between the extrapolated UTC track and z measurements based on the end-to-end time differences in the individual RS counters was evaluated with the χ^2 probability of the sum of residuals.

The momentum measured in UTC was corrected for the energy loss suffered by the charged particle with the observed track length in the target, in order to determine the total momentum P. The total range R was calculated from the track length in the target and in the RS. The track length within the RS stopping counter was measured from the energy deposit in it. The total kinetic energy T was determined by adding up the energy deposits of the charged track in the scintillators of the target and the RS, taking account of the losses in inactive materials such as wrapping and chamber materials.

3.1.2 photon reconstruction

For the $K^+ \rightarrow \pi^0 \mu^+ \nu_\mu \gamma$ analysis, three photons in the final state were detected and measured by the BV, which covered two-thirds of the solid angle. For each BV module, in order to remove the hit-position dependence along the z direction, the energy deposit was determined by the geometrical mean of the energies measured in both ends and the timing was determined by the average of the times in both ends. The energy calibration of the BV hits was performed by using the energy deposits from cosmic-ray muons, and was verified by reconstructing the monochromatic energy (245.6 MeV) of the two photons from π^0 in the $K^+ \rightarrow \pi^+ \pi^0$ decay at rest.

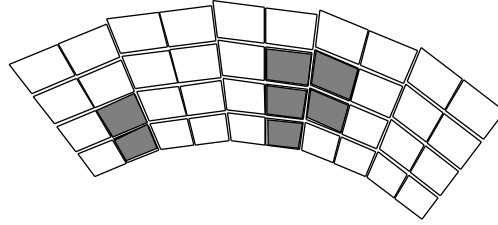


Figure 3.1: Example of the BV clustering: modules in five BV sectors are drawn in the cross-sectional view, and the modules with hits are indicated in gray. Two clusters are observed in this example.

Electromagnetic showers due to the photons spread out in the BV and the energy was recorded in the modules. Thus an algorithm of shower reconstruction (“clustering” in the BV) was necessary. Adjacent hit modules whose visible energy was more than 0.2 MeV and whose timing was within ± 6.0 nsec of the μ^+ track time were grouped into a “cluster” (e.g. Fig. 3.1). The location of the shower (x, y, z) was obtained as

$$x = \frac{\sum E_i x_i}{\sum E_i},$$

where E_i and x_i indicate the energy and the x-coordinate of the i -th module in the cluster, respectively. The y and z coordinates were calculated in the same way. The hit position of each module

in the end view (x_i, y_i) was determined from the center position of the cross section of the module. The hit position along the beam axis (z_i) was calculated from the the energy-weighted mean of the z-measurements with TDCs and ADCs of the PMTs in both ends of the modules:

$$z_i = \frac{z_i^T + z_i^A \sqrt{E_i/10}}{1 + \sqrt{E_i/10}},$$

where z_i^T and z_i^A are the TDC-based and ADC-based z-measurements, respectively.

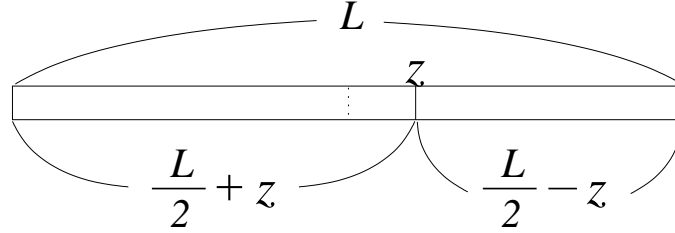


Figure 3.2: Hit position (z) along the beam axis in the BV; the total length (190 cm) of the BV module is denoted as “L”.

For the the TDC-based z measurement, effective speed of scintillation light in the BV module (κ) was needed. Although the speed of light in BV should naively be determined by the refractive index of the material, the speed was affected by the geometry of the module and the path of light to reach the end. Using the notation in Fig. 3.2, the timings of both ends are represented as :

$$\begin{aligned} T_1 &= (L/2 + z)/\kappa, \text{ and} \\ T_2 &= (L/2 - z)/\kappa, \end{aligned}$$

where T_1 and T_2 are obtained from the TDC measurements. The TDC-based z measurement is represented in the following formula with an offset parameter O_T .

$$z^T = \kappa(T_1 - T_2)/2 - O_T$$

For the ADC-based z measurement, attenuation length of scintillation light (λ) was needed. The measured energies in both ends are expressed as follows.

$$\begin{aligned} A_1 &= E \exp\left(-\frac{L/2 + z}{\lambda}\right) \\ A_2 &= E \exp\left(-\frac{L/2 - z}{\lambda}\right) \end{aligned}$$

Thus the ADC-based z -measurement is represented with an offset parameter O_A .

$$z^A = \frac{\lambda}{2} \log(A_1/A_2) - O_A$$

The cluster energy, by the sum of the energy in each module:

$$E_{cluster} = \sum E_i$$

is only a part of the shower energy because the detected energy (“visible energy”) is only the energy loss of the electromagnetic shower in the scintillators. Then the calibration parameter called the

“visible fraction” was introduced. The visible fraction (*VSFR_BV*) was defined as the portion of the energy deposit in the active part of the sampling calorimeter, and was about 0.3 in the BV design with simulations. The true shower energy was measured by dividing the visible energy with the visible fraction:

$$E_\gamma = E_{cluster}/VSFR_BV.$$

The energy calibration of the BV is described in Section 3.2.1.

In the clustering algorithm, if two showers were separated by less than 55 cm and the energy of one of them was less than 25 MeV, they were combined to a single shower. This avoided misidentifying a part of an electromagnetic shower to be a separate one (“photon-splitting” events), although four photons from K_{π^3} might be misidentified as three photons.

The cluster timing was determined by the energy-weighted mean of the timings in the BV modules:

$$t_\gamma = \frac{\sum E_i t_i}{\sum E_i}.$$

When multiple showers were observed in the BV, they were labeled as $\gamma_1, \gamma_2, \dots, \gamma_n$ according to the energy from the highest (γ_1) to the lowest (γ_n). In this notation, e.g. E_{γ_3} denotes the third highest energy of the photons in the final state.

3.1.3 Kinematic fit

A least-square fit was used in this analysis to reconstruct the $K^+ \rightarrow \pi^0 \mu^+ \nu_\mu \gamma$ events with one undetected particle (neutrino) in the final state. This is a technique called “kinematic fit” and has widely been used in the analysis of high-energy physics experiments [37, 38, 39].

In the mathematical formula of the kinematic fit, there are:

- measured and fitted variables y_i, η_i ($i = 1, \dots, N$),
- unmeasured variables ξ_j ($j = 1, \dots, J$),
- constraints $f_k(\eta_1, \eta_2, \dots, \eta_N, \xi_1, \xi_2, \dots, \xi_J) = 0$ ($k = 1, \dots, K$), and
- covariant matrix \mathbf{V} ,

and the following notations are adopted.

$$\begin{aligned}\mathbf{y} &\equiv (y_1, y_2, \dots, y_N)^T \\ \boldsymbol{\eta} &\equiv (\eta_1, \eta_2, \dots, \eta_N)^T \\ \mathbf{f} &\equiv (f_1(\eta, \xi), f_2(\eta, \xi), \dots, f_K(\eta, \xi))^T\end{aligned}$$

The χ^2 to evaluate the goodness of fit is defined as

$$\chi^2(\eta) = (\mathbf{y} - \boldsymbol{\eta})^T \mathbf{V}^{-1} (\mathbf{y} - \boldsymbol{\eta}).$$

The mathematical problem is how to minimize $\chi^2(\eta)$ under the constraints of $\mathbf{f}(\eta, \xi) = \mathbf{0}$. In order to use the method with Lagrangian multipliers, additional parameters λ_i ($i = 1, \dots, K$) are introduced. The notation $\boldsymbol{\lambda}$ is defined as $\boldsymbol{\lambda} = (\lambda_1, \dots, \lambda_K)^T$. The original problem is now equivalent to the minimization of $\chi^2(\eta, \xi, \lambda)$ defines as follows.

$$\chi^2(\eta, \xi, \lambda) = (\mathbf{y} - \boldsymbol{\eta})^T \mathbf{V}^{-1} (\mathbf{y} - \boldsymbol{\eta}) + 2\boldsymbol{\lambda}^T \mathbf{f}(\eta, \xi)$$

The partial derivative of χ^2 by each variable in η_i, ξ_j , and λ_k should be zero at the minimum of χ^2 .

$$\begin{aligned}\frac{\partial \chi^2(\eta, \xi, \lambda)}{\partial \eta_i} &= -2(\mathbf{V}^{-1}(\mathbf{y} - \boldsymbol{\eta}))_i + 2(\mathbf{F}_\eta^T \boldsymbol{\lambda})_i = 0, \\ \frac{\partial \chi^2(\eta, \xi, \lambda)}{\partial \xi_j} &= 2(\mathbf{F}_\xi^T \boldsymbol{\lambda})_j = 0, \text{ and} \\ \frac{\partial \chi^2(\eta, \xi, \lambda)}{\partial \lambda_k} &= 2f_k(\eta, \xi) = 0,\end{aligned}$$

with the matrices \mathbf{F}_η and \mathbf{F}_ξ defined as:

$$\begin{aligned}(\mathbf{F}_\eta)_{ki} &\equiv \frac{\partial f_k(\eta, \xi)}{\partial \eta_i}, \text{ and} \\ (\mathbf{F}_\xi)_{ki} &\equiv \frac{\partial f_k(\eta, \xi)}{\partial \xi_i}.\end{aligned}$$

By solving these equations, the fitted variables of η_i, ξ_j and the minimized χ^2 are obtained. In the algorithm of the fit in this analysis, several iterations were performed until the χ^2 was converged;

we gave up when the iteration repeated 20 times. Results of $(\nu + 1)$ -th iteration are expressed as:

$$\begin{aligned}\xi^{\nu+1} &= \xi^\nu - (\mathbf{F}_\xi^T \mathbf{S}^{-1} \mathbf{F}_\xi)^{-1} \mathbf{F}_\xi^T \mathbf{S}^{-1} \mathbf{r}, \\ \lambda^{\nu+1} &= \mathbf{S}^{-1} [\mathbf{r} + \mathbf{F}_\xi (\xi^{\nu+1} - \xi^\nu)], \text{ and} \\ \eta^{\nu+1} &= \mathbf{y} - \mathbf{V} \mathbf{F}_\eta^T \lambda^{\nu+1},\end{aligned}$$

with the matrices \mathbf{r} and \mathbf{S} defined as:

$$\begin{aligned}\mathbf{r} &\equiv \mathbf{f}^\nu + \mathbf{F}_\eta^\nu (\mathbf{y} - \eta^\nu), \text{ and} \\ \mathbf{S} &\equiv \mathbf{F}_\eta^\nu \mathbf{V} (\mathbf{F}_\eta^T)^\nu.\end{aligned}$$

In order to monitor the quality of the fitted variables, the variables called “stretch functions” are introduced. The stretch function sf_i to check the difference of the measured and fitted variables y_i and η_i is defined as:

$$sf_i = \frac{y_i - \eta_i}{\sqrt{\sigma_{y_i}^2 - \sigma_{\eta_i}^2}}$$

where σ_{y_i} and σ_{η_i} are the resolutions of y_i, η_i , respectively. If the kinematic fit is properly performed, all the stretch functions should be distributed as a Gaussian distribution with the mean = 0.0 and $\sigma = 1.0$ and the χ^2 probability distribution should be flat between 0 and 1. Since σ_{y_i} are not determined in advance, some iterations of tuning the σ_{y_i} are needed until all stretch functions and χ^2 probability get reasonable.

In this analysis, four types of kinematic fit were performed with the assumptions of $K_{\mu 3}$ decay, $K_{\pi 3}$ decay, $K_{\mu 3\gamma}$ decay, and $K_{\pi 2\gamma}$ decay. The kinematic fit with the assumption of $K_{\mu 3}$ or $K_{\pi 3}$ decay was applied and the results were used to select the events for calibrations and to check the performance of Monte Carlo simulation. In particular, the resolutions used for the muon and the photons in the kinematic fit on the $K_{\mu 3\gamma}$ assumption (and used in the elements of \mathbf{V} for $K_{\mu 3\gamma}$) were obtained from the studies of the $K_{\mu 3}$ events and the $K_{\pi 3}$ events, respectively, because we were not able to collect enough number of $K_{\mu 3\gamma}$ decay events in real data for doing the $K_{\mu 3\gamma}$ calibration directly. The parameters for the muon track were “borrowed” from those in the $K_{\mu 3}$ kinematic fit, and the parameters for the photons were borrowed from those in the $K_{\pi 3}$ kinematic fit. The validity of this method was examined by using Monte Carlo $K_{\mu 3\gamma}$ data as explained in Section 3.3. The $K_{\mu 3}$ kinematic fit was also used to eliminate the $K_{\mu 3}$ backgrounds. The kinematic fit on the $K_{\pi 2\gamma}$ assumption was used for the studies of the photon energy smearing as well as the acceptance factors of $K_{\mu 3\gamma}$ in Section 6.3.1.

In the kinematic fit on the $K_{\mu 3\gamma}$ assumption, there were 13 observables and three constraints. The observables were:

- Momentum vector of the charged particle (3 variables),
- Kinetic energy of the charged particle (1 variable), and
- Momentum vectors of three photons (3×3 variables).

The directions of the momentum vectors were defined to be from the kaon-decay vertex position. In the actual algorithm of the kinematic fit, the kinetic energy T_μ , momentum P_μ , azimuthal angle ϕ_μ and polar angle θ_μ of the muon and the energy E_γ , azimuthal angle ϕ_γ and polar angle θ_γ of each photon were used. The constraints were:

- The invariant mass of the total energy and momentum should be equal to the nominal mass of K^+ ,

- The kinetic energy and momentum of the charged particle should be consistent with a muon hypothesis, and
- The invariant mass of one pair of photons should be equal to the nominal mass of π^0 .

In the events with three photons in the final state, there are three possible pairings to form the π^0 (and assign the emitted photon). In the events with four photons in the final state, there are twelve possible pairing to form the π^0 and to assign the emitted photon. (The remaining one photon was regarded to be an accidental hit and was ignored in the fit.) Thus, three combinations in three-photon events and twelve combinations in four-photon events were tested, and the best kinematic-fitting result was used in subsequent analysis. Events with five or more photons were discarded in this analysis.

In the $K_{\mu 3}$ -assumed kinematic fitting, there were 10 observables with three constraints. The observables were: charged track momentum (3 variables), charged track kinetic energy (1 variable), and the momentum vector of two photons (2×3 variables). The constraints were: K^+ mass (1 constraint), μ^+ mass (1 constraint), and π^0 mass (1 constraint). In the events with three photons, there are three possible pairings to form the π^0 . In the events with four photons, there are six possible pairings to form the π^0 . Thus, three combinations in three photon events and six combinations in four photon events were tested, and the best kinematic-fitting result was used in the subsequent analysis.

In the $K_{\pi 3}$ -assumed kinematic fit, one photon out of four photons was deliberately ignored in order to imitate the $K_{\mu 3\gamma}$ kinematic fit, and 13 variables with three constraints were used. The measured variables were: charged track momentum (3 variables), charged track kinetic energy (1 variable), and momentum vectors of three photons (3×3 variables). The constraints were: K^+ mass (1 constraint), π^+ mass (1 constraint), and π^0 mass (1 constraint). It should be noted that one possible constraint: π^0 mass of the third photon and the missing (or ignored) photon, was not imposed. This kinematic fit was performed only for four photon events. The photon with the lowest energy was ignored and three possible combinations for the three photons were tested.

In the $K_{\pi 2\gamma}$ -assumed kinematic fit, there were thirteen variables and six constraints. The measure variables were: charged track momentum (3 variables), charged track kinetic energy (1 variable), and the momentum vectors of three photons (3×3 variables). The constraints were: K^+ mass (1 constraint), π^+ mass (1 constraint), π^0 mass (1 constraint), and the total momentum conservation (3 constraints). Only in this case, the charged track was reconstructed as π^+ ; the presence of the additional 4 MeV deposit in the RS stopping counter due to the $\pi^+ \rightarrow \mu^+ \nu$ decay at rest was assumed and was subtracted from the observed energy. This kinematic fitting was performed only for the three photon events. The three possible pairing to form the π^0 were tested and the best result was used.

3.2 Calibration

3.2.1 BV visible fraction

The visible fraction $VSFR_{BV}$ was calibrated by comparing the monochromatic peak of the sum of the energies of two photons from π^0 in the $K_{\pi 2}$ decay ($K^+ \rightarrow \pi^+ \pi^0$) with the expected value (245.56 MeV), and was obtained to be 0.2922 in real data. In this calibration the $K\pi 2(2)$ monitor trigger, explained in Section 2.2, was used. The $K_{\pi 2}$ events were selected by requiring that the momentum, kinetic energy and range of the π^+ track were consistent with those of the π^+ from $K_{\pi 2}$ (Fig. 3.3) and no photon was observed in the photon detectors except for the BV. The results are shown in Fig. 3.4.

The same procedures were applied to the Monte Carlo $K_{\pi 2}$ events; the visible fraction for the Monte Carlo events was obtained to be 0.2920.

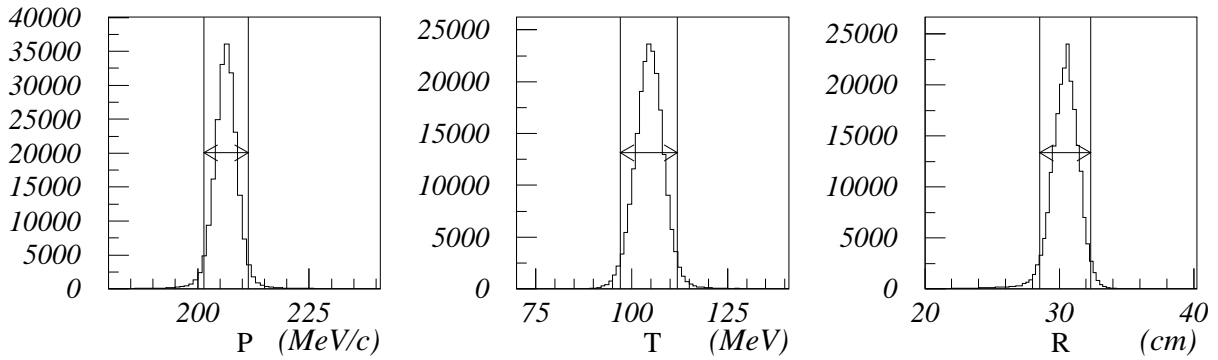


Figure 3.3: Momentum (left), kinetic energy (middle), and range (right) of the π^+ tracks in the events used for the BV energy calibration. The arrows indicate the region accepted as the π^+ track from $K_{\pi 2}$.

3.2.2 parameters for BV z-measurement

The z position of the electromagnetic shower in BV was measured from ADCs and TDCs in both ends. The following relations should be satisfied by using the notation defined in Section 3.1.2.

$$\frac{\lambda}{2} \log(A_1/A_2) - O_A = \kappa(T_1 - T_2)/2 - O_T$$

As shown in Fig. 3.5, a linear fit was made to the two-dimensional plot of Z_{ADC} vs Z_{TDC} . The attenuation length (λ) and the offset for the ADC-based z measurement (O_A) were obtained for each BV module, with the assumption that the speed-of-light (κ) and the offsets for the TDC-based z measurement (O_T) are common to all the counters. The speed-of-light was adopted from the analysis of the $K^+ \rightarrow \pi^+ \pi^0 \gamma$ decay [40] as

$$\kappa = 17.44 \text{ cm/nsec.}$$

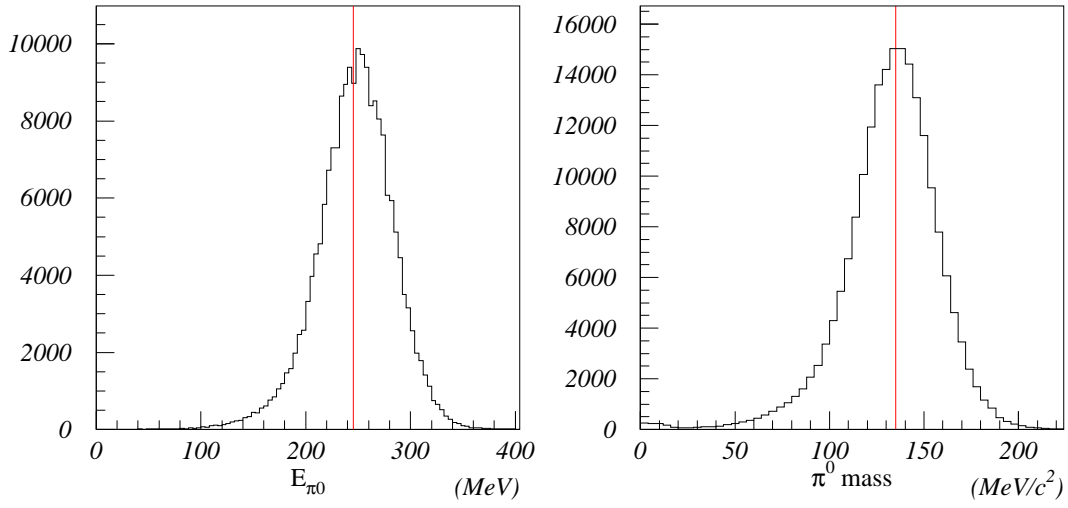


Figure 3.4: π^0 energy calculated from the sum of the energies of two photons (left) and the invariant mass of the two photons (right) from K_{π^2} . The red lines indicate the nominal values.

The mean value of the attenuation lengths of the BV modules in real data (86.67 cm) was used in the Monte Carlo simulation.

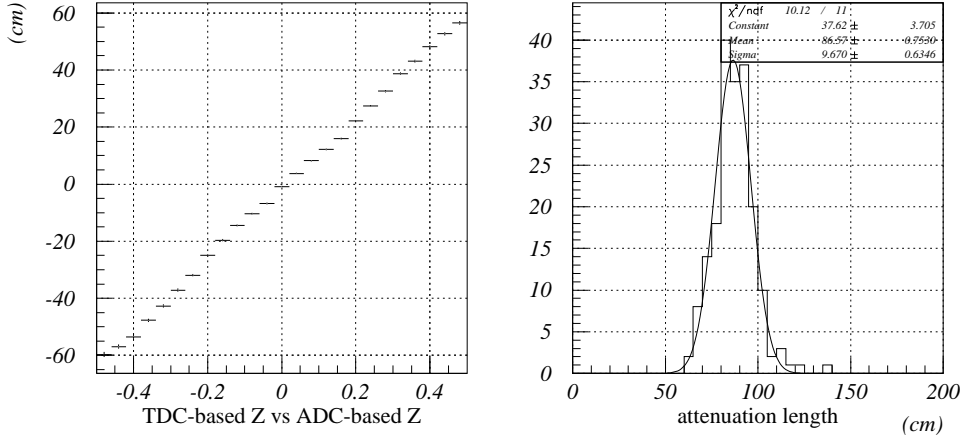


Figure 3.5: Linear fit of the ADC-based and TDC-based z measurements to a BV module (left); x-axis and y-axis are $\frac{1}{2} \log(\frac{A_1}{A_2})$ and $\kappa(T_1 - T_2)/2$, respectively. Distribution of the attenuation length from all the 192 BV modules (right).

3.2.3 parameters for kinematic fitting

In this section, the tuning of the parameters used in the kinematic fit (resolutions in the covariant matrix) with the $K_{\mu 3}$ and $K_{\pi 3}$ assumptions for real data are explained.

$K_{\mu 3}$ events were selected from the 3γ trigger sample with the following conditions.

- No photon was observed in the RS, I-counters, V-counters, and Endcap counters.
- There were only three photons in the BV.
- The timing of the photon with the lowest energy should not coincide with the charged track timing and should therefore be due to accidental hits.
- The event satisfied the kinematic fit on the $K_{\mu 3}$ assumption.

The charged track before and after these conditions were imposed are shown in Fig. 3.6. It is clearly seen that the charged tracks after the selection satisfied the range-momentum relation of muon, though no direct requirement for muon identification was imposed. The resolution for each observable was determined through monitoring the stretch function and the χ^2 probability distribution in the kinematic fit. The tuning results are shown in Fig. 3.7.

The $K_{\pi 3}$ events were selected from the 3γ trigger sample with the following conditions. (Reminded that charged tracks were reconstructed as μ^+ in the sample.)

- No photon was observed in the RS, I-counters, V-counters, and Endcap counters.
- There were four photons in the BV.
- The timings of all the four photons were close to the charged track time.
- The events satisfied the kinematic fit on the $K_{\pi 3}$ assumption.

quantity	unit	resolution
kinetic energy T_μ	MeV	$0.379 \times \sqrt{T_\mu}$
momentum P_μ	MeV/c	$\sqrt{(0.0227P_\mu)^2 - (0.00784P_\mu)^4}$
azimuthal angle ϕ_μ	mrاد	17.6
polar angle θ_μ	mrاد	$32.2 \times \cos \theta_\mu$

Table 3.1: Resolutions on the muon observables assumed in the kinematic fit on the $K_{\mu 3\gamma}$ assumption.

quantity	unit	resolution
energy E_γ	MeV	$1.61 \times \sqrt{E_\gamma}$
azimuthal angle ϕ_γ	mrاد	39.8
polar angle θ_γ	mrاد	$65.6 \times \cos \theta_\gamma$

Table 3.2: Resolutions on the photon observables assumed in the kinematic fit on the $K_{\mu 3\gamma}$ assumption.

- The momentum of charged track should be less than 130 MeV/c, which corresponds to the maximum π^+ momentum from $K_{\pi 3}$ (133 MeV/c).

The resolution for each observable was determined through monitoring the stretch functions and the χ^2 probability distribution. The tuning results are shown in Fig. 3.8.

The resolutions used for the muon and the photons in the fit on the $K_{\mu 3\gamma}$ assumption are summarized in Table 3.1 and Table 3.2, respectively.

Figure 3.9 (left) shows the invariant mass $\gamma\gamma$ mass ($M_{\gamma\gamma}$) distribution of the π^0 from the $K_{\mu 3}$ events, and Figure 3.9 (right) shows the $M_{\gamma\gamma}$ distribution of the π^0 from the $K_{\pi 3}$ events. In both cases, it is demonstrated that two photons from π^0 are properly selected by the kinematical fit.

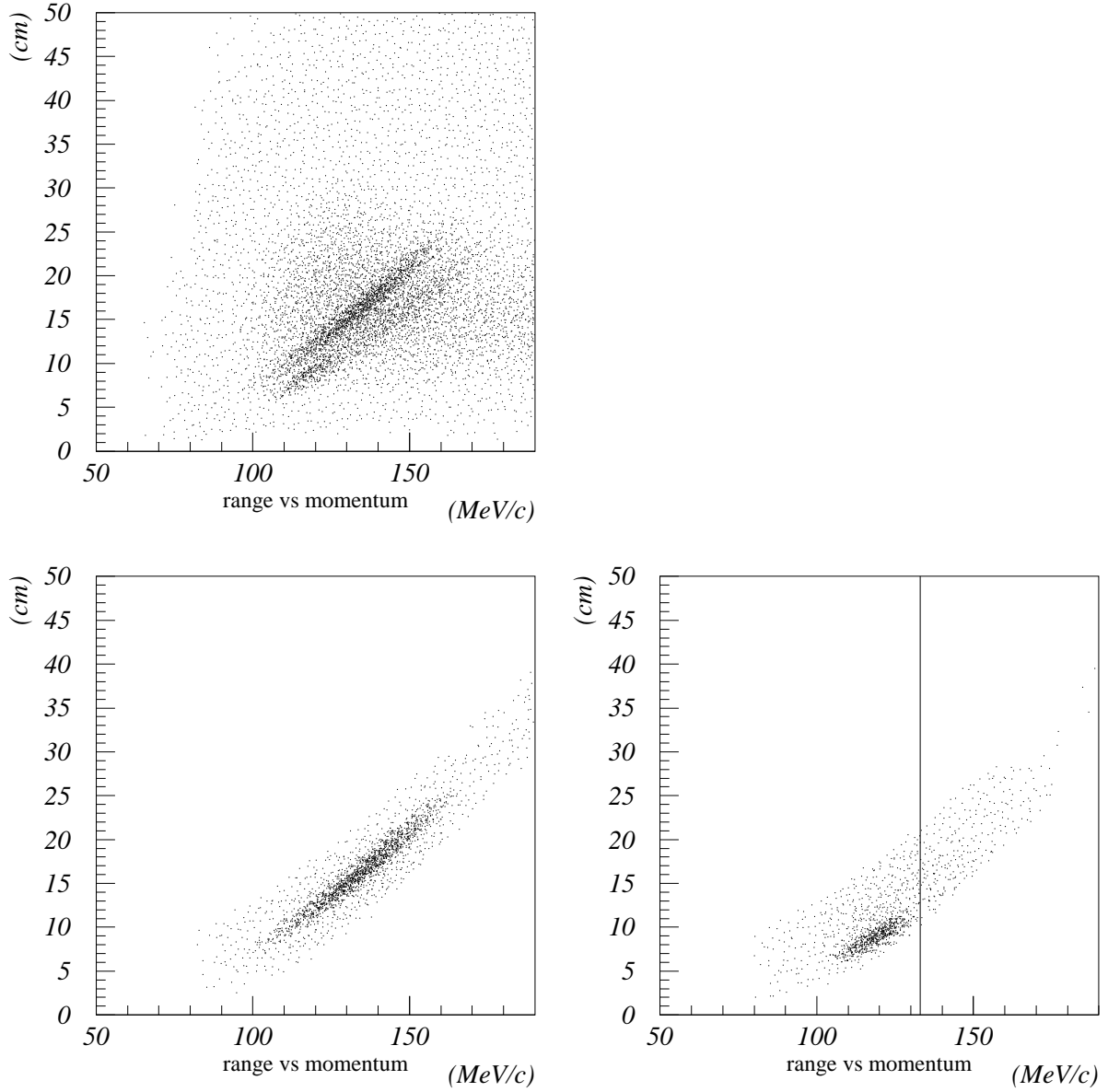


Figure 3.6: Range vs momentum plots of the charged tracks in the sample for tuning kinematic fitting before (top left) and after imposing the selection criteria for $K_{\mu 3}$ (bottom left) and $K_{\pi 3}$ (bottom right) in this section, respectively. In the plot for $K_{\pi 3}$, the condition $P < 133 \text{ MeV}/c$ is not imposed.

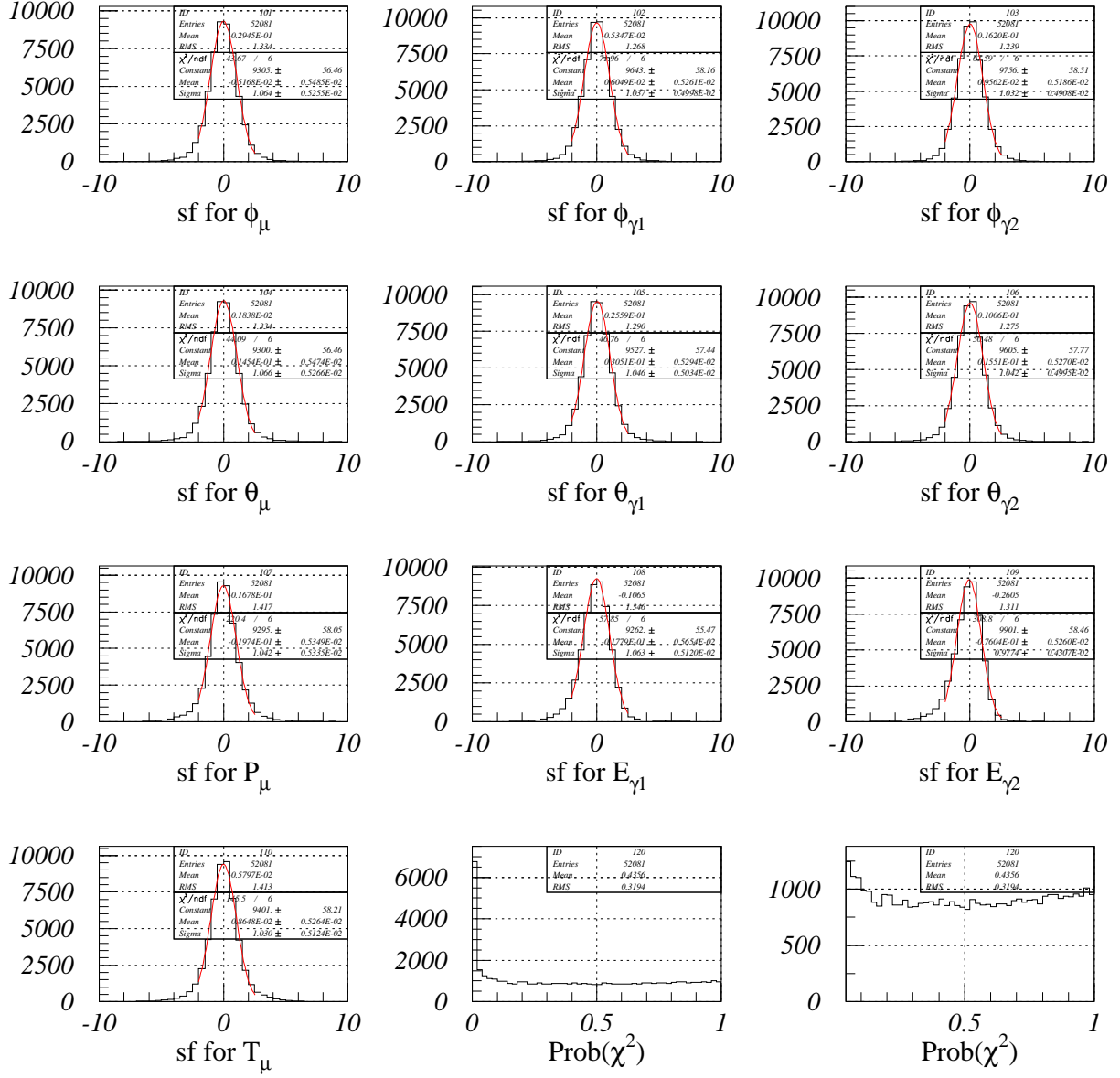


Figure 3.7: Distributions of stretch functions for the 10 parameters in the kinematic fit on the $K_{\mu 3}$ assumption (from top left to bottom left) and the χ^2 probability distributions from 0 to 1 (bottom middle) and from 0.05 to 1 (bottom right).

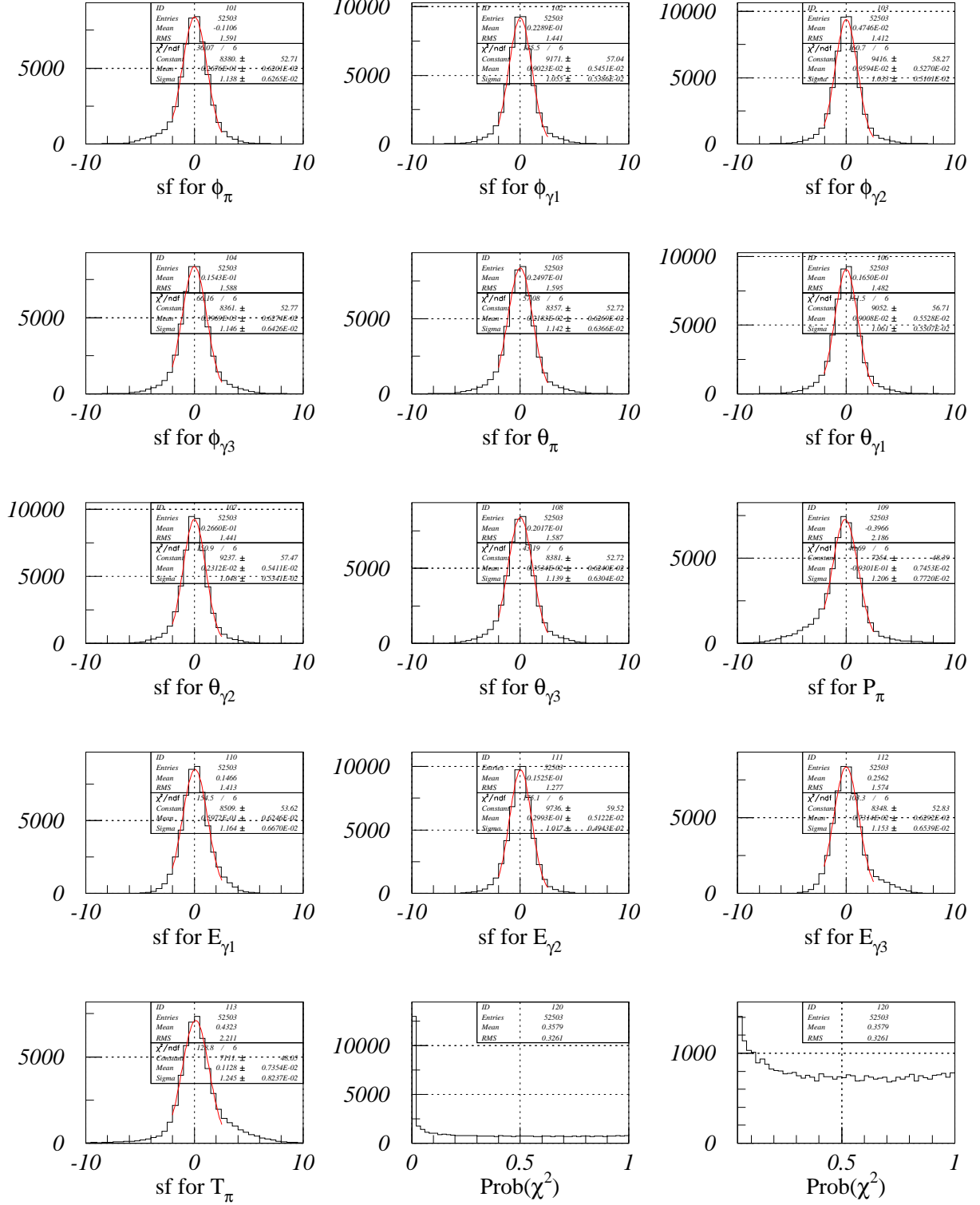


Figure 3.8: Distributions of stretch functions for the 13 parameters in the kinematic fitting with the $K_{\pi 3}$ assumption (from top left to bottom left) and the χ^2 probability distributions from 0 to 1 (bottom middle) and from 0.05 to 1 (bottom right).

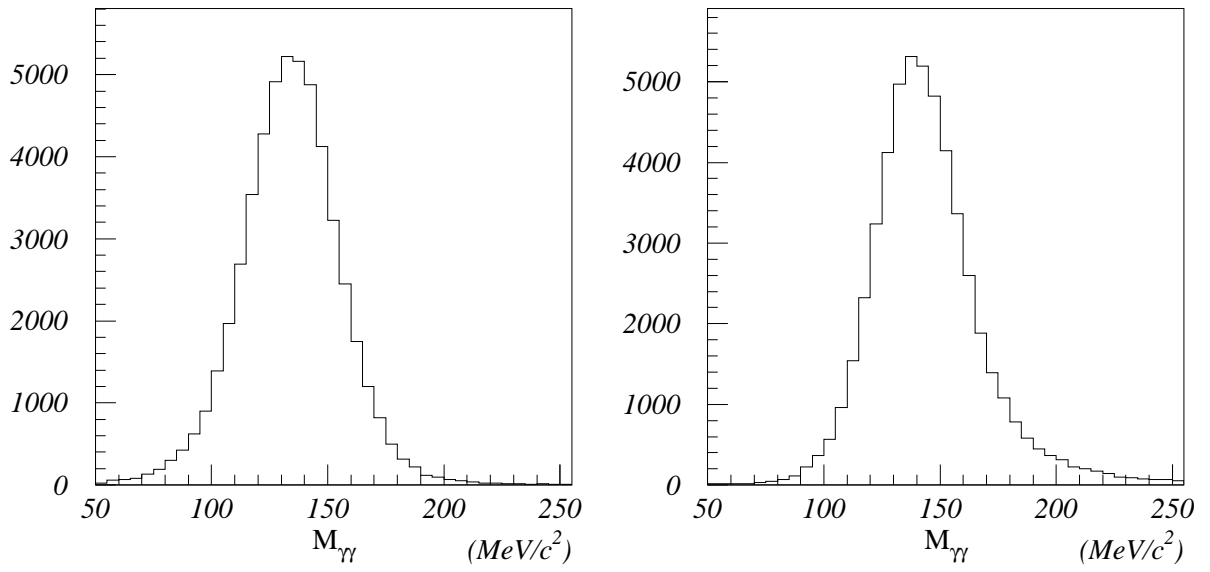


Figure 3.9: $M_{\gamma\gamma}$ distributions of the π^0 from the $K_{\mu 3}$ (left) and $K_{\pi 3}$ (right) events.

3.3 smearing of the observables in Monte Carlo

The performance of the detector subsystems in the Monte Carlo simulation is usually better than the performance in the real data. The observables in the Monte Carlo events do not necessarily reproduce all the distributions from the real data. Instead of tuning the specific kinematic fit resolutions for reconstructing Monte Carlo events, the observables in the Monte Carlo events were properly smeared with deviates drawn from a Gaussian distribution, as explained in this section, so that the Monte Carlo events were reconstructed with the same kinematic-fit algorithm and resolutions as used in the analysis of real data.

In the subsequent subsections, "g" denotes a random number from the normal Gaussian distribution (with the mean of 0.0 and the sigma of 1.0).

3.3.1 BV energy

For Monte Carlo data, the energy of each BV module was smeared as

$$E_i^{smeared} = E_i + P_{smearing} \times g \times \sqrt{E_i},$$

where $P_{smearing}$ is the smearing parameter and the energies are in MeV. In the case that $E_i^{smeared}$ got to be negative, the value was replaced to be 0.1MeV. In order to determine $P_{smearing}$, the Monte Carlo $K^+ \rightarrow \pi^+ \pi^0 \gamma$ events were reconstructed by the kinematic fit on the $K_{\pi 2 \gamma}$ assumption. The best value of $P_{smearing}$, 0.55, was obtained by changing $P_{smearing}$ and monitoring the χ^2 probability distributions, as shown in Fig. 3.10.

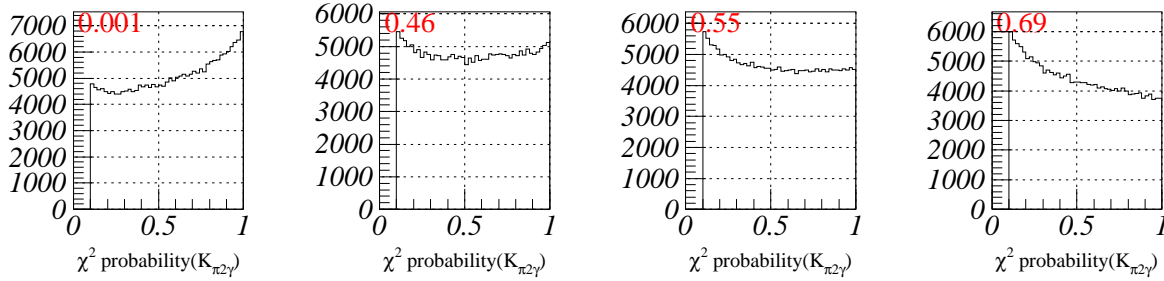


Figure 3.10: χ^2 probability distributions of the Monte Carlo $K_{\pi 2 \gamma}$ events by setting the smearing parameters $P_{smearing}$ to 0.001, 0.46, 0.55, and 0.69 (from left to right).

3.3.2 BV z-offset

The muons from $K_{\mu 2}$ decay can easily penetrate the RS counters and reach the BV modules. The expected hit position in BV (defined as Z_{RS}) can be calculated from the extrapolation of the charged track reconstructed in the RS. The accuracy of the BV Z reconstruction was evaluated with the measured z-position in BV minus the expected z-position from the extrapolated track. Z-offset

smearing was applied with the following formulae:

$$\begin{aligned}
Z_{smeared}^A &= Z^A - s_{za} \times g, \\
Z_{smeared}^T &= Z^T - s_{zt} \times g, \text{ and} \\
Z_{smeared} &= \frac{Z_{smeared}^T + \sqrt{E_{smeared}/10} Z_{smeared}^A}{1 + \sqrt{E_{smeared}/10}},
\end{aligned}$$

where s_{za} and s_{zt} are the smearing parameters for the ADC-based and TDC-based measurements, respectively. It should be mentioned that the observable Z was not smeared directly but affected by the smearing in E , Z^T and Z^A in the calculation. The z-offset smearing parameters were tuned so that the distributions were consistent for Z , Z_{TDC} and Z_{ADC} between the real and Monte Carlo data. The following three variables in data and Monte Carlo are checked as shown in Fig. 3.11.

$$\begin{aligned}
A_Z &= Z^{smeared} - Z_{RS} \\
A_{Z_{TDC}} &= Z_{TDC}^{smeared} - Z_{RS} \\
A_{Z_{ADC}} &= Z_{ADC}^{smeared} - Z_{RS}
\end{aligned}$$

The tuning parameters were $s_{za} = 6.59$ cm and $s_{zt} = 8.75$ cm.

3.3.3 smearing for charged track

The smearing parameters were obtained from the differences between the resolutions of real data and Monte Carlo. The resolution of kinetic energy and momentum of charged track ($\sigma_{real}(E_\mu)$ and $\sigma_{real}(P_\mu)$) were obtained in the procedure explained in the Section 3.2.3. The resolutions of kinetic energy and momentum of Monte Carlo data ($\sigma_{MC}(E_\mu)$, $\sigma_{MC}(P_\mu)$) were determined by doing kinematic fit tuning without all the smearing, and the following formula was used to estimate the smearing quantity.

$$X_{smearing} \equiv \sqrt{\sigma_{real}^2(X) - \sigma_{MC}^2(X)} \quad (X = T_\mu, P_\mu)$$

The validity of this smearing was confirmed in the kinematic fit in which all smearing was applied and all the resolutions were adopted. Distributions of the stretch functions of the observables and the χ^2 probability of the kinematic fit on the $K_{\mu 3}$ assumption, of the fit on the $K_{\pi 3}$ assumption, and of the fit on the $K_{\mu 3\gamma}$ assumption for Monte Carlo events are shown in Fig. 3.12, Fig. 3.13, and Fig. 3.14, respectively.

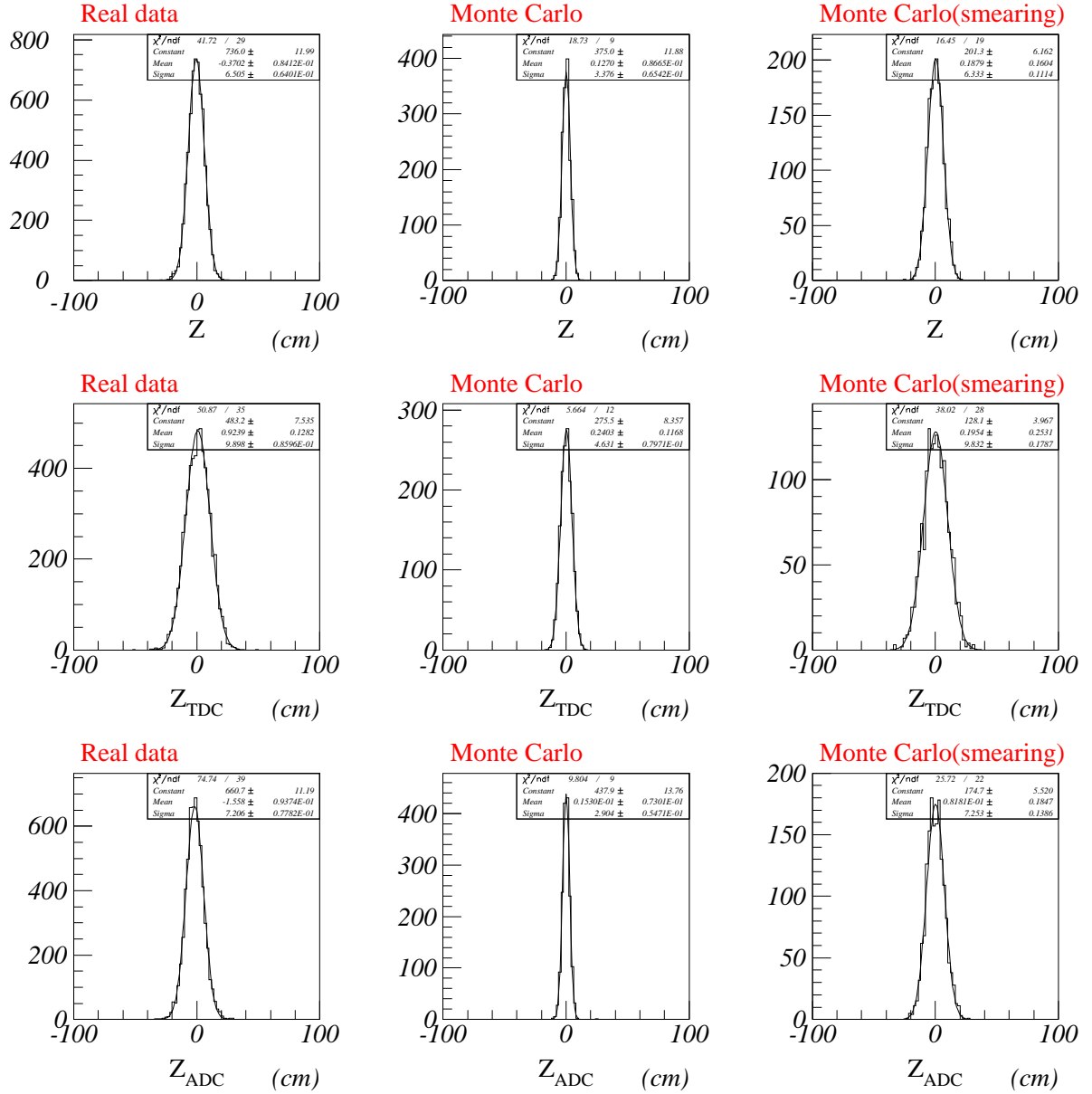


Figure 3.11: Z position of the photons in BV. Z accuracy for real data (top left), Z accuracy for MC data without smearing (top center), and Z accuracy for MC data after smearing (top right); Z_{TDC} accuracy for real data (middle left), Z_{TDC} accuracy for MC data without smearing (middle center), and Z_{TDC} accuracy for MC data after smearing (middle right); Z_{ADC} accuracy for real data (bottom left), Z_{ADC} accuracy for MC data without smearing (bottom center), and Z_{ADC} accuracy for MC data after smearing (bottom right).

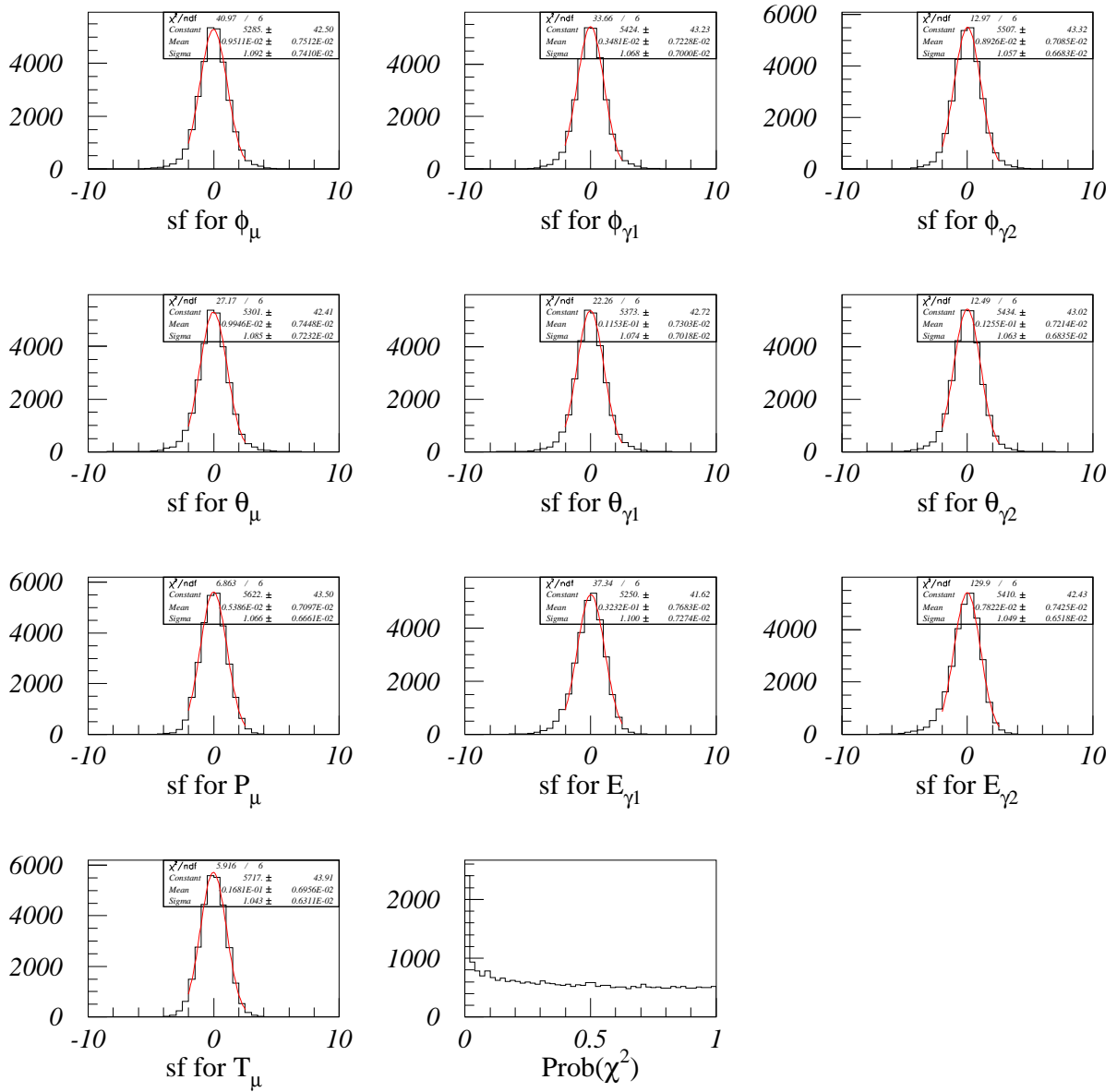


Figure 3.12: Distribution of stretch functions of the 10 observables (from to left to bottom left) and the χ^2 probability (bottom middle) of the $K_{\mu 3}$ -assumed kinematic fit for Monte Carlo $K_{\mu 3}$ data.

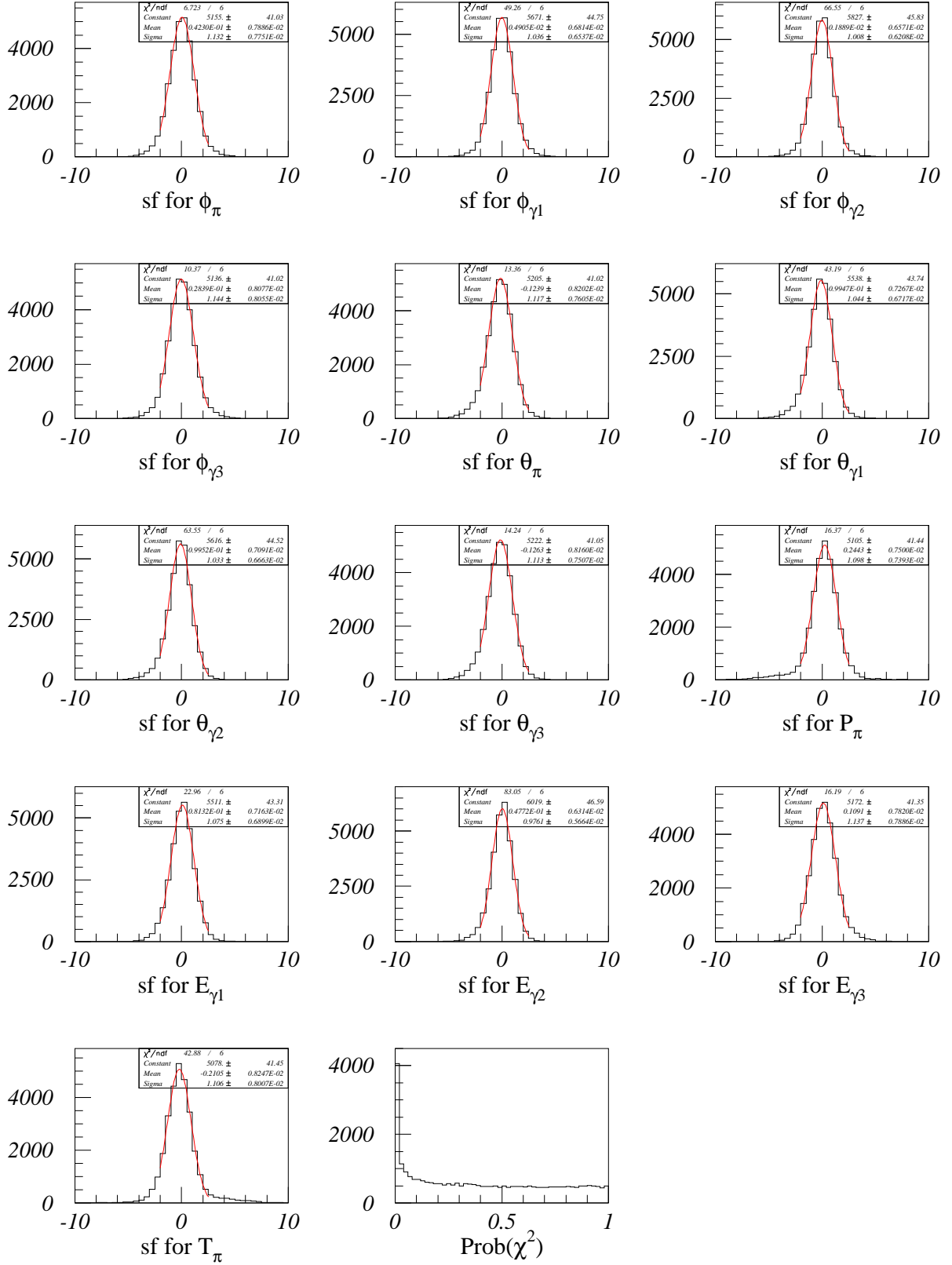


Figure 3.13: Distribution of stretch functions of the 13 observables (from top left to bottom left) and χ^2 probability (bottom middle) of the K_{π^3} -assumed kinematic fit for Monte Carlo K_{π^3} data.

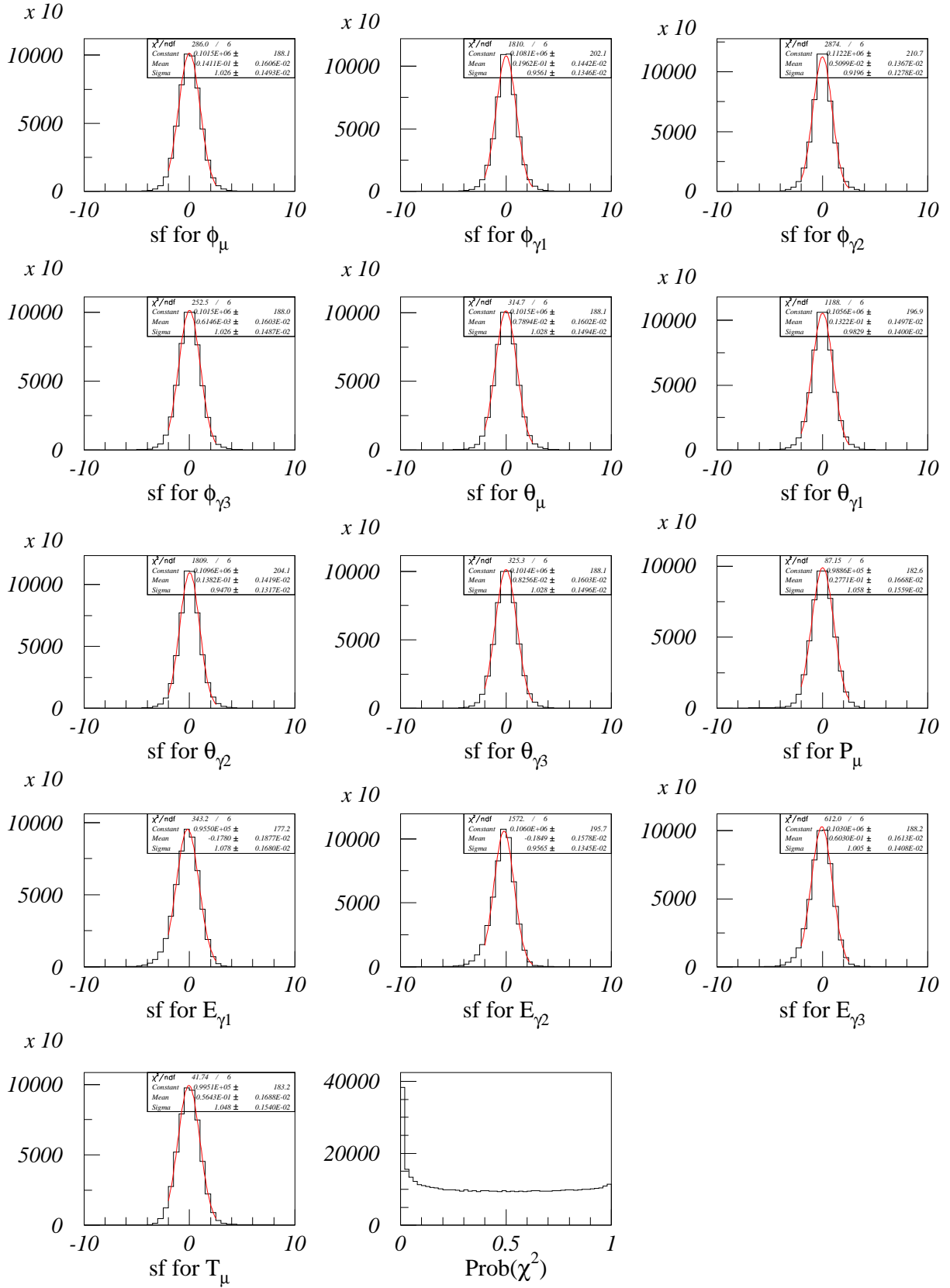


Figure 3.14: Distribution of stretch functions of the 13 observables (from top left to bottom left) and χ^2 probability (bottom middle) of the $K_{\mu 3\gamma}$ -assumed kinematic fit for Monte Carlo $K_{\mu 3\gamma}$ data.

Chapter 4

Event Selection

In order to verify that the $K^+ \rightarrow \pi^0 \mu^+ \nu_\mu \gamma$ events were properly reconstructed and to reduce the contamination of background events, offline selection criteria (“cuts”) were developed and were imposed to the reconstructed events. Each of the cuts used in this analysis is explained in this chapter. Studies on the background reduction and signal acceptance are described in the subsequent chapters.

4.1 Primary selection

The number of 3γ trigger events was 9.38×10^6 . After the charged track reconstruction, 6.92×10^6 events survived (PASS1). The following cuts on the charged track were imposed and 2.78×10^6 events survived (PASS2).

- itgqualt cut:
This cut required that the kaon decay position was located inside the fiducial volume of the target. The decay position was determined by the pattern recognition of the fiber hits in the target (in the XY-plane) and by the charged track which was reconstructed in the drift chamber and was extrapolated to the target (in Z).
- RS stopping layer cut:
The RS stopping layer, reconstructed offline, should be consistent with the trigger condition: in the 3rd to the 6th layer.
- cos3d cut:
This cut required that the cosine of the dip angle of the charged track with respect to the beam axis, $\cos 3d$, should be less than 0.5. This corresponds to the fiducial volume of the drift chamber and Range Stack in the E787 detector system.
- ptot cut:
Events were discarded if the momentum of the charged track P was larger than 190 MeV/c. Many of the triggered events were due to the $K_{\pi 2}$ decay for which π^+ had interactions within RS counters before coming to rest; these events were easily rejected because the π^+ momentum (205 MeV/c) was measured with the drift chamber.

Furthermore, the following cuts were imposed to remove the events triggered by kaon decays in flight before it came to rest (“single-beam” background events) or by multiple beam particles into the detector (“double-beam” background events, in particular when another K^+ came to the target simultaneously with the K^+ coming to rest), and 1.41×10^6 events survived.

- delayed coincidence cut:

To ensure that the charged track came from the K^+ decay at rest, the charged track timing (T_π) was required to be at least 2nsec later than the timing of the K^+ entering the target (T_K). That was called the offline “delayed coincidence” in the E787 analysis. Both T_π and T_K used in this cut were obtained from the hits in the target.

- beam cuts

The hits in the beam counters such as the Čerenkov counter, beam-wire chambers, and B4 counters were examined and a group of cuts called the “beam cuts” were imposed. The basic cuts in the E787 standard analysis were adopted. Details of the beam cuts are explained in Appendix C.

- target cuts

To ensure that the hit pattern of the fibers in the target are consistent with the K^+ decay at rest, a group of cuts called the “target cuts” were imposed. The basic cuts in the E787 standard analysis were adopted. The details of the target cuts are explained in Appendix D.

Then, after the photon reconstruction, event were discarded unless three or four photons were observed in the BV. A total of 1081117 events survived and were used in the subsequent analysis.

4.2 Selection of muon

4.2.1 range-momentum relation cuts

For eliminating e -track events (K_{e3} or $K_{e3\gamma}$), the measured range R was compared to the measured kinetic energy T . The range expected from the kinetic energy by assuming the muon mass, $r_\mu(T)$, was calculated and $|R - r_\mu(T)|$ was required to be less than 5.0 cm. This requirement is so rough that the difference of the distributions between real data and Monte Carlo was not considered.

For muon identification, a cut based on the measured range compared to that expected from the measured muon momentum was imposed. The new variable dr_ratio was adopted (Fig. 4.1) and was defined as $dr_ratio \equiv (R - r_\mu(P))/(r_\pi(P) - r_\mu(P))$, where $r_\mu(P)$ and $r_\pi(P)$ were the ranges expected from the given momentum P by assuming the nominal muon and pion masses, respectively. dr_ratio should be close to 0 (1) for muon (pion) tracks.

Since Monte Carlo simulation did not reproduce the dr_ratio distribution in real data well, equivalent cut positions were set for real data and Monte Carlo such that

$$\begin{aligned} -0.5 < dr_ratio < 0.35 & \quad (\text{for real data}), \\ -0.479 < dr_ratio < 0.206 & \quad (\text{for Monte Carlo}). \end{aligned}$$

The distributions of dr_ratio for $K^+ \rightarrow \pi^0 \mu^+ \nu_\mu \gamma$ and $K^+ \rightarrow \pi^+ \pi^0 \gamma$ decays in Monte Carlo are shown in Fig. 4.1.

The cuts in this section were imposed to the events before the kinematic fit; R , P , and T in the cuts are the measured values and not the one after the kinematic fit.

4.2.2 $\frac{dE}{dx}$ cut

For the charged track identification and to reject e^+ tracks in the RS, the energy deposit in each of the RS counters was checked. Assuming the type of charged particle (μ^+), the energy deposit in the i -th RS counter ($E_p(i)$) can be predicted from the thickness of the counter and the kinetic

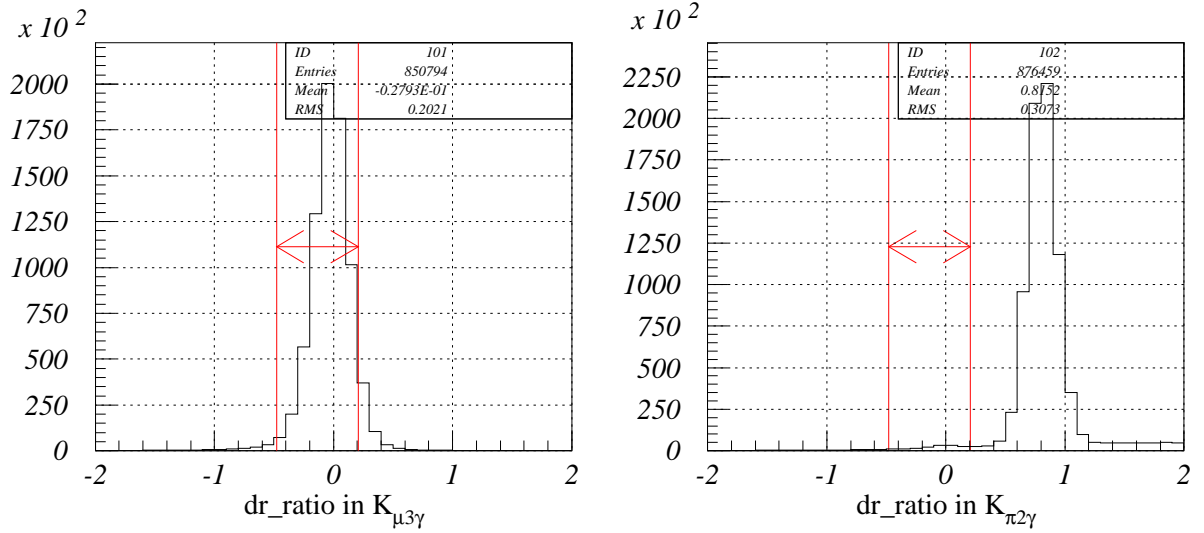


Figure 4.1: Distributions of the variable dr_ratio in $K^+ \rightarrow \pi^0 \mu^+ \nu_\mu \gamma$ (left) and in $K^+ \rightarrow \pi^+ \pi^0 \gamma$ (right) in Monte Carlo.

energy (and the velocity) of the charged track when it entered the counter, T_i . T_i can be calculated by subtracting the sum of the energy deposits, from the i -th to the stopping counter, from the total kinetic energy T . The deviation of the measured energy deposit ($E_m(i)$) from the predicted energy deposit ($E_p(i)$) was used as an indicator. The variable edf was defined as

$$edf \equiv \frac{\sum_i |E_m(i) - E_p(i)|}{\#layers},$$

where $\#layers$ was the number of layers which the charged particle passed through. The events with $edf > 2.0$ MeV were discarded (Fig. 4.2).

4.3 Selection of photons

4.3.1 number-of-photon cut (NG3)

For the $K_{\mu 3\gamma}$ decay, events were discarded unless exactly three photons with > 5 MeV were observed in the BV. This offline cut was not only for identifying the three photons in the final state of $K_{\mu 3\gamma}$ but also for detecting the activity due to an extra photon in the BV (“BV photon-veto cuts”).

4.3.2 Photon timing cut

The times of three photons in the final states should coincide with the charged track time. The timing window for real data was set to be ± 2 nsec. The time window used for Monte Carlo data was determined by the comparison of $K_{\pi 2}$ photon timing distributions because there was no smearing on the timing information on Monte Carlo, and was set to be -0.34 ± 1.02 nsec. The timing distributions of real data and Monte Carlo are shown in Fig. 4.3.

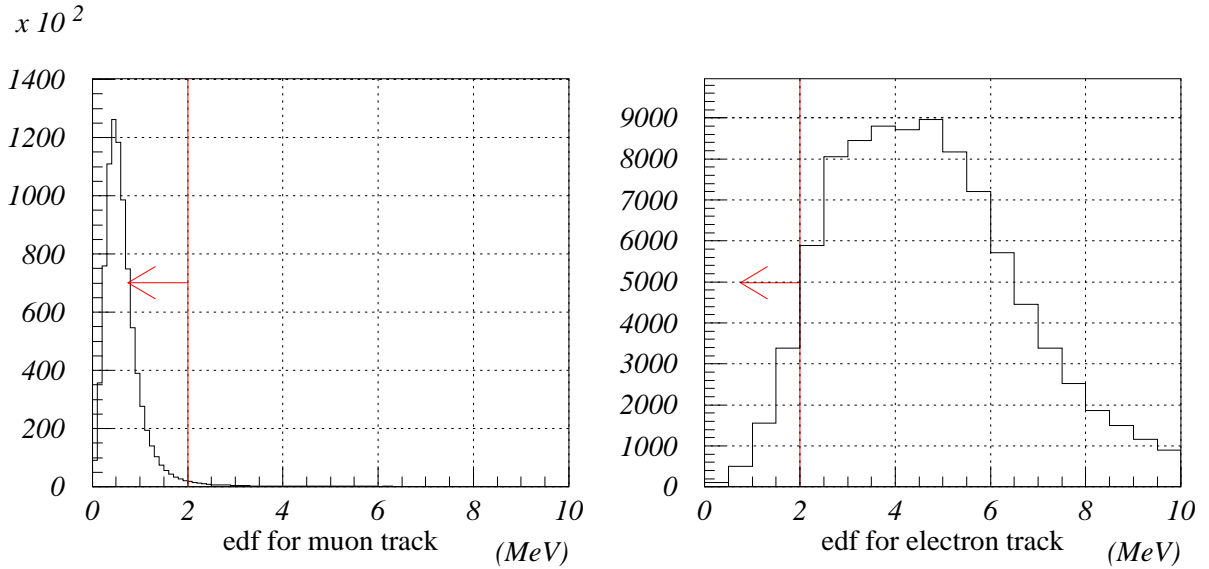


Figure 4.2: Distributions of the variable edf for the muon (left) and electron (right) tracks generated by the Monte Carlo simulation.

detector element	offset(nsec)	window(nsec)	threshold(MeV)
Endcap	0.50	± 2.50	2.40
Range Stack	1.50	± 3.50	0.40
target	-0.75	± 2.00	2.60
I-counter	-0.50	± 2.50	0.20
collar	2.50	± 5.00	0.60

Table 4.1: Photon veto requirements.

4.3.3 photon veto cuts

In order to identify the activity due to an extra photon in the K^+ decay, tight conditions on the offline photon detection (“photon veto”) were imposed on the timing and energy of the extra hits in the Endcap, Range Stack, target, I-counters, collar and micro collar counters. The timing offset, time window, and visible-energy threshold to each detector subsystem are summarized in Table. 4.1. The photon veto cuts also ensured that only those events in which the total photon energy from $K_{\mu 3\gamma}$ was deposited in the BV (and a part of the showers was not recorded in any other subsystem) were accepted.

4.3.4 *egcut* cut

The photon energy should also be sufficiently larger than the online energy threshold; since the threshold of the online NG3 requirement had been applied to the analog-sum signals separately for the upstream and downstream ends (subsection 2.1.5), the threshold level depended on the Z position of the shower in the BV. In order to confirm the effects of the attenuation of the visible

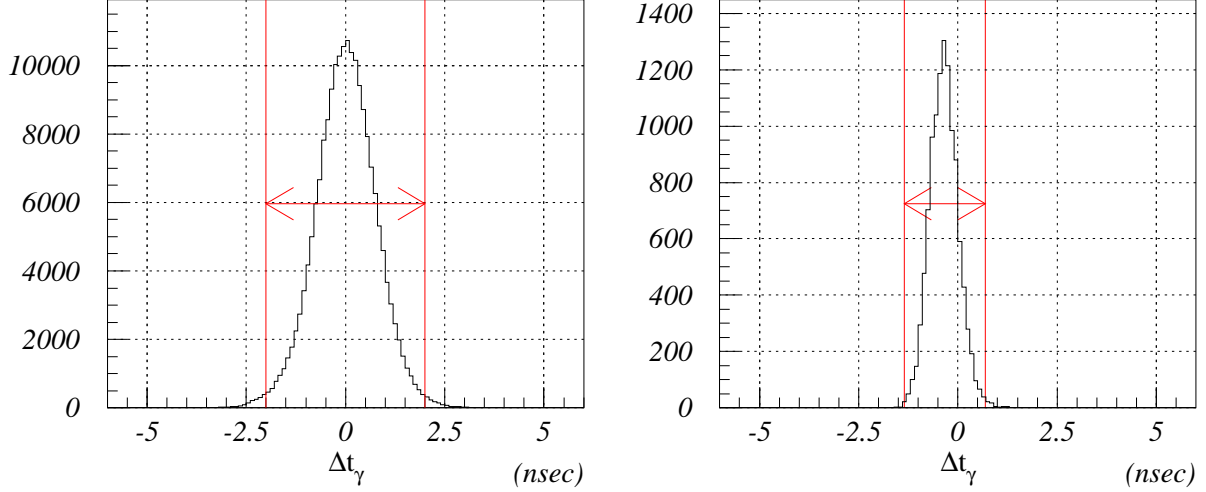


Figure 4.3: Photon timing relative to the charged track time Δt_γ in real data (left) and in Monte Carlo (right).

energy in the BV, the “Z-position corrected” photon energy, egc_i was calculated as:

$$egc_i \equiv E_{\gamma_i} \times \exp\left(-\frac{L/2 - |z_{\gamma_i}|}{\lambda_{mean}}\right),$$

where $\lambda_{mean} = 86.57$ cm was the mean value of the attenuation length in the BV modules, $L = 190.0$ cm was the total length of the BV modules, and Z_{γ_i} was the reconstructed Z-position of γ_i .

Events were discarded unless $egcut \equiv \min(egc_1, egc_2, egc_3)$ was larger than 22.0 MeV. This condition requires that the photon energy should be greater than 22 (66) MeV for the showers located at the edge (center) of the BV. This cut was imposed to both real data and Monte Carlo. Figure. 4.4 shows the E_{γ_i} versus Z_{γ_i} plots and $egcut$ distributions in real data and Monte Carlo.

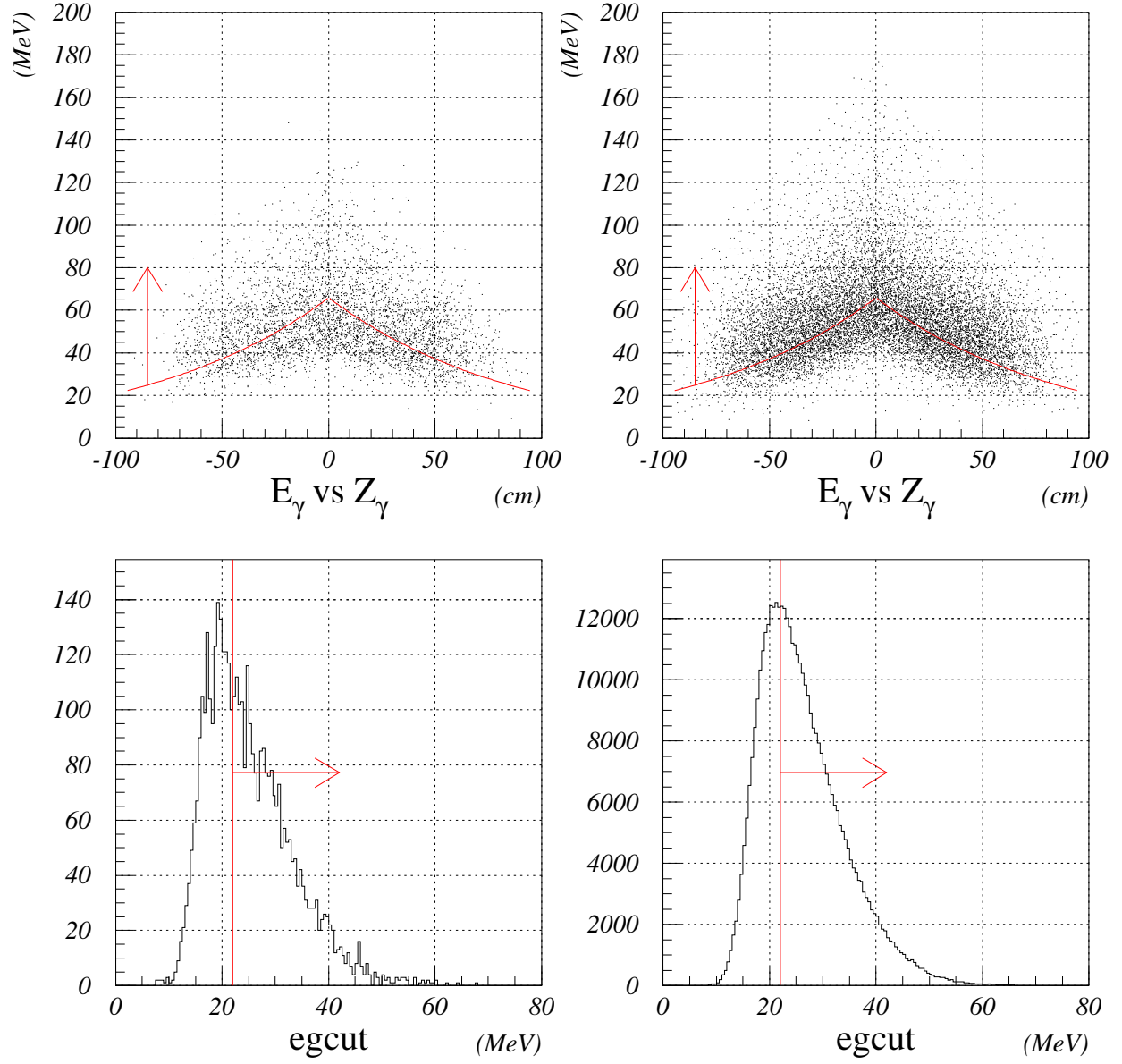
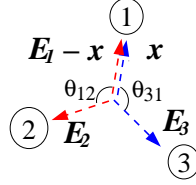


Figure 4.4: Photon energy versus Z position of the showers in the BV in real data (top left) and Monte Carlo $K^+ \rightarrow \pi^+ \pi^0 \gamma$ events (top right), where the curves in the plots indicate the cut realized by $egcut > 22\text{MeV}$; distributions of the variable $egcut$ in real data (bottom left) and Monte Carlo (bottom right).

4.3.5 fused cluster cut

This cut was designed for the purpose of removing the background events due to “fused cluster” in the K_{π^3} decay, in which two out of four photons from two π^0 were emitted to the same direction and the two electromagnetic showers in the BV overlapped each other and were reconstructed as a single cluster. The fused cluster could occur through two mechanisms: “odd” combination and “even” combination of the photons. The even combination means the overlap of two photons are originated from the same π^0 , while the odd combination means the overlap of two photons originated from different π^0 s. It was confirmed by Monte Carlo studies that the case with even combination was negligible; thus the case with odd combination should be considered. Two invariant masses m_{12} and m_{13} can be calculated by assuming that, in the fused cluster γ_1 with the energy of E_1 , there are two photons with energies of x_1 and $E_1 - x_1$ with the same azimuthal and polar angles, where x_1 is a parameter that varies from 0 to E_1 .



As illustrated in the figure above,

$$\begin{aligned} m_{12}(x_1) &= \sqrt{2E_2(E_1 - x_1)(1 - \cos \theta_{12})} \\ m_{13}(x_1) &= \sqrt{2E_3x_1(1 - \cos \theta_{31})} \end{aligned}$$

and a new function $F_1(x_1)$:

$$F_1(x_1) = \sqrt{(m_{12}(x_1) - m_{\pi^0})^2 + (m_{13}(x_1) - m_{\pi^0})^2}$$

are calculated with the nominal mass of π^0 : m_{π^0} . If there exists a value of x_1 which gives $F_1(x_1) \simeq 0$, it suggests γ_1 is a fused cluster. $F_1(x_1)$ is positive by definition; the minimum value $F_1(x_1)$ is worth monitoring. Although the minimum value can be obtained analytically, the rigorous expression is extremely complicated. Thus an approximate value (defined as $\min F_1$) is practically determined by the minimum value by changing x_1 from 0 to E_1 in 1 MeV step, i.e.

$$\min F_1 \equiv \min(F_1(1\text{MeV}), F_1(2\text{MeV}), \dots, F_1(\text{int}(E_1))),$$

where $\text{int}()$ means the function which returns the integer part of the argument. Applying the same procedures to other two photons, the minimum value of $F_1(x_1)$, $F_2(x_2)$, and $F_3(x_3)$ with all possible values of x_1 , x_2 , and x_3 , respectively, named $DPSQ (= \min(\min F_1, \min F_2, \min F_3))$, was obtained. $DPSQ$ would be small if an event was from K_{π^3} and one of γ_1, γ_2 , and γ_3 was the fused cluster.

On the other hand, the invariant masses of two out of the three reconstructed photons: $m_{\gamma_1\gamma_2}$, $m_{\gamma_2\gamma_3}$, and $m_{\gamma_3\gamma_1}$ were calculated, and the minimum of $|m_{\gamma_1\gamma_2} - m_{\pi^0}|$, $|m_{\gamma_2\gamma_3} - m_{\pi^0}|$, and $|m_{\gamma_3\gamma_1} - m_{\pi^0}|$, named $CHKSPZ$, was obtained. If an event was from K_{π^3} with odd combination, the invariant mass of any two photons should not be close to m_{π^0} and thereby $CHKSPZ$ would be large. Figure 4.5 shows the $DPSQ$ vs $CHKSPZ$ plots for the $K_{\mu^3\gamma}$ events and the K_{π^3} background events (after imposing the BV photon cuts and the photon veto cuts) generated by the Monte Carlo simulation. $DPSQ$ was required to be more than 30 MeV/ c^2 and $CHKSPZ$ was required to be less than 21 MeV/ c^2 .

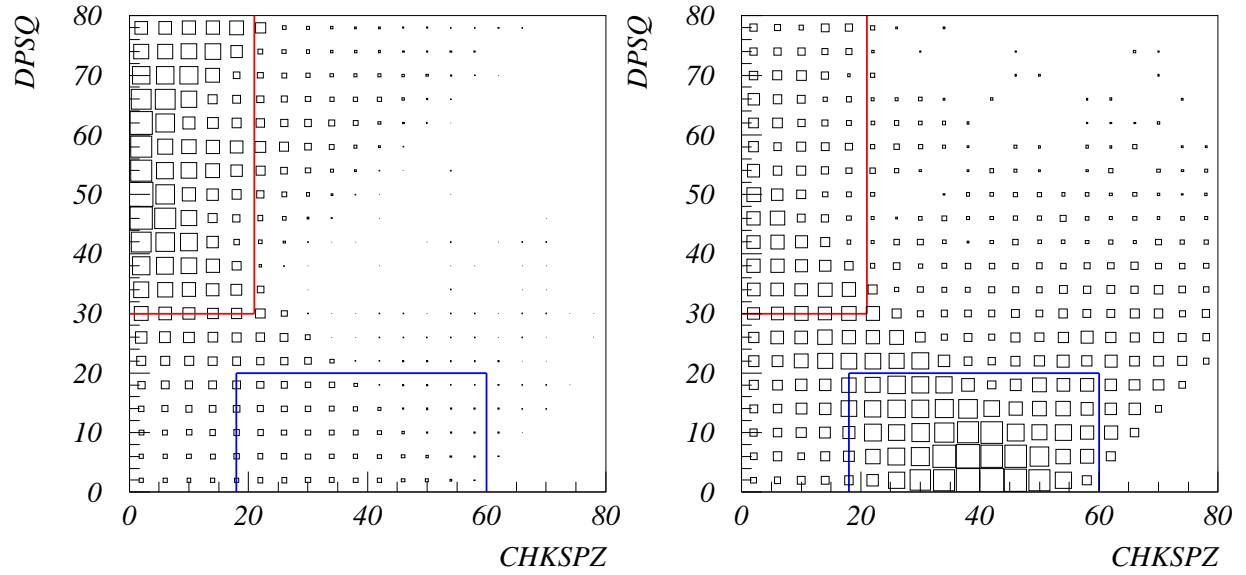


Figure 4.5: Plots of the variables $DPSQ$ vs $CHKSPZ$ for the $K_{\mu 3 \gamma}$ events (left) and $K_{\pi 3}$ background events (right) generated by the Monte Carlo simulation. The events in the red rectangle area ($DPSQ > 30$ and $CHKSPZ < 20$) were selected. The blue rectangle area ($18 < CHKSPZ < 60$ and $DPSQ < 21$) will be used in the $K_{\pi 3}$ background studies to tag the $K_{\pi 3}$ fused-cluster backgrounds.

4.3.6 e^+ bremsstrahlung cut

In order to remove the events with the photon due to bremsstrahlung of the e^+ track from the $K^+ \rightarrow \pi^0 e^+ \nu_e$ (K_{e3}) or $K^+ \rightarrow \pi^0 e^+ \nu_e \gamma$ ($K_{e3\gamma}$) decay within the RS, the angle between the direction of the hit position of the charged track at the RS T-counter from the center of the detector system and the direction of each of the photons from the kaon decay vertex position was checked. Events were discarded if the cosine of the angle, named amings, was larger than 0.9 (i.e. the angle was less than 26°), because the photon could be due to the bremsstrahlung. The distributions of amings for $K^+ \rightarrow \pi^0 \mu^+ \nu_\mu \gamma$ and $K^+ \rightarrow \pi^0 e^+ \nu_e$ decays in Monte Carlo are shown in Fig. 4.6.

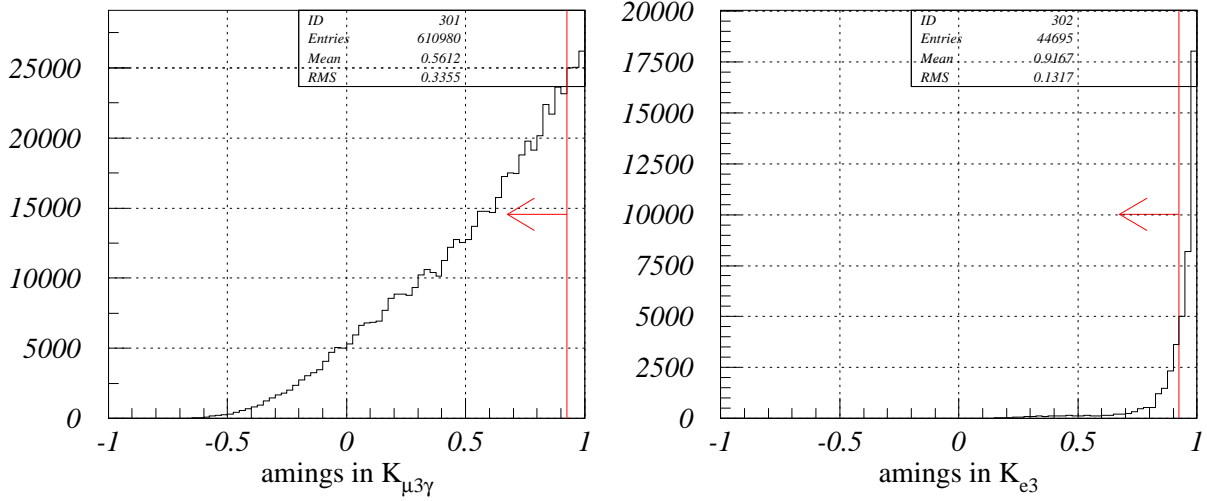


Figure 4.6: Distributions of the variable amings in $K^+ \rightarrow \pi^0 \mu^+ \nu_\mu \gamma$ events (left), and in $K^+ \rightarrow \pi^0 e^+ \nu_e$ events (right) generated by Monte Carlo simulation.

4.4 Kinematic fit

4.4.1 $K_{\mu 3\gamma}$ likelihood cut

The χ^2 probability of the kinematic fit on the $K_{\mu 3\gamma}$ assumption, $Prob(\chi^2_{K_{\mu 3\gamma}})$, was required to be more than 10%, as shown in Fig. 4.7.

4.4.2 $K_{\mu 3}$ likelihood cut

In order to suppress the $K_{\mu 3}$ backgrounds, the events whose χ^2 probability of the kinematic fit on the $K_{\mu 3}$ assumption, $Prob(\chi^2_{K_{\mu 3}})$, was more than 10% were discarded, as shown in Fig. 4.8.

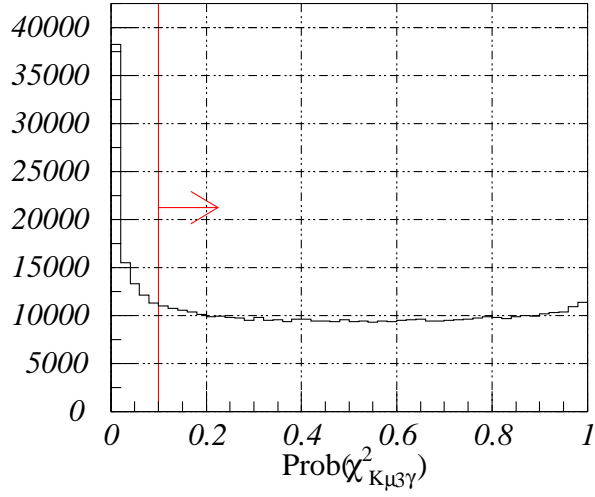


Figure 4.7: Distribution of $\text{Prob}(\chi^2_{K_{\mu 3} \gamma})$ from the events generated by Monte Carlo simulation

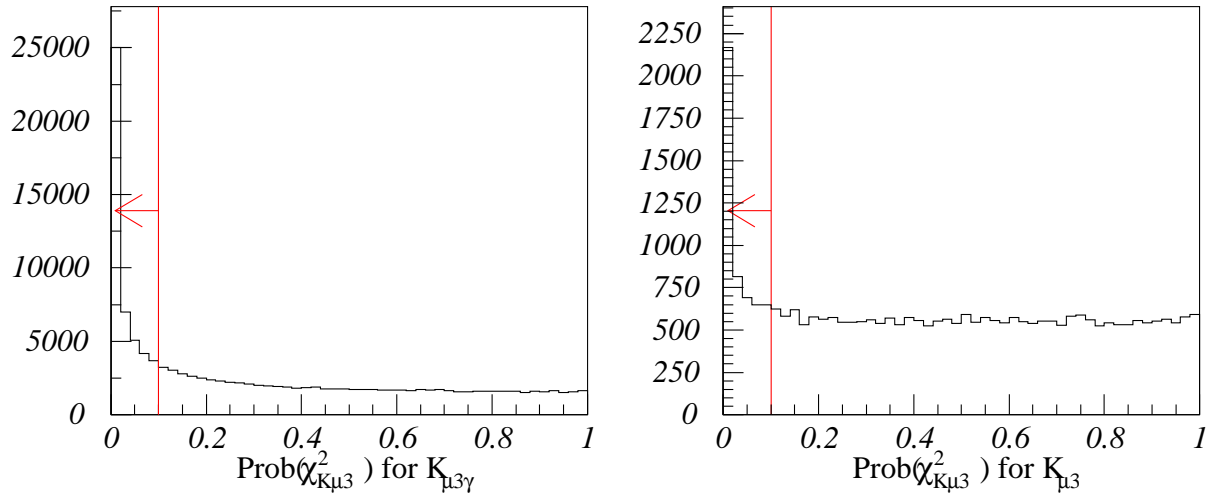


Figure 4.8: Distributions of $\text{Prob}(\chi^2_{K_{\mu 3}})$ for the $K_{\mu 3} \gamma$ events (left) and $K_{\mu 3}$ events (right) generated by Monte Carlo simulation.

4.5 Cuts after the kinematic fit

4.5.1 missing energy cut

The energy of the undetected particle (neutrino) in the final state, E_ν , should be larger than 60 MeV, as shown in Fig. 4.9. This cut suppressed the $K_{\pi 2\gamma}$ background events, in which E_ν should be small. It is worth mentioning that the peak position of E_ν for the $K_{\pi 2\gamma}$ is shifted to be +30 MeV because the kinetic energy of the charged track was calculated with the muon assumption and the invariant mass of the charged track was deliberately fitted to the muon mass.

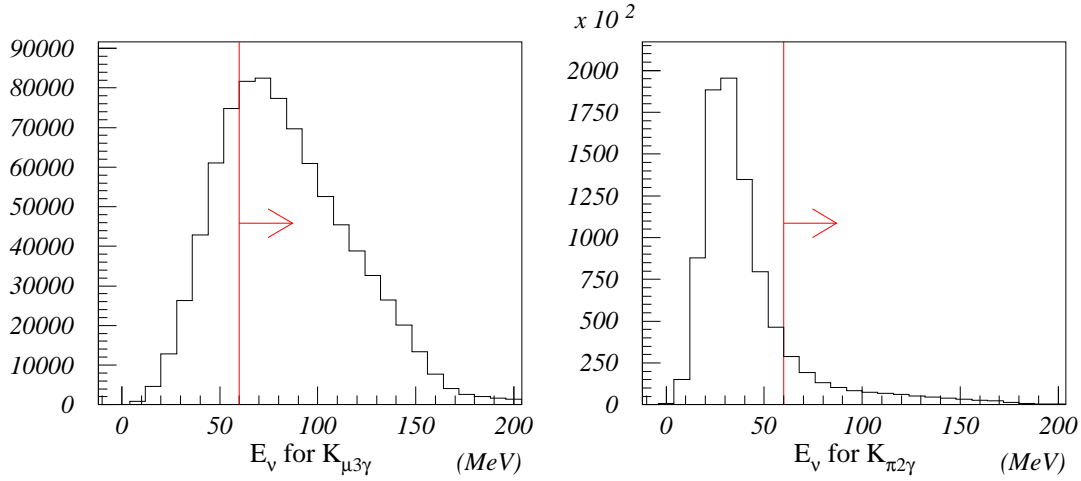


Figure 4.9: Distributions of E_ν from the $K_{\mu 3\gamma}$ events (left) and the $K_{\pi 2\gamma}$ events (right) generated by Monte Carlo simulation.

4.5.2 $M_{\mu\nu}$ cut

If decay-in-flight occurred to the π^+ from the $K_{\pi 2\gamma}$ decay, the event topology is the same as the $K_{\mu 3\gamma}$ decay. When the μ and ν came from a π^+ decay-in-flight, the invariant mass of the muon and neutrino, $M_{\mu\nu}$, should be close to the π^+ mass. In order to suppress the background events with the π^+ decay in flight, $M_{\mu\nu}$ was required to be larger than 200 MeV/ c^2 , as shown in Fig. 4.10.

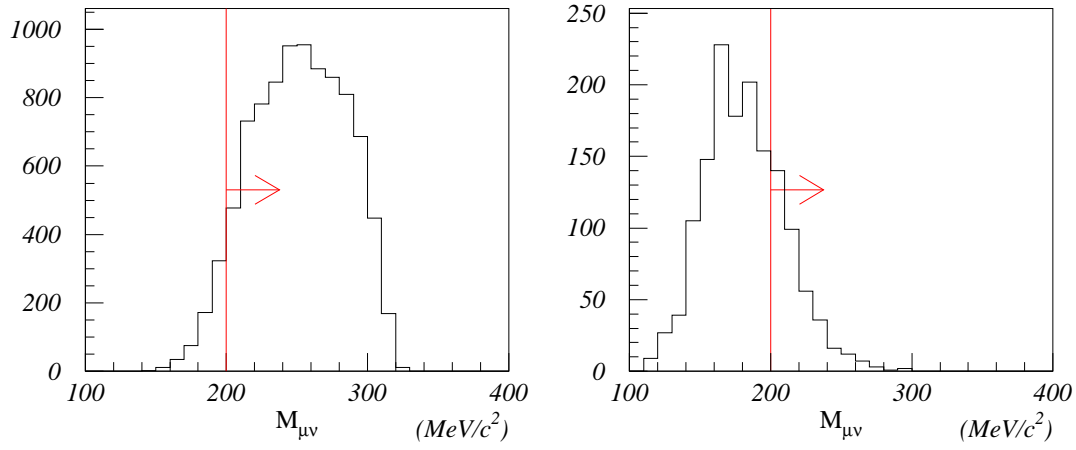


Figure 4.10: Distributions of the $M_{\mu\nu}$ from the $K_{\mu 3\gamma}$ events (left) and the $K_{\pi 2\gamma}$ events (right) generated by Monte Carlo simulation

4.5.3 θ_ν cut

The polar angle of the neutrino momentum vector with respect to the beam axis, θ_ν , should be larger than 26° ($|\cos \theta_\nu| \leq 0.9$) to prevent a photon in the final state from escaping along the beam direction and being undetected.

4.6 Data reduction

After imposing the cuts described in the above sections, 178 events survived. The reduction of the events after imposing each the cuts is summarized in Table 4.2.

cut	# of events	reduction
(input)	1081117	
range-momentum relation cut	346418	3.12
dE/dx cut	338431	1.02
number of photon cut	99680	3.40
photon timing cut	61718	1.62
photon veto cuts	45549	1.35
$egcut$ cut	10874	4.19
fused cluster cut	6319	1.72
e^+ bremsstrahlung cut	4553	1.39
$K_{\mu 3\gamma}$ likelihood cut	2630	1.73
$K_{\mu 3}$ likelihood cut	360	7.31
missing energy cut	297	1.21
$M_{\mu\nu}$ cut	190	1.56
θ_ν cut	178	1.07

Table 4.2: Data reduction after imposing each of the cuts in this chapter

4.7 Signal region

4.7.1 E_γ cut

The energy of the emitted photon, E_γ , should be larger than 30 MeV. The distribution of E_γ to the Monte Carlo $K_{\mu 3\gamma}$ events is shown in Fig. 4.11.

4.7.2 $\theta_{\mu\gamma}$ cut

The angle between the μ^+ track and the radiative photon should be $> 20^\circ$. The other requirement was $\theta_{\mu\gamma} < 60^\circ$ to improve the proportion of the correct pairing to π^0 (86% in the final sample) and to suppress the $K_{\pi 3}$ background. In other words, $\theta_{\mu\gamma}$ should satisfy $0.5 < \cos \theta_{\mu\gamma} < 0.94$. The distribution of cosine of $\theta_{\mu\gamma}$ to the Monte Carlo $K_{\mu 3\gamma}$ events is shown in Fig. 4.12.

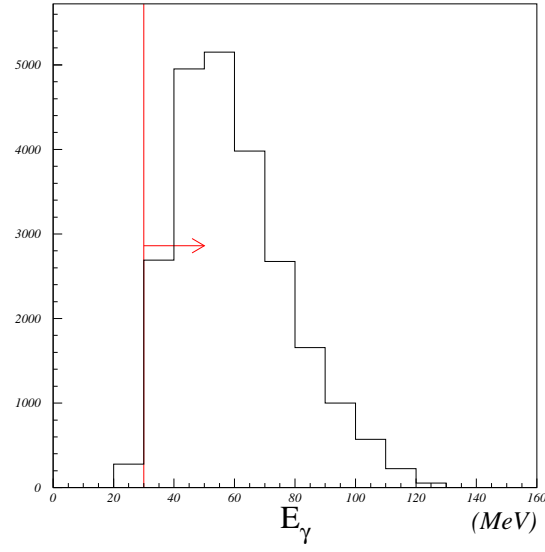


Figure 4.11: Distribution of E_γ in the $K_{\mu 3\gamma}$ events generated by Monte Carlo simulation.

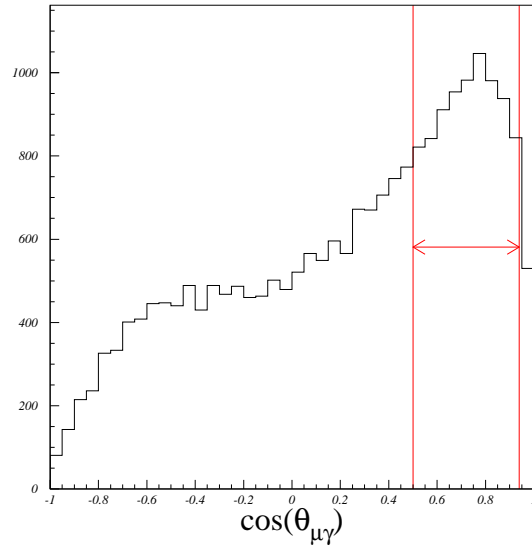


Figure 4.12: Distributions of the cosine of $\theta_{\mu\gamma}$ in the $K_{\mu 3\gamma}$ events generated by Monte Carlo simulation.

Chapter 5

Background expectation

5.1 Background sources

The momentum of the charged particles from K^+ decays at rest is shown in Fig.5.1. The signature of $K_{\mu 3\gamma}$ is a muon and three photons, including two photons from π^0 , in the final state. Kaon decays with a single charged track in the similar momentum region as $K_{\mu 3\gamma}$ and at least one π^0 in the final state are potential background sources. The background events are contained in the 3γ trigger sample by mis-identification of the charged track ($K_{\pi 2\gamma}$, $K_{\pi 3}$, $K_{e 3}$, $K_{e 3\gamma}$), mis-counting of the number of photons which might occur due to accidental hits ($K_{\mu 3}$), photon detection inefficiency ($K_{\pi 3}$), fused cluster ($K_{\pi 3}$), or the two photons from π^0 reconstructed as three showers ($K_{\mu 3}$).

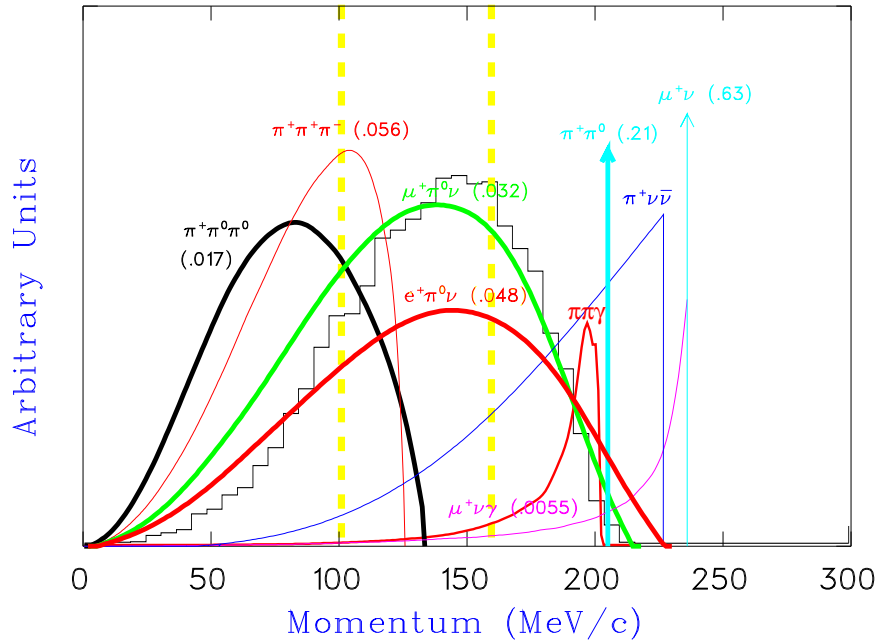


Figure 5.1: Momentum distribution of the charged particles from K^+ decays at rest. The solid histogram shows the distribution of the muon from $K_{\mu 3\gamma}$.

5.2 $K_{\mu 3}$ background

$K_{\mu 3}$ decays associated with an extra cluster in the BV due to accidental hits were called the “ $K_{\mu 3}$ -1” background. The $K_{\mu 3}$ -1 background was studied with real data from the 3γ trigger. In order to study the accidental hits in the BV, the photon whose timing relative to the muon time, Δt_γ , was most deviated was examined. As the side-band for the background study, the off-timing region ($|\Delta t_{\gamma_1}| > 3\text{nsec}$, $|\Delta t_{\gamma_2}| < 2\text{nsec}$, $|\Delta t_{\gamma_3}| < 2\text{nsec}$ or $|\Delta t_{\gamma_1}| < 2\text{nsec}$, $|\Delta t_{\gamma_2}| > 3\text{nsec}$, $|\Delta t_{\gamma_3}| < 2\text{nsec}$ or $|\Delta t_{\gamma_1}| < 2\text{nsec}$, $|\Delta t_{\gamma_2}| < 2\text{nsec}$, $|\Delta t_{\gamma_3}| > 3\text{nsec}$) was selected from the events which satisfied all the offline cuts except for the photon timing cut ($|\Delta t_\gamma| < 2\text{nsec}$). The Δt_γ distributions of the two photons to form the π^0 and of the radiative photon are shown in Fig. 5.2. Fig. 5.3 shows the $\cos \theta_{\mu\gamma}$ vs E_γ plot of the events with a photon on the interval $3 < |\Delta t_\gamma| < 6\text{nsec}$ in real data; the number of events in the signal region was 11. The number of background events in the signal region ($|\Delta t_{\gamma_1}| < 2.0\text{nsec}$, $|\Delta t_{\gamma_2}| < 2\text{nsec}$, $|\Delta t_{\gamma_3}| < 2\text{nsec}$) was estimated with the assumption that the timing distribution of the BV cluster due to accidental hits was constant. The background level was estimated to be $11/(6\text{nsec}/4\text{nsec})=7.3 \pm 2.2$ events.

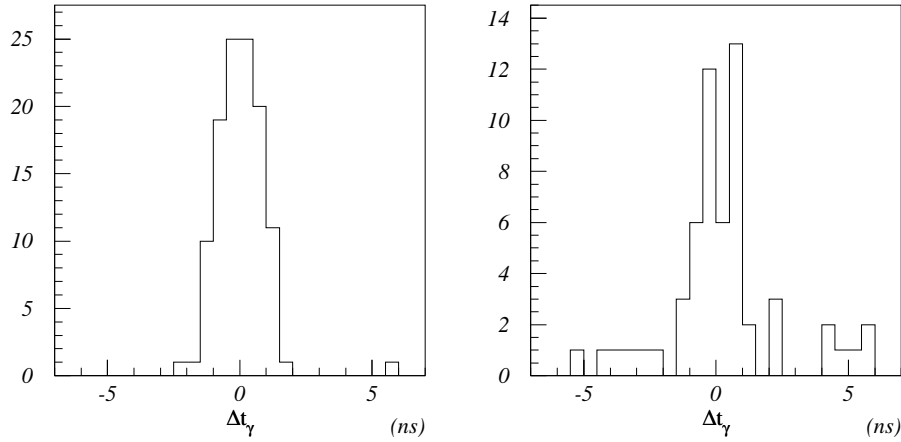


Figure 5.2: Δt_γ distributions of the two photons to form the π^0 (left) and of the radiative photon (right) in real data.

$K_{\mu 3}$ decays associated with an extra cluster in the BV when the showers due to the two photons from π^0 were reconstructed as three showers, i.e. when a shower was reconstructed as two clusters in the BV, were called the “ $K_{\mu 3}$ -2” background. Since it was difficult to isolate the sample of the $K_{\mu 3}$ -2 background from the real data, the background was studied with the sample generated by Monte Carlo simulation. A total of 2.3567×10^{10} $K_{\mu 3}$ decays were generated, and no event survived after imposing all the cuts. The background level of $K_{\mu 3}$ -2 was estimated to be < 0.35 events at the 90% C.L. by normalizing it with the sensitivity of this measurement (in Chapter 6) and was omitted from the background estimate.

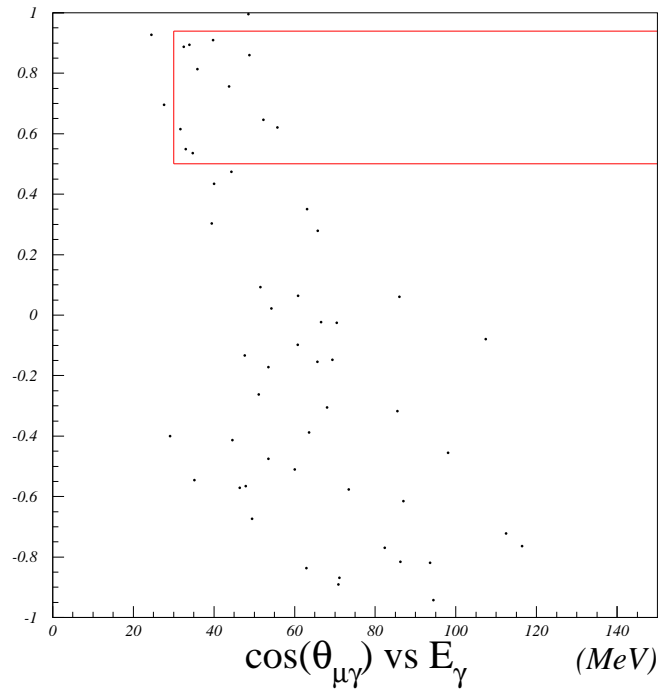


Figure 5.3: Distribution in $\cos \theta_{\mu\gamma}$ vs E_γ of events selected as the $K_{\mu 3-1}$ backgrounds. The box indicates the signal region.

5.3 $K_{\pi 2\gamma}$ background

$K_{\pi 2\gamma}$ decay events in which the π^+ was misidentified as a muon or decayed in flight before it came to rest in the RS were called the $K_{\pi 2\gamma}$ background. Since it was difficult to isolate the sample of the $K_{\pi 2\gamma}$ background from the real data, the background was studied with the sample generated by Monte Carlo simulation. A total of 5.20×10^8 $K_{\pi 2\gamma}$ decays with the photon emitted by Inner Bremsstrahlung (described later in subsection 6.3.1) were generated, and 22 events survived after imposing all the cuts. The background level of $K_{\pi 2\gamma}$ was estimated to be 0.38 ± 0.08 events by normalizing it with the sensitivity of this measurement. The reliability of the $K_{\pi 2\gamma}$ Monte Carlo was confirmed by the comparison between the peak in the missing energy (E_ν) distributions of the real data and Monte Carlo for the charged tracks that satisfied the range-momentum relation of π^+ (Fig. 5.4).

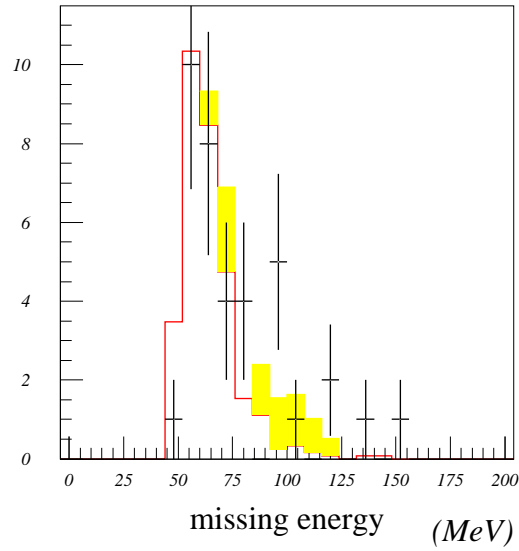


Figure 5.4: Missing energy distributions of real data (black) and $K_{\pi 2\gamma}$ (red) and $K_{\pi 3}$ (yellow) Monte Carlo for the charged tracks that satisfied the range-momentum relation of the π^+ . In this plot, the missing energy cut $E_\gamma < 60$ MeV was not applied

5.4 $K_{e3(\gamma)}$ background

$K_{e3\gamma}$ decays for which the e^+ was misidentified as a muon, or K_{e3} decays with the e^+ misidentification and an extra cluster in the BV or a photon due to bremsstrahlung were called the “ $K_{e3(\gamma)}$ ” background. The $K_{e3(\gamma)}$ background was studied with the real data by using the dE/dx cut to the charged track. The dE/dx cut was inverted to enhance the e^+ track events, but no event was left after imposing all the other analysis cut. In order to study the performance of the dE/dx cut, the events with the charged tracks which did not satisfy the range-momentum relation of μ^+ nor π^+ (Fig. 5.5(left)) were selected as the e^+ track events ($M = 236865$ events in total). After the inverted

dE/dx cut was imposed, $N = 162288$ events survived (Fig. 5.5(right)); the tagging efficiency of the inverted dE/dx cut was estimated to be $N/M = 162288/236865 = 0.685$. The further rejection of the dE/dx cut on e^+ track was also estimated to be $M/(M - N) = 236865/74577 = 3.18$. By combining these, the background level of $K_{e3(\gamma)}$ was estimated to be $< (2.3/0.685) \times 1/3.18 = 1.1$ events at the 90% C.L. and was omitted from the background estimate.

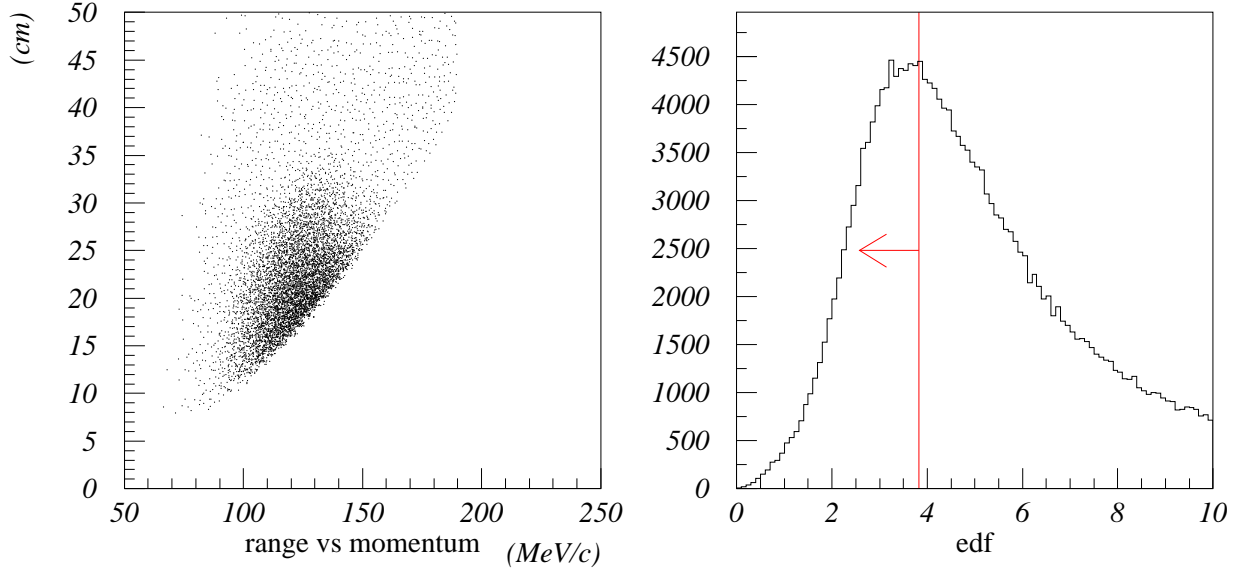


Figure 5.5: Range vs momentum plot of the charged tracks selected as the e^+ track events (left); distribution of the variable edf used in the dE/dx cut for the e^+ track events (right).

5.5 $K_{\pi 3}$ background

5.5.1 overview

$K_{\pi 3}$ decays in which the π^+ was misidentified as a muon or decayed in flight before it came to rest in the RS, and at the same time one of the four photons from two π^0 was undetected, were called the $K_{\pi 3}$ background. The disappearance of a photon was either of the three mechanisms: through inefficiency due to very narrow gaps between counters, inactive material, etc. in the BV, through the inefficiency in the other subsystems: Endcap, Range Stack, target, I-counters, and collar and micro collar counters, or through the fused cluster in the BV. The $K_{\pi 3}$ background was studied with the real data, in particular, with the muon identification cuts and the cuts to veto the undetected photon.

5.5.2 Bifurcation technique

In the E787 experiment, for background studies with the real data, an analysis technique named “bifurcation” was developed. Two independent sets of offline cuts were established for each type (or mechanism) of backgrounds. At least one of these cuts was inverted during the background studies in order to enhance the background events collected by the 3γ trigger as well as to prevent candidate events from being examined before the studies were completed. In order to avoid contamination from other background sources, all the offline cuts except for those being established were imposed on the data.

In order to explain the bifurcation technique, a simplified case is presented (Fig. 5.6). The two independent sets of cuts are named as “cut1” and “cut2”, respectively. All the cuts except for the cut1 and cut2 are called the “setup cuts”. After the setup cuts are imposed, there should remain only the events due to the specific background source (designated as type- i) and the signal events. In Fig. 5.6, the events in each of the regions A, B, C, and D are:

$$\begin{aligned} N_A &= \#signal + \#BG_A^i, \\ N_B &= \#BG_B^i, \\ N_C &= \#BG_C^i, \\ N_D &= \#BG_D^i, \end{aligned}$$

where N_A , N_B , N_C , and N_D are the numbers of events in the regions, and $\#BG_X^i$ represents the number of the background events in the region X . The region A is considered to be the region where the signal events are concentrated, and $\#signal$ is the number of signal events in it. The regions B, C, and D mean the cut1, the cut2, and both the cut1 and cut2 are inverted and thus are set to be looser than in the signal region, respectively, and are thought to be the regions where the background events are enhanced.

If cut1 and cut2 are uncorrelated, $\#BG_A^i/\#BG_B^i$ should be equal to $\#BG_C^i/\#BG_D^i$. Thus, the background level in the region A (the signal region), $\#BG_A^i$, can be estimated from the observed number of events in the other regions as $\#BG_B^i \times (\#BG_C^i/\#BG_D^i) = N_B \times N_C/N_D = N_B/(N_D/N_C)$, where the ratio of N_D/N_C is particularly called as the rejection factor or “Rejection (R)”.

In the $K_{\pi 3}$ background studies, the cut1 was the range-momentum relation cuts for muon identification and the cut2 was the number-of-photon cut (to the inefficiency of the BV), the photon veto cuts (to the inefficiency of the other subsystems), or the fused cluster cuts (to the fused cluster in the BV). To invert cut1, the events with the charged track that satisfied the range-momentum relation of π^+ (“ π -band events”) were selected; the momentum was also required to be less than

115 MeV/c to select the $K_{\pi 3}$ events and to remove the $K_{\pi 2\gamma}$ events. To invert cut2, the events which failed the number-of-photon cut, the photon veto cuts, or the fused cluster cuts were selected.

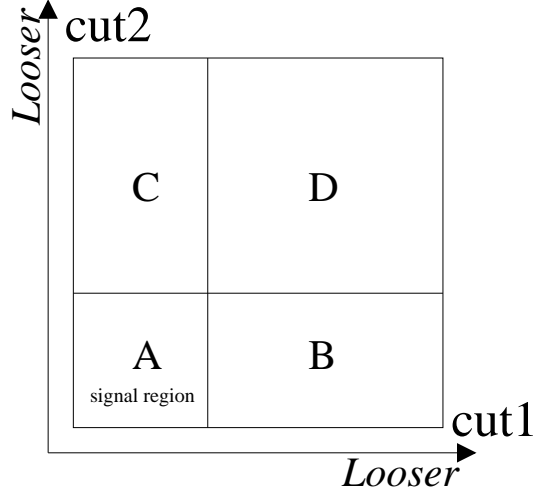


Figure 5.6: Pictorial explanation of the bifurcation method.

5.5.3 Photon inefficiency of the BV

The background due to the photon inefficiency of the BV was studied with the number-of-photon cut (Fig. 5.7). $K_{\pi 3}$ decays were tagged by the requirement that the number of photons in BV was equal to 4 ; this requirement is abbreviated as “NG4” in Fig. 5.7. The tagging efficiency of “NG4” to the $K_{\pi 3}$ decay was measured in the right branch in Fig. 5.7, in which the $K_{\pi 3}$ sample was selected by the low-momentum charged tracks (<115 MeV/c) in the π -band events. The ratio of the number of the NG4 events to the total sample ($\varepsilon \equiv N_1/N_2 = 3330/3779 = 0.881$) was regarded as the tagging efficiency. The rejection R of the number-of-photon cut, i.e. the requirement that the number of clusters is exactly three (abbreviated as “NG3” in Fig. 5.7), was also estimated in the right branch. Additional cuts (labeled as the “no overlap tagging & missing direction” cuts) were imposed in the right branch to avoid the contribution of other two $K_{\pi 3}$ background mechanisms. The “missing direction” cut required that the missing momentum should go to the BV region. The BV region was defined with the cosine of the polar angle of the missing momentum to be from -0.7 to 0.7. The “no overlap tagging” is described in the next subsection. The rejection R was estimated with the ratio of the number of events after imposing the “no overlap tagging & missing direction” cuts, $M_2 = 383$, to the number of events in which only three photons were observed in the BV, $M_1 = 56$, as $R = M_2/M_1 = 383/56 = 6.8$. In the left branch for normalization, all the cuts except for NG3 were imposed to the tagged $K_{\pi 3}$ events. Figure 5.8 shows the $\cos \theta_{\mu\gamma}$ vs E_γ plot of the events after imposing the cuts in real data; the number of events in the signal region was 45. Finally, the number of backgrounds was estimated to be:

$$\begin{aligned} n/\varepsilon \times 1/R &= 45/0.881 \times 1/6.8 \\ &= 7.5 \pm 1.5. \end{aligned}$$

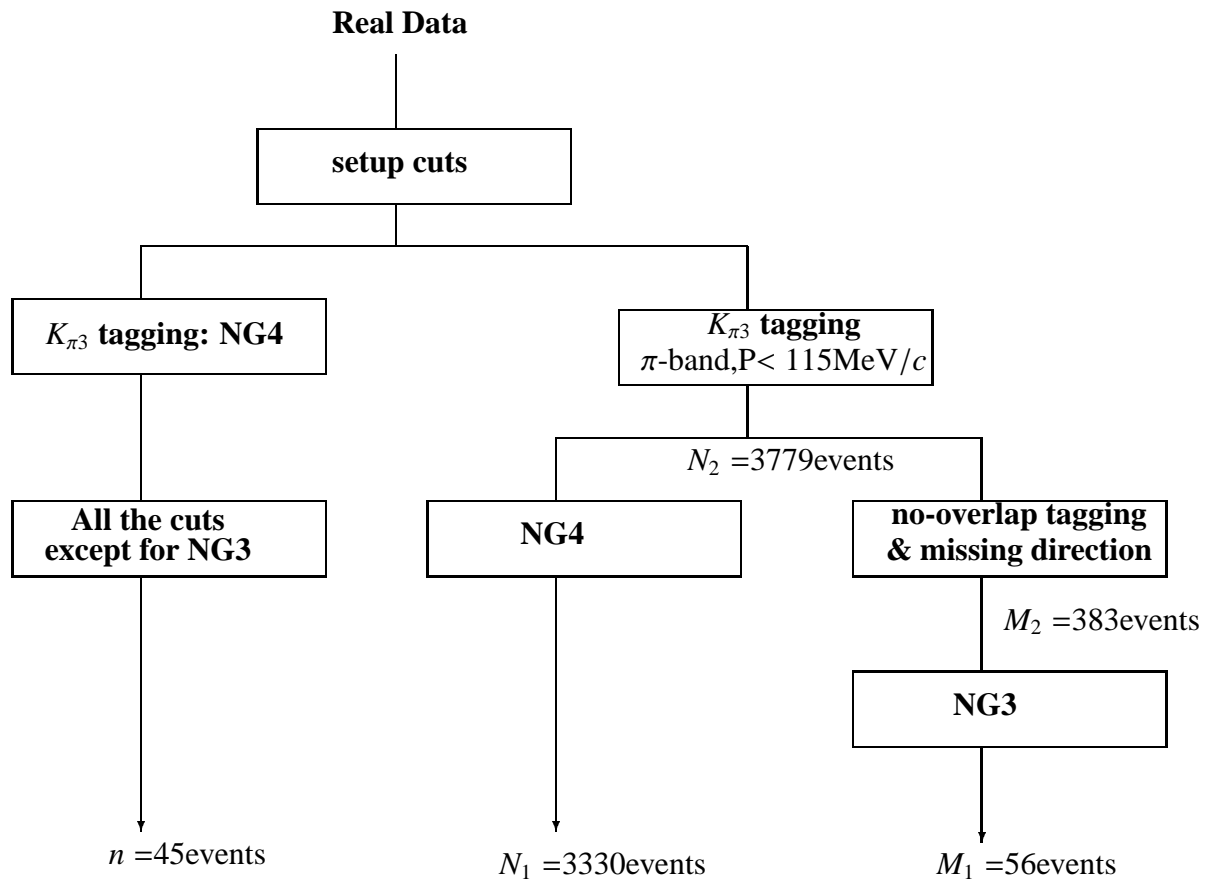


Figure 5.7: Bifurcation chart for the $K_{\pi 3}$ background through the inefficiency of the BV.

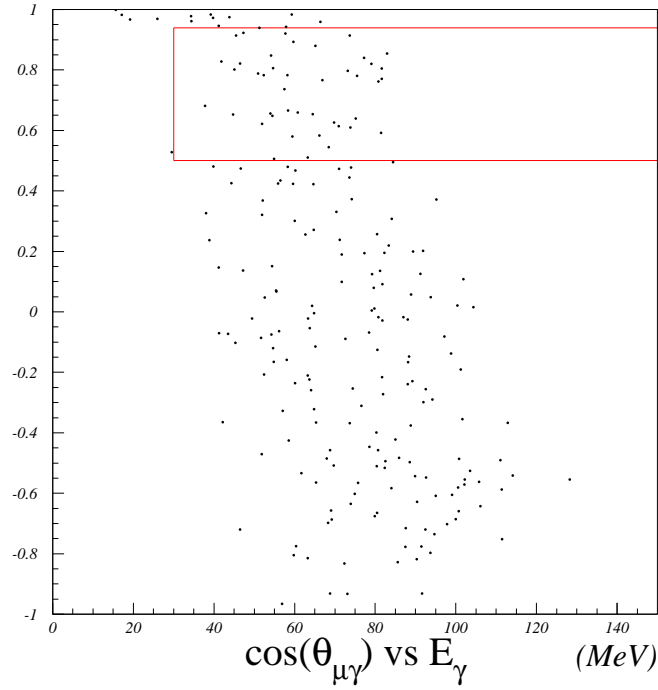


Figure 5.8: Distribution in $\cos \theta_{\mu\gamma}$ vs E_{γ} of events selected as the $K_{\pi 3}$ BV inefficiency background. The box indicates the signal region.

5.5.4 Photon inefficiency of the other subsystems

The $K_{\pi 3}$ background due to the photon inefficiency of the other subsystems was studied with the photon veto cuts (Fig. 5.9). $K_{\pi 3}$ decays were tagged by the inversion of the photon veto cuts (detection of the activity due to an extra photon in the other subsystems than the BV). The tagging efficiency of the inverted photon-veto cuts to the $K_{\pi 3}$ decay was measured in the right branch in Fig. 5.9, in which the $K_{\pi 3}$ sample was selected by the low-momentum charged tracks (< 115 MeV/c) in the π -band events. The ratio of the number of the events which satisfied the inverted photon-veto cuts to the total sample ($\varepsilon \equiv N_1/N_2 = 430/824 = 0.522$) was regarded as the tagging efficiency. The rejection R of the photon veto cuts (abbreviated as the “PV cut” in Fig. 5.9) was also estimated in the right branch. An additional cut on the direction of the missing energy in the kinematic fit (labeled as the “direction of missing momentum” cut in Fig. 5.9) was imposed in the right branch so that the undetected photon from the $K_{\pi 3}$ decay should go to the direction other than the BV. On the other hand, the “missing direction” cut in Fig. 5.7 (and Fig. 5.10) required the undetected photon from the $K_{\pi 3}$ should go to the direction of BV. The accepted region was $[-0.9, -0.7]$ or $[0.7, 0.9]$ in the cosine of the polar angle of the direction of the missing momentum. The rejection R was estimated with the ratio of the number of events after imposing the “direction of missing momentum” cuts, $M_2 = 227$, to the number of events which survived the photon veto cuts, $M_1 = 49$, as $R = 227/49 = 4.6$. In the left branch for normalization, all the cuts except for the photon veto cuts were imposed to the tagged $K_{\pi 3}$ events and the number of remaining events ($n = 2$) was counted. Finally, the number of backgrounds was estimated to be:

$$\begin{aligned} n/\varepsilon \times 1/R &= 2/0.552 \times 1/4.6 \\ &= 0.8 \pm 0.6. \end{aligned}$$

5.5.5 Fused cluster in the BV

The $K_{\pi 3}$ background due to the fused cluster in the BV was studied with the fused cluster cuts, i.e. the *DPSQ* and *CHKSPZ* cuts (Fig. 5.10). $K_{\pi 3}$ decays were tagged by the requirement that $DPSQ < 21$ and $18 < CHKSPZ < 60$ in Fig. 4.5 in page 48; this requirement is labeled as the “overlapped photons” cut in Fig. 5.10, and was to invert the fused cluster cuts (detection of the fused cluster in the BV). The tagging efficiency of “overlapped photons” to the $K_{\pi 3}$ decay was measured in the right branch in Fig. 5.10, in which the $K_{\pi 3}$ sample was selected by the low-momentum charged tracks (< 115 MeV/c) in the π -band events. The ratio of the number of the “overlapped photons” events to the total sample ($\varepsilon \equiv N_1/N_2 = 729/1754 = 0.416$) was regarded as the tagging efficiency. The rejection R of the fused cluster cuts (abbreviated as the “OVP cut” in Fig. 5.10) was also estimated in the right branch. Additional cuts, label as the “No BV inefficiency” cut in Fig. 5.10, was imposed in the right branch.

To develop this cut, a new variable *chkcc1* was defined to the Monte Carlo $K_{\pi 3}$ events, as the cosine of the minimum of the opening angles between the undetected photon (true values in Monte Carlo generation) and the photon clusters reconstructed in the BV; the events with the *chkcc1* close to 1.0 are considered to be the fused-cluster events in the BV. From Fig. 5.11 (left), it was confirmed that the requirement on the missing energy E_γ in the kinematic fit to be $E_\gamma < 60$ MeV enhanced the fused cluster events. On the other hand, the cosine of the minimum of the opening angles between the missing momentum in the kinematic fit and the photon clusters in the BV, $\cos \theta_{min} (\equiv \max(\cos \theta_{\gamma\gamma_1}, \cos \theta_{\gamma\gamma_2}, \cos \theta_{\gamma\gamma_3}))$ was calculated and, from Fig. 5.10 (right), it was found that the fused cluster events (*chkcc1* ~ 1.0) can be avoided with a negative value of $\cos \theta_{min}$. In the “no overlap tagging” in Fig. 5.7 for the $K_{\pi 3}$ background through the inefficiency of the BV, the

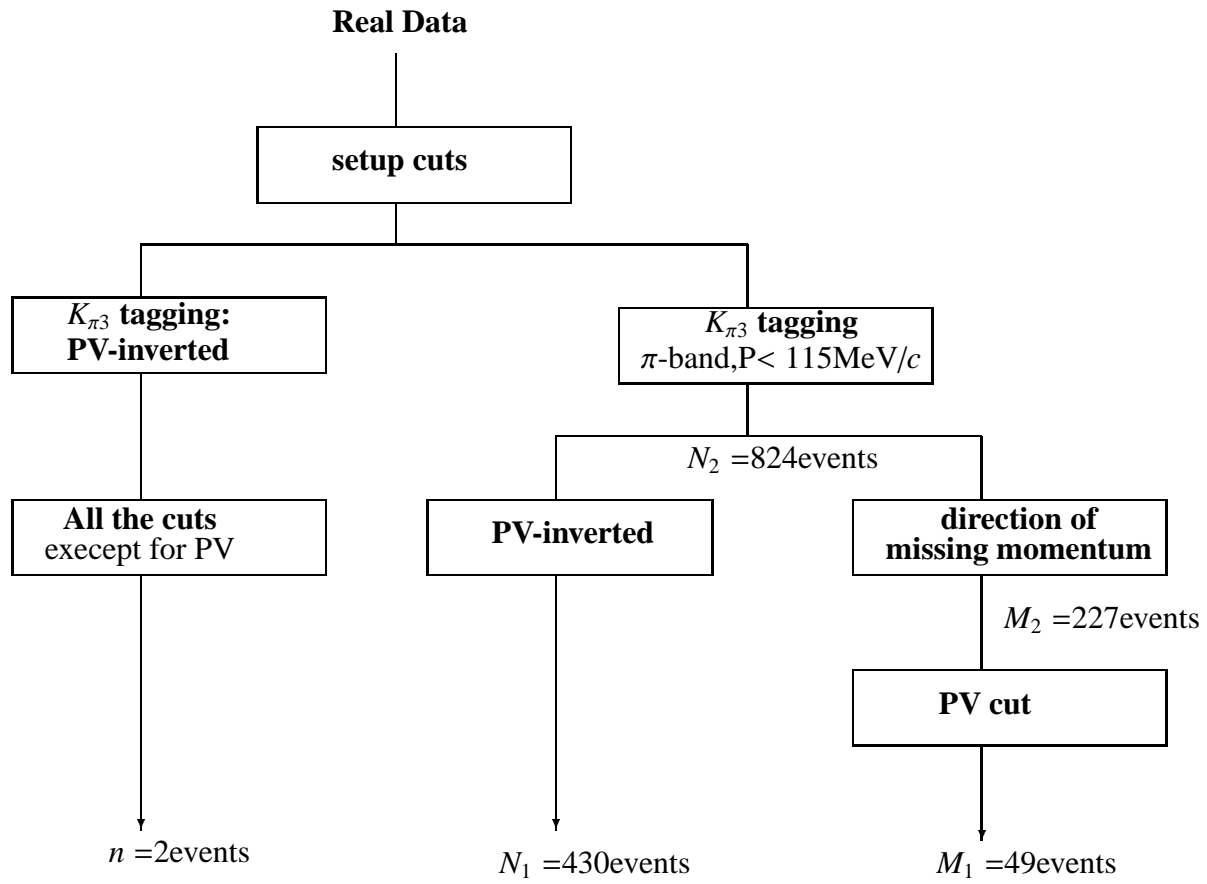


Figure 5.9: Bifurcation chart for the $K_{\pi 3}$ background through the inefficiency of the other subsystems.

requirement $\cos \theta_{min} < 0.0$ was used. The rejection R was estimated with the ratio of the number of events after imposing the “No BV inefficiency” cut, $M_2 = 878$, to the number of events which survived the fused cluster cuts, $M_1 = 95$, as $R = 878/95 = 9.2$. In the left branch for normalization, all the cuts except for the fused cluster cuts were imposed to the tagged $K_{\pi 3}$ events and the number of remaining events ($n = 2$) was counted. Finally, the number of backgrounds was estimated to be:

$$\begin{aligned}
 n/\varepsilon \times 1/R &= 2/0.416 \times 1/9.2 \\
 &= 0.5 \pm 0.4.
 \end{aligned}$$

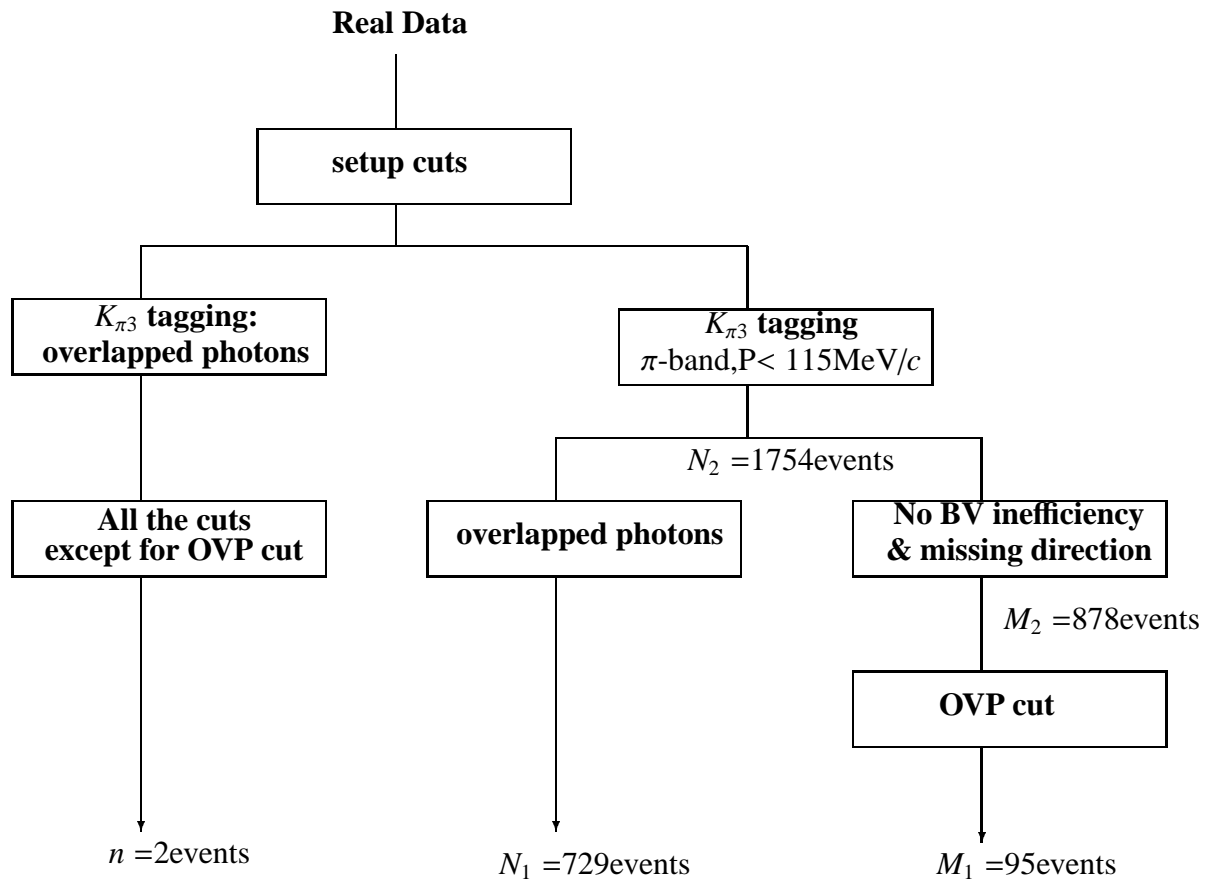


Figure 5.10: Bifurcation chart for the $K_{\pi 3}$ background through the fused cluster in the BV.

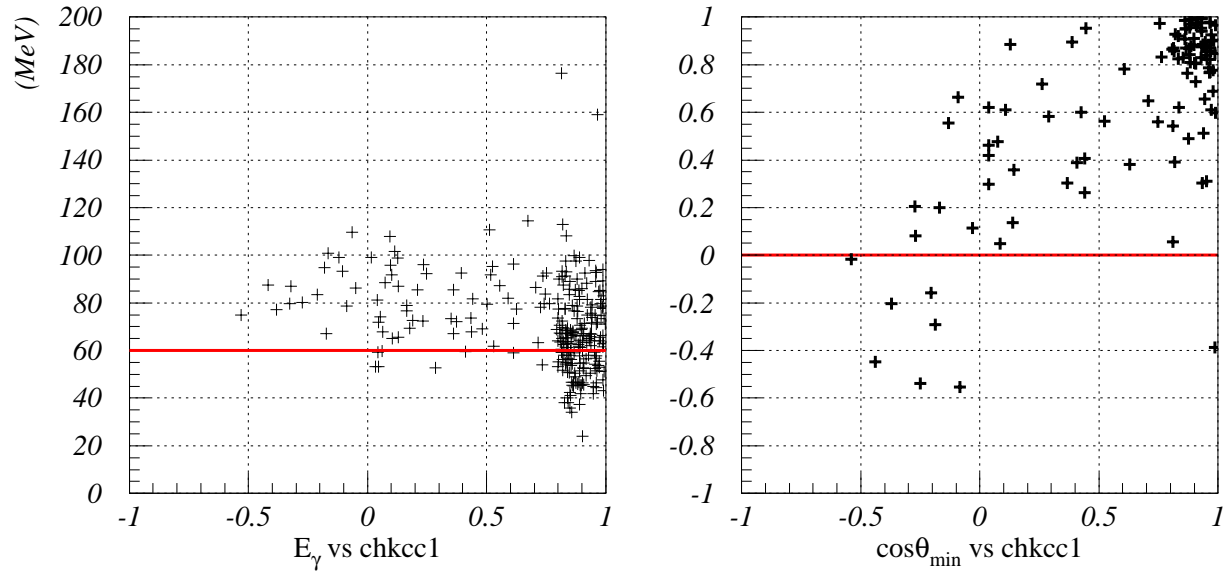


Figure 5.11: Distributions of the missing energy E_γ vs $chkccl$ (left) and $\cos\theta_{min}$ vs $chkccl$ (right) in the Monte Carlo $K_{\pi 3}$ events.

5.5.6 summary of the $K_{\pi 3}$ background

The background levels of $K_{\pi 3}$ due to the photon disappearance through three mechanism: the inefficiency of the BV, the inefficiency of the other subsystems, and the fused cluster in the BV were estimated to be 7.5 ± 1.5 events, 0.8 ± 0.6 events, and 0.5 ± 0.4 events, respectively; the first mechanism was dominant. After combining them, the background level of $K_{\pi 3}$ was 8.8 ± 1.6 events in total.

5.6 Summary of the background levels

The background levels are summarized in Table 5.1. In total, 16.5 ± 2.7 background events were expected in the signal region.

Sources	Background level	Sample
$K_{\mu 3-1}$	7.33 ± 2.2	Data
$K_{\mu 3-2}$	< 0.35 (90%CL)	M.C.
$K_{\pi 2\gamma}$	0.38 ± 0.08	M.C.
$K_{e 3(\gamma)}$	< 1.06 (90%CL)	Data
$K_{\pi 3}$	8.81 ± 1.61	Data
All Backgrounds	16.5 ± 2.7	-

Table 5.1: Expected background levels in the signal region. “Data” and “MC” in the rightmost column indicate whether real data or Monte Carlo simulation were used for the estimation, respectively.

Chapter 6

Sensitivity for $K^+ \rightarrow \pi^0 \mu^+ \nu_\mu \gamma$

6.1 Acceptance factors

The acceptance factors for the selection criteria in this measurement were estimated primarily from Monte Carlo simulation. We generated the $K_{\mu 3\gamma}$ sample at $O(p^4)$ in ChPT with $E_\gamma > 20$ MeV. The energy threshold in Monte Carlo was set to be lower than the offline criteria on the photon energy, in particular the *egcut* cut; thus, the acceptance factors and the single event sensitivity in this chapter are for the $K_{\mu 3\gamma}$ decay in the kinematic region $E_\gamma > 20$ MeV. In later, we will first obtain the partial branching ratio for $K_{\mu 3\gamma}$ in this kinematic region and then convert it into $Br(K_{\mu 3\gamma}, E > 30 \text{ MeV}, \theta_{\mu\gamma} > 20^\circ)$ and $Br(K_{\mu 3\gamma}, 30 < E_\gamma < 60 \text{ MeV})$.

A total of 9.32×10^8 $K_{\mu 3\gamma}$ decays were generated, and 8157 events survived all the online and offline cuts except for the beam cuts and target cuts. The acceptance factors are summarized in Tables 6.1 to 6.7.

cut	# of events	acceptance
($K_{\mu 3\gamma}$ decay)	932000000	-
KB	931933572	1.000
$T \cdot 2$	268055475	0.288
DC	268054941	1.000
$3_{ct} + 4_{ct}$	236294968	0.882
$7_{ct} + 8_{ct}$	130357559	0.552
total		0.140

Table 6.1: Acceptance factors for the muon trigger component based on Monte Carlo simulation.

cut	# of events	acceptance
(muon trigger component)	130357559	-
$(9 + \dots + 21)$	24152859	0.185
\overline{EC}	7417335	0.307
HEX	6764845	0.912
$NG3$	794284	0.117
total		6.09×10^{-3}

Table 6.2: Acceptance factors for the photon trigger component based on Monte Carlo simulation.

cut	# of events	acceptance
(photon trigger component)	794284	-
charged track reconstruction and itgqualt cut	714394	0.899
cos3d cut	698233	0.977
stopping layer cut	697005	0.998
ptot cut	697005	1.000
delayed coincidence cut	592802	0.851
total		0.746

Table 6.3: Acceptance factors for the primary selection based on Monte Carlo simulation.

cut	# of events	acceptance
(primary selection)	592802	-
range-momentum relation cuts	540521	0.912
dE/dx cut	536053	0.992
number of photon cut	515922	0.962
photon timing cut	468102	0.907
photon veto cuts	377620	0.807
$egcut$ cut	205696	0.545
fused cluster cut	145702	0.708
e^+ bremsstrahlung cut	130296	0.894
total		0.220

Table 6.4: Acceptance factors for the selection of muon and photons based on Monte Carlo simulation.

The acceptance factors for the beam cuts and the target cuts were measured with the data sample of $K^+ \rightarrow \mu^+ \nu_\mu$ decays simultaneously accumulated with the $Kmu2(1)$ trigger. After the selection of the monochromatic peaks in the momentum, range, and kinetic energy of the muons from $K_{\mu 2}$ and imposing the itgqualt cut, online and offline photon veto cuts, the delayed coincidence cut and the cos3d cut, 457457 events remained. Then, after imposing the beam cuts and the target cuts, 313044 events survived as summarized in Table 6.8; the acceptance factors were 0.684 in total. After combining the factors in Table 6.3 and Table 6.8, the acceptance factors for the primary selection was 0.511 in total.

cut	# of events	acceptance
(selection of muon and photons)	130296	-
$K_{\mu 3\gamma}$ likelihood cut	117908	0.905
$K_{\mu 3}$ likelihood cut	35783	0.303
total		0.275

Table 6.5: Acceptance factors for the kinematic fit based on Monte Carlo simulation.

cut	# of events	acceptance
(kinematic fit)	35783	-
missing energy cut	30825	0.861
$M_{\mu\nu}$ cut	24321	0.789
θ_ν cut	23237	0.955
total		0.649

Table 6.6: Acceptance factors for the cuts after the kinematic fit based on Monte Carlo simulation.

6.2 Accidental loss

The 3gamma trigger was defined as follows.

$$KB \cdot DC \cdot T \bullet 2 \cdot (3_{ct} + 4_{ct}) \cdot \overline{(7_{ct} + 8_{ct})} \cdot \overline{(9 + \dots + 21)} \cdot \overline{EC} \cdot HEX \cdot NG3 \cdot prescale$$

The veto conditions in the trigger: $\overline{(7_{ct} + 8_{ct})}$, $\overline{(9 + \dots + 21)}$, \overline{EC} and HEX suffer the acceptance loss by the accidental hits. For the estimation, the data samples of $K_{\mu 2}$ decays and scattered beam pions, which were simultaneously accumulated by the $Kpi2(1)$ trigger and the $Piscat$ trigger, respectively, were used. These triggers were defined as follows:

$$\begin{aligned} Kpi2(1) &= KB \cdot T \bullet 2 \cdot (6_{ct} + 7_{ct}) \cdot \overline{(19_{ct} + 20_{ct} + 21_{ct})} \\ Piscat &= piB \cdot \overline{DC} \cdot IC \cdot T \bullet 2 \cdot (6_{ct} + 7_{ct}) \cdot \overline{(20 + 21)} \cdot \overline{BV + EC} \cdot HEX \end{aligned}$$

At first, the accidental loss due to the \overline{EC} and HEX cuts was determined by the $K_{\mu 2}$ sample in the $Kpi2(1)$ trigger. 1470 events were selected by the monochromatic peaks in the momentum, energy, and range of the $K_{\mu 2}$ whose RS stopping layers was up to layer 14. By imposing the \overline{EC} and HEX bits, 1298 events remained. The acceptance was thereby 0.883.

The accidental loss due to the range stack hits had to be estimated separately. The accidental loss due to layer $9 + \dots + 19$ was estimated by using the scattered beam pions in the $Piscat$ trigger. A total of 72213 events were selected by the requirements that the RS stopping layer was in layer 6 or layer 7, and the charged track was in the pion band, and with the \overline{EC} and HEX bits. After imposing the veto of $9 + \dots + 19$ to this sample, 55834 events remained. The acceptance was thereby 0.773.

The accidental loss due to layer $20+21$ was estimated by using the $K_{\mu 2}$ sample in the $Kp2(1)$ trigger. A total of 1160 events were selected by the monochromatic peaks in the range, energy and momentum of the muons from $K_{\mu 2}$ whose RS stopping layer was up to layer 14, \overline{EC} , HEX , and the layer $15 + \dots + 19$ veto. After imposing the layer $20+21$ veto, 1138 event remained. The acceptance for the layer $20+21$ veto was thereby 0.981 though there were uncertainties due to the requirement $\overline{(19_{ct} + 20_{ct} + 21_{ct})}$ already in the $Kpi2(1)$ trigger.

cut	# of events	acceptance
(cuts after the kinematic fit)	23237	-
$E_\gamma > 30 \text{ MeV}$	22956	0.988
$0.5 < \cos \theta_{\mu\gamma} < 0.94$	8157	0.355
total		0.351

Table 6.7: Acceptance factors for the signal region based on Monte Carlo simulation.

cut	#events	acceptance
itgqualt cut, momentum, range, kinetic energy, online photon veto cuts	624203	
delayed coincidence cut	540788	
cos3d cut	529699	
photon veto cut	457457	
target cuts	402636	0.880
beam cuts	313044	0.777
total		0.684

Table 6.8: Acceptance factors for the primary selection based on the data sample of $K^+ \rightarrow \mu^+ \nu_\mu$ decays.

The accidental loss due to $(7_{ct} + 8_{ct})$ was estimated by the offline analysis of the $K_{\mu 2}$ sample in the $K\pi 2(1)$ trigger. The activities of the RS modules in layer 7, 8 which were located in the ten sectors in the counterclockwise region were checked. The acceptance was estimated to be 0.999.

The acceptance factors with the loss due to the accidental hits are summarized in Table 6.9. After combining the factors, the acceptance factors were 0.669 in total.

trigger condition	acceptance
$\overline{EC \cdot HEX}$	0.883
$\overline{(9 + \dots + 19)}$	0.773
$\overline{20 + 21}$	0.981
$\overline{(7_{ct} + 8_{ct})}$	0.999
total	0.669

Table 6.9: Acceptance factors for the accidental loss based on the data samples of $K_{\mu 2}$ decays and scattered beam pions, respectively.

6.3 K^+ stop efficiency

The single event sensitivity (SES) for $K_{\mu 3\gamma}$ was derived from the total acceptance (including the accidental loss $\epsilon = 0.669$ in the previous section), the total exposure of kaons entering the target ($\text{KB_L} = 3.4894 \times 10^{11}$ in Section 2.4), and the fraction of kaons entering the target that decayed at rest, called the K^+ stop efficiency F_s . KB_L represents a scalar count of the number of incoming kaons while the DAQ system is ready to accept a new event, and was not equal to the number of

K^+ decays at rest in the target. Thus the ratio F_s of the number of K^+ decays to the number of incoming kaons should be estimated by data, and the ratio was called the K^+ stop efficiency. F_s was obtained by solving the following equation with respect to a specific K^+ decay mode whose branching ratio (Br) was well known and which was taken simultaneously with the $K^+ \rightarrow \pi^0 \mu^+ \nu_\mu \gamma$ decay.

$$(\# \text{ of observed events}) = \text{KB.L} \times Br \times Acc \times \epsilon \times F_s$$

ϵ is the same acceptance factor for the accidental loss used in the $K_{\mu 3 \gamma}$ sensitivity, and Acc is the acceptance to the K^+ decay mode. In the standard E787 experiment, the conventional method was to use the $K_{\mu 2}$ or $K_{\pi 2}$ decay. In this analysis, the decay modes accumulated in the same 3γ trigger, $K_{\pi 2 \gamma}$ and $K_{\pi 3}$, were used and were compared with the results with the standard method.

6.3.1 F_s from the $K_{\pi 2 \gamma}$ branching ratio

This method is basically the same as used in the '95 $K_{\pi 2 \gamma}$ analysis of E787 [40]. The $K^+ \rightarrow \pi^+ \pi^0 \gamma$ decay is dominated by Inner Bremsstrahlung (IB), which is QED radiative corrections to $K^+ \rightarrow \pi^+ \pi^0$, but also has the component in which the photon directly emitted (DE). In the π^+ kinetic-energy region $55 < T_{\pi^+} < 90$ MeV the theoretical prediction for the IB branching ratio is 2.61×10^{-4} , which was confirmed by experiments [23]. The branching ratio of the DE component in the same region was measured to be $(4.3 \pm 0.7) \times 10^{-6}$ [23]. For $K_{\pi 2 \gamma}$, the events collected with the 3γ trigger were further prescaled by 8 and were reconstructed with the assumption that the charged track was a π^+ : the presence of the additional 4 MeV deposit in the RS stopping counter due to the $\pi^+ \rightarrow \mu^+ \nu_\mu$ decay at rest was assumed and was subtracted from the observed energy. The kinematic fit with the assumption of the $K_{\pi 2 \gamma}$ decay was also applied to the events.

The procedure of event selection for $K_{\pi 2 \gamma}$ is summarized in Table 6.10. After imposing primary cuts except for the beam and target cuts, π^+ identification cuts, photon veto cuts and photon selection cuts, 8463 events survived. The missing momentum should be smaller than 100 MeV/c. (In reality, in the data reduction for $K_{\pi 2 \gamma}$, this cut was imposed as a primary cut.) In Table 6.10, the “prob” cut means the χ^2 probability of the kinematic fit was required to be more than 10% and the “prob2” cut means, among the three possible pairings of the three photons to form the π^0 , the value of the best χ^2 probability was twice or more as large as the value of the worst χ^2 probability. The π^+ momentum P_{π^+} should satisfy $140 < P_{\pi^+} < 180$ MeV/c. The polar angle of the radiative photon θ_γ should satisfy $|\cos \theta_\gamma| < 0.6$. Finally, a kinematic variable W was defined as

$$W^2 \equiv \frac{E_{\gamma 3}^2 (E_{\pi^+} - P_{\pi^+} \cos(\theta_{\pi\gamma}))}{m_K m_{\pi^+}^2},$$

where E_γ is the energy of the radiative photon and $\theta_{\pi^+ \gamma}$ is the angle between π^+ and the photon, and W was required to be larger than 0.1; this cut was needed for the $K_{\pi 2 \gamma}$ study. We observed 2425 $K_{\pi 2 \gamma}$ events.

9.64×10^8 IB $K_{\pi 2 \gamma}$ decays were generated by Monte Carlo in the region $20 < T_{\pi^+} < 95$ MeV. 279785 events survived all the online and offline cuts. Thus the acceptance was obtained to be $A_{umc} = 279785 / (9.64 \times 10^8) = (2.902 \pm 0.005) \times 10^{-4}$. The acceptance factors based on the Monte Carlo are also summarized in Table 6.10. The two background mechanisms to $K_{\pi 2 \gamma}$ were considered: one was due to charged-track misidentification, and the other was due to the accidental photon. Both of the background levels were estimated with the number of events observed in the side-band regions. Accidental photon backgrounds were estimated to be 11.3 ± 2.8 events. The charged-track misidentification backgrounds were estimated to be 74.9 ± 13.9 events. Thus, the background expectation to $K_{\pi 2 \gamma}$ events was 3.6%. The contribution from the DE component of $K_{\pi 2 \gamma}$ was also checked. The acceptance was estimated to be 3.094×10^{-4} by Monte Carlo. The

branching ratios were adopted from the PDG value in $55 \text{ MeV} < T_{\pi^+} < 90 \text{ MeV}$ and was scaled to extended to the kinetic region ($20 \text{ MeV} < T_{\pi^+} < 95 \text{ MeV}$), which were 4.12×10^{-4} for IB and 8.71×10^{-6} for DE, respectively. The contribution from the DE component to the IB $K_{\pi 2\gamma}$ events was estimated to be 2.2%.

F_s from the $K_{\pi 2\gamma}$ branching ratio was obtained as:

$$\begin{aligned} \#observed - \#background &= KB_L \times prescale \times (A_{unc}^{IB} \times Br^{IB} + A_{unc}^{DE} \times Br^{DE}) \times \epsilon \times F_s, \\ 2425 \times (1 - 0.036) &= 3.4864 \times 10^{11} \times 1/8 \times (2.902 \times 10^{-4} \times 4.12 \times 10^{-4}) \times (1 + 0.022) \times \epsilon \times F_s, \end{aligned}$$

and F_s was measured to be 0.669 ± 0.014 .

cut	real data		Monte Carlo	
	# of events	rejection	# of events	acceptance
(MC $K_{\pi 2\gamma}$ -IB decays)	-	-	9.64×10^8	-
trigger components and primary cuts	93397		1231970	0.00128
range-momentum relation cut for π^+	44354	2.11	1079005	0.876
photon veto cut	25313	1.75	850946	0.789
number of photon cut	16047	1.58	818872	0.962
photon timing cut	13692	1.17	744097	0.909
egcut cut	8463	1.62	480958	0.646
prob	3547	2.39	387401	0.805
prob2	3377	1.05	366907	0.947
$140 < P_{\pi^+} < 180 \text{ MeV}/c$	2633	1.28	301228	0.821
$ \cos \theta_\gamma < 0.6$	2498	1.05	287849	0.956
$W > 0.1$	2425	1.03	279785	0.972

Table 6.10: Data reduction and acceptance factors for the $K_{\pi 2\gamma}$ measurement.

6.3.2 F_s from the $K_{\pi 3}$ branching ratio

For a cross check, F_s from the $K_{\pi 3}$ decays in the 3γ trigger was also measured. In this case, background contamination was large due to the accidental γ background and the electron background ($K_{e3} + K_{e3\gamma}$). Both of them were estimated with the number of events observed in the side-band regions and were estimated to be 71.3 events and 250.6 events, respectively. The electron background was estimated by the dr_pi distribution (right plot of Fig. 6.1). dr_pi was defined by the difference of expected range assuming a π^+ track from the measured range. Assuming the electron backgrounds had a flat dr_pi distribution, the contamination was estimated. In the Monte Carlo, 3.0×10^8 $K_{\pi 3}$ decays were generated. F_s was estimated in the momentum range of the charged track from 100 MeV/c to 136 MeV/c, in which $K_{\pi 2\gamma}$ contamination is large (left plot of Fig. 6.1). In real data, 3942 events were observed in the region. Both of the contributions of $K_{\pi 3}$ and $K_{\pi 2\gamma}$ were used in the measurement of F_s .

$$\begin{aligned} \#observed - \#background &= KB_L \times prescale \times \epsilon \times F_s \times \sum_{i=K_{\pi 3}, K_{\pi 2\gamma}} (A_{unc}^i \times Br^i) \\ 3942 - (71.3 + 250.6) &= 3.4864 \times 10^{11} \times 1/8 \times \epsilon \times F_s \\ &\quad \times (9.513 \times 10^{-6} \times 1.73 \times 10^{-2} + 6.284 \times 10^{-5} \times 4.1168 \times 10^{-4}) \end{aligned}$$

F_s was measured to be 0.664 and was consistent with the measurement with $K_{\pi 2\gamma}$.

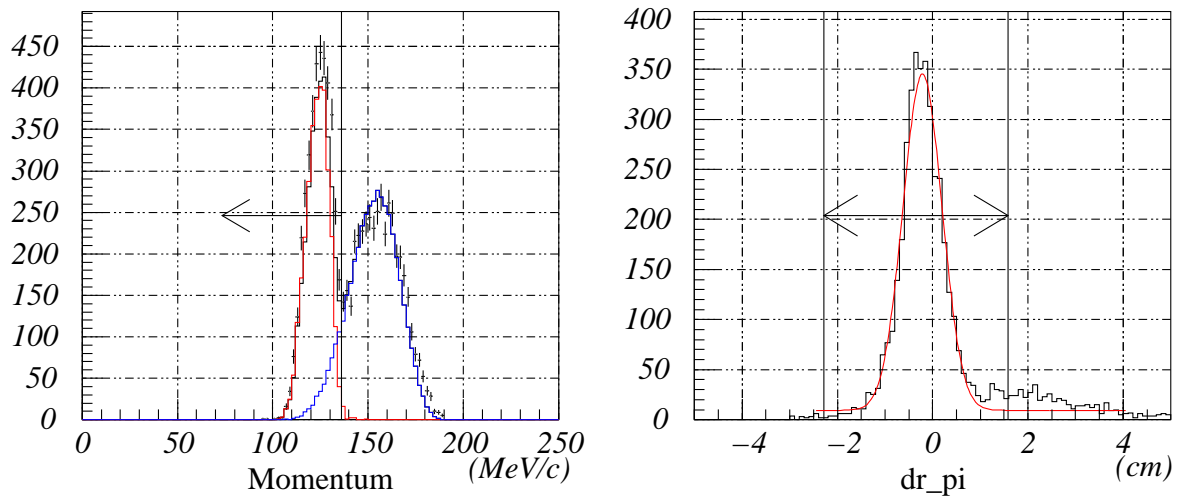


Figure 6.1: Momentum distributions (left): histogram with error (data), red histogram ($K_{\pi 3}$ M.C.), blue histogram ($K_{\pi 2\gamma}$ M.C.), black histogram ($K_{\pi 3}$ M.C. and $K_{\pi 2\gamma}$ M.C. are combined); dr_{π} distribution (right): the region defined by the arrow is the π -band region.

6.3.3 Summary on the K^+ stop efficiency

The F_s measurements with $K_{\pi 2\gamma}$ and $K_{\pi 3}$ were consistent to each other. They were also consistent with the values of F_s in other E787 analyses ($0.65 \sim 0.70$), though F_s was more or less analysis-dependent.

The $K_{\pi 3}$ Monte Carlo simulation in the kinematical region in this measurement was sensitive to the form factors in the matrix element, and the F_s with $K_{\pi 3}$ is less reliable than the F_s with $K_{\pi 2\gamma}$. $F_s = 0.669 \pm 0.014$, measured with the events of the IB component of the $K_{\pi 2\gamma}$ decay, was used in this analysis. Thus, the sensitivity for $K_{\mu 3\gamma}$ was normalized to $K_{\pi 2\gamma}$, and many systematic uncertainties in the acceptance factors are canceled.

6.4 Summary on the sensitivity

The acceptance factors for the $K_{\mu 3\gamma}$ decay in the kinematic region $E_\gamma > 20$ MeV, including the accidental loss (ϵ) discussed in Section 6.2, are summarized in Table 6.11. The total acceptance was 4.01×10^{-6} and was dominated by the trigger acceptance. With the total exposure of kaons entering the target (3.4894×10^{11}) and the K^+ stop efficiency 0.669 ± 0.014 , $SES = 1.07 \times 10^{-6}$ was obtained in the kinetic region $E_\gamma > 20$ MeV.

Acceptance factors	-
Muon trigger component	0.140
Photon trigger component	0.00609
Primary selection	0.511
Selection of muon and photons	0.220
Kinematic fit	0.275
Cuts after the kinematic fit	0.649
Signal region	0.351
Accidental loss (ϵ)	0.669
Total acceptance	4.01×10^{-6}

Table 6.11: Acceptance factors for the $K_{\mu 3\gamma}$ decay in the kinematic region $E_\gamma > 20$ MeV.

Chapter 7

Signal events

Figure 7.1 shows the cosine of $\theta_{\mu\gamma}$ vs E_γ plots of the events that survived all analysis cuts in real data (178 events) and in Monte Carlo $K_{\mu 3\gamma}$ simulation. The signal region was specified with $E_\gamma > 30$ MeV and $20^\circ < \theta_{\mu\gamma} < 60^\circ$ ($0.50 < \cos \theta_{\mu\gamma} < 0.94$). Figures 7.2 and 7.3 show the $\text{Prob}(\chi^2_{K_{\mu 3\gamma}})$ distributions and the $M_{\gamma\gamma}$ distributions of π^0 , respectively, from the events in the signal region in real data and in Monte Carlo $K_{\mu 3\gamma}$ simulation. Forty events were observed in the signal region.

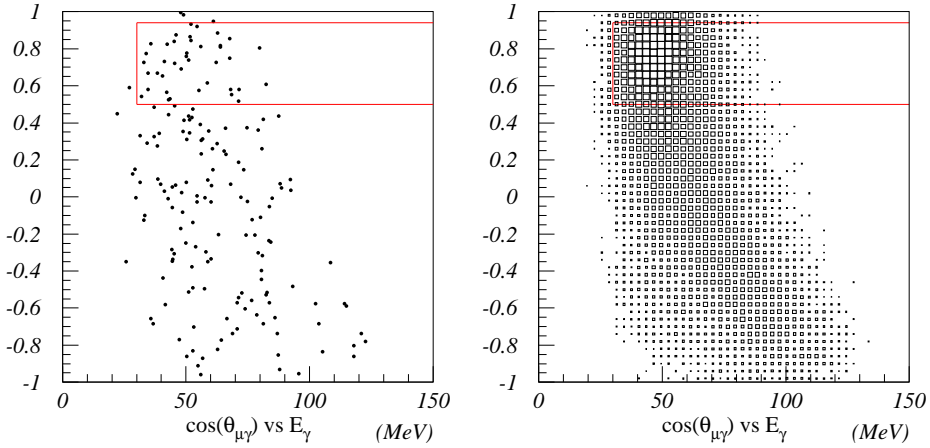


Figure 7.1: Cosine of $\theta_{\mu\gamma}$ vs E_γ plots of the events with all analysis cuts imposed in real data (left) and in the sample generated by Monte Carlo $K_{\mu 3\gamma}$ simulation (right). The box indicates the signal region.

From the 40 observed events, after subtracting the expected background (16.5 ± 2.7 events), $23.5 \pm 6.9(\text{stat.})$ $K_{\mu 3\gamma}$ events with the statistical uncertainty of 29% were obtained. With $\text{SES} = 1.07 \times 10^{-6}$, the partial branching ratio for $K_{\mu 3\gamma}$ in the kinematical region $E_\gamma > 20$ MeV was $(2.51 \pm 0.74(\text{stat.})) \times 10^{-5}$. To convert it into $\text{Br}(K_{\mu 3\gamma}, E_\gamma > 30 \text{ MeV}, \theta_{\mu\gamma} > 20^\circ)$ and $\text{Br}(K_{\mu 3\gamma}, 30 < E_\gamma < 60 \text{ MeV})$, the factors 0.628 and 0.437 estimated from the theoretical $K_{\mu 3\gamma}$ spectrum at $O(p^4)$ in ChPT were used; $\text{Br}(K_{\mu 3\gamma}, E_\gamma > 30 \text{ MeV}, \theta_{\mu\gamma} > 20^\circ) = (1.58 \pm 0.46(\text{stat.})) \times 10^{-5}$ and $\text{Br}(K_{\mu 3\gamma}, 30 < E_\gamma < 60 \text{ MeV}) = (1.10 \pm 0.32(\text{stat.})) \times 10^{-5}$. The systematic uncertainties are discussed in the next chapter.

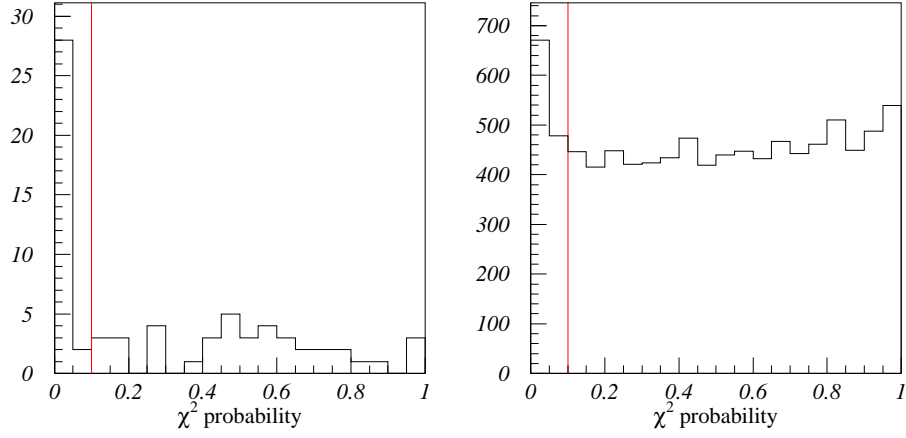


Figure 7.2: Distributions of $Prob(\chi^2_{K_{\mu 3\gamma}})$ from the events in the signal region in real data (left) and in the sample generated by Monte Carlo $K_{\mu 3\gamma}$ simulation (right). All selection cuts excepts for the cut $Prob(\chi^2_{K_{\mu 3\gamma}}) > 0.1$ are imposed.

The kinetic distributions of the observed 40 events were compared to the spectra predicted from the $K_{\mu 3\gamma}$ decay plus all the background contributions, as shown in Fig. 7.4. The $\chi^2/\text{degree-of-freedom}$ values to evaluate the match between data and predictions were 2.7/6, 11.3/8, 12.5/5, and 7.0/9 in the distributions of E_γ , π^0 energy, E_ν , and the muon momentum, respectively. The scatter plots of E_ν versus the range difference (dr_ratio defined in Sec. 4.2.1) in real data, Monte Carlo $K_{\pi 2\gamma}$, $K_{\mu 3}$, and $K_{\mu 3\gamma}$ events are shown in Fig. 7.5 to illustrate the distributions of background events outside the signal region with the distributions of E_ν versus dr_ratio . The isolation of the 40 candidate events from the backgrounds of $K_{\pi 3}$ and $K_{\pi 2\gamma}$ were observed in the real data plot. All the events observed in the signal region of the Monte Carlo $K_{\pi 2\gamma}$ events were due to the decay-in-flight of π^+ . One event observed in the signal region of the Monte Carlo $K_{\pi 3}$ events was also due to π^+ decay-in-flight.

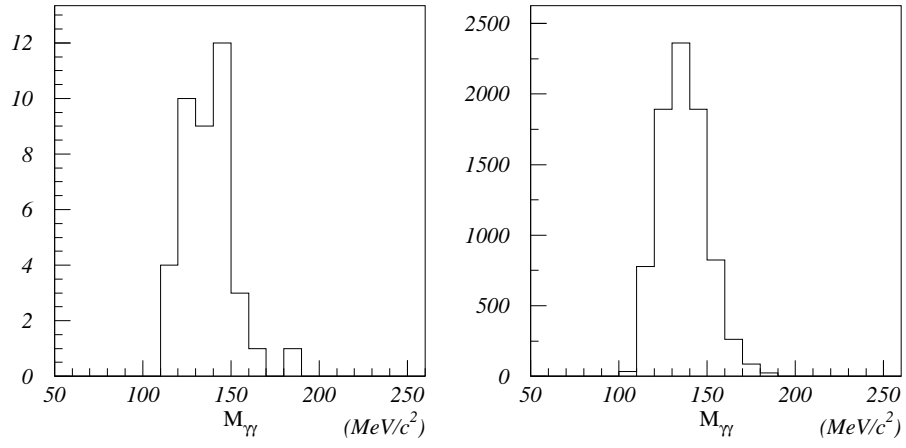


Figure 7.3: $M_{\gamma\gamma}$ distribution of the π^0 from the events in the signal region in real data (left) and the sample generated by Monte Carlo $K_{\mu 3\gamma}$ simulation (right).

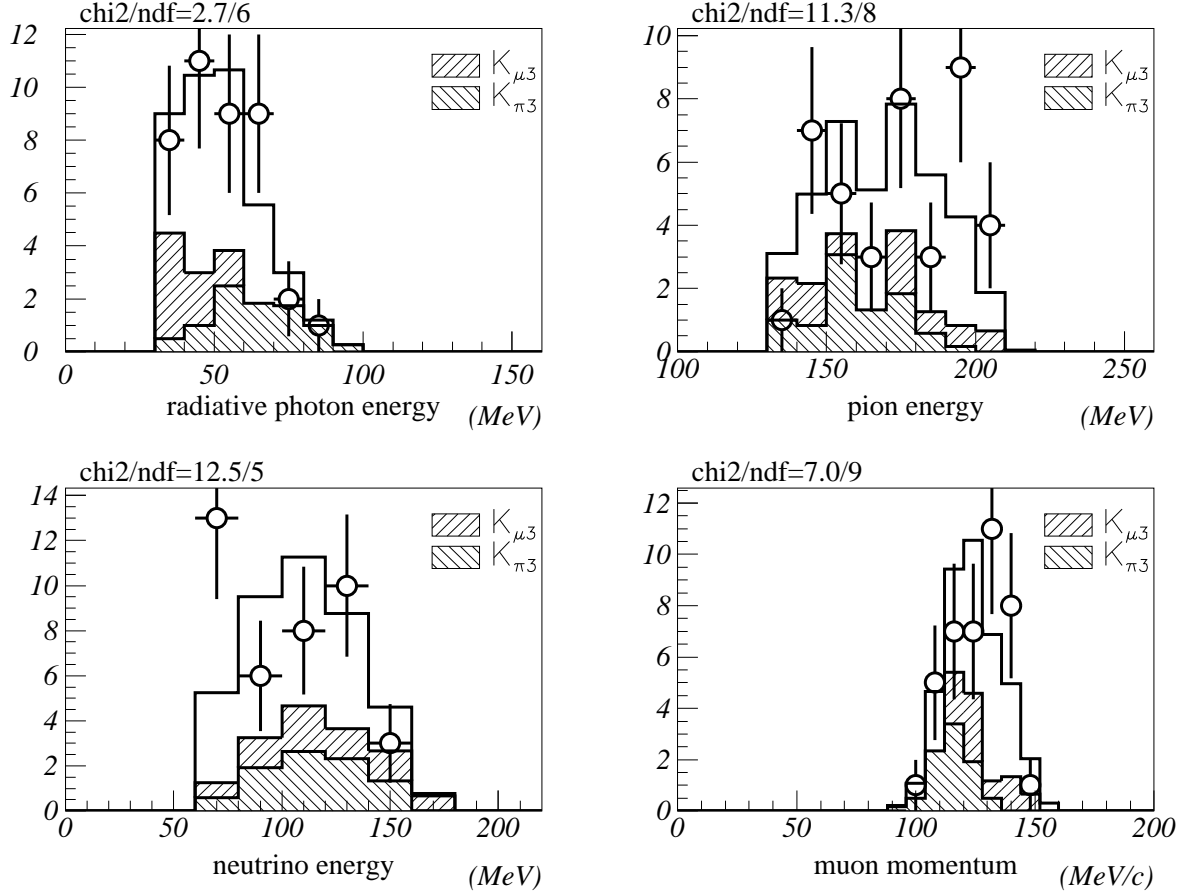


Figure 7.4: Spectra of the $K_{\mu 3\gamma}$ candidates: E_γ (top left), π^0 energy (top right), E_ν (bottom left), and muon momentum (bottom right). In each plot, the circles with error bars represent the distributions of the 40 events observed in the signal region. The cuts $E_\gamma > 30$ MeV and $E_\nu > 60$ MeV have been imposed in the analysis. The unhatched histograms represents the distribution of the Monte Carlo $K_{\mu 3\gamma}$ events with the central value of the measured branching ratio plus all the background distributions, and should be compared to the circles with error bars.

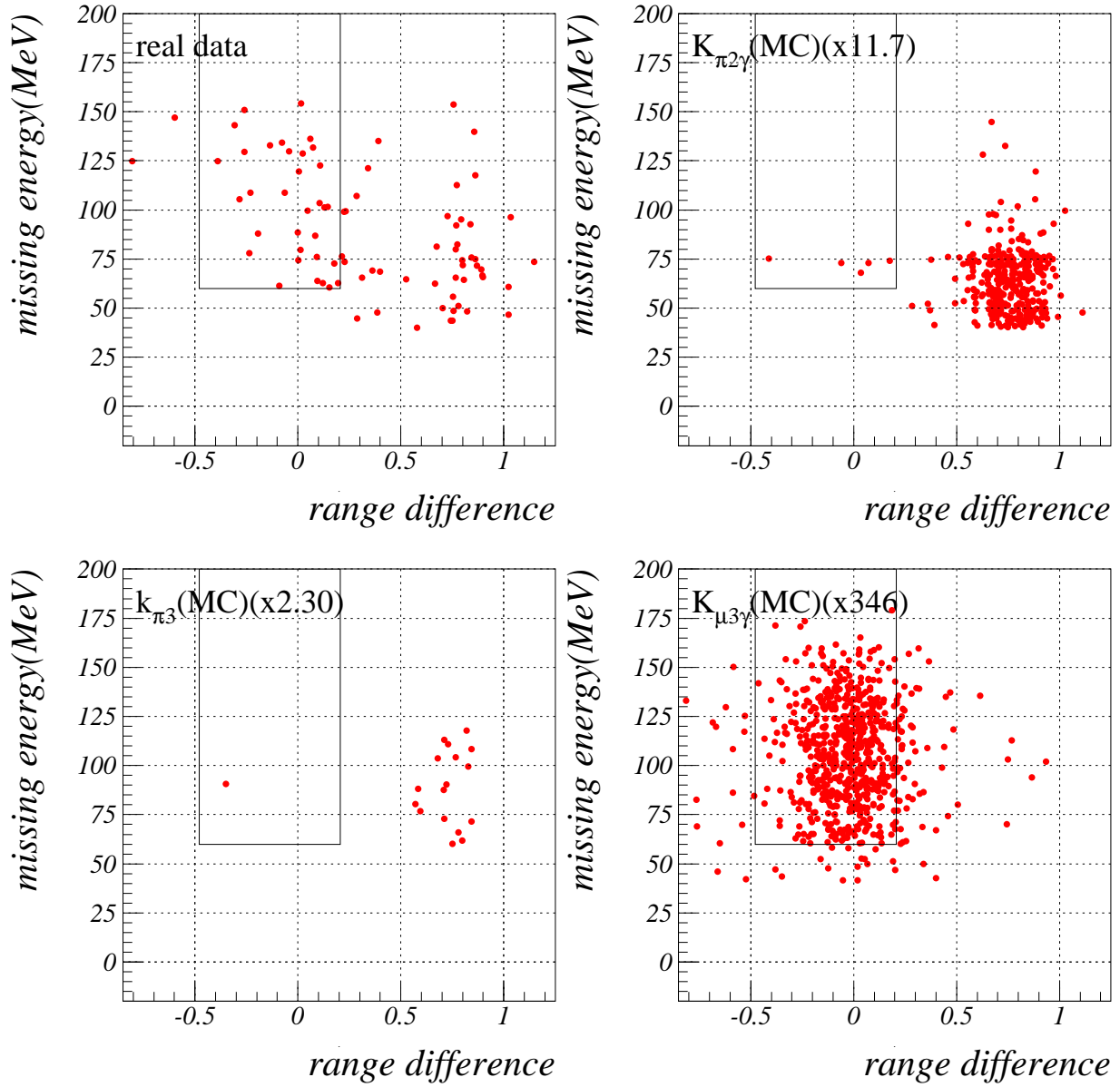


Figure 7.5: Missing energy (E_ν) vs range difference (dr_ratio) plots of the events with all analysis cuts imposed in real data (top left), and in the samples generated by Monte Carlo $K_{\pi 2\gamma}$ (top right), $K_{\pi 3}$ (bottom left), and $K_{\mu 3\gamma}$ (bottom right) simulation. Note that the Monte Carlo simulation is not scaled to real data.

Chapter 8

Systematic uncertainties

The systematic uncertainties in the single events sensitivity (SES) were due to imperfection of the BV calibrations, to which the photon selection was sensitive, as well as the difference between real data and Monte Carlo simulation, i.e. reproducibility of real data, smearing effects, etc. F_s was obtained from the $K_{\pi 2\gamma}$ branching ratio measurement, and was inversely proportional to the acceptance for $K_{\pi 2\gamma}$; $Br(K_{\mu 3\gamma})$ should therefore be proportional to the ratio of the $K_{\pi 2\gamma}$ acceptance to the $K_{\mu 3\gamma}$ acceptance in the 3γ trigger sample. Thus, the variations observed in the acceptance ratio were studied as each corresponding parameter was varied over the range that had not been excluded in the calibrations, as discussed in the subsections of this chapter.

8.1 visible fraction of the BV

The uncertainty in the visible fraction for the photon energy measurement in the BV was due to the calibration method by fitting the peak of the energy sum of the two photons from π^0 in the $K_{\pi 2}$ decay. The uncertainty of $\pm 1\%$ was evaluated from the fitted histograms (Fig. 8.1). The effects due to visible fraction ($\pm 2.7\%$) were studied by the changes of the double ratio of the acceptance

factors: $\frac{A_{K_{\pi 2\gamma}}^{changed}}{A_{K_{\mu 3\gamma}}^{changed}} / \frac{A_{K_{\pi 2\gamma}}^{standard}}{A_{K_{\mu 3\gamma}}^{standard}}$, and were summarized in Table 8.1.

	standard	+1.0	-1.0
$K_{\mu 3\gamma}$	8157	8114	8104
$K_{\pi 2\gamma}$	279785	272929	285518
ratio	-	1.0197	0.97352

Table 8.1: Systematic uncertainty related to the visible fraction in the BV: the numbers in the $K_{\mu 3\gamma}$ and $K_{\pi 2\gamma}$ rows mean the numbers of events which survived all the offline cuts, and the number in the “ratio” row mean the changes of the double ratio of the acceptance factors.

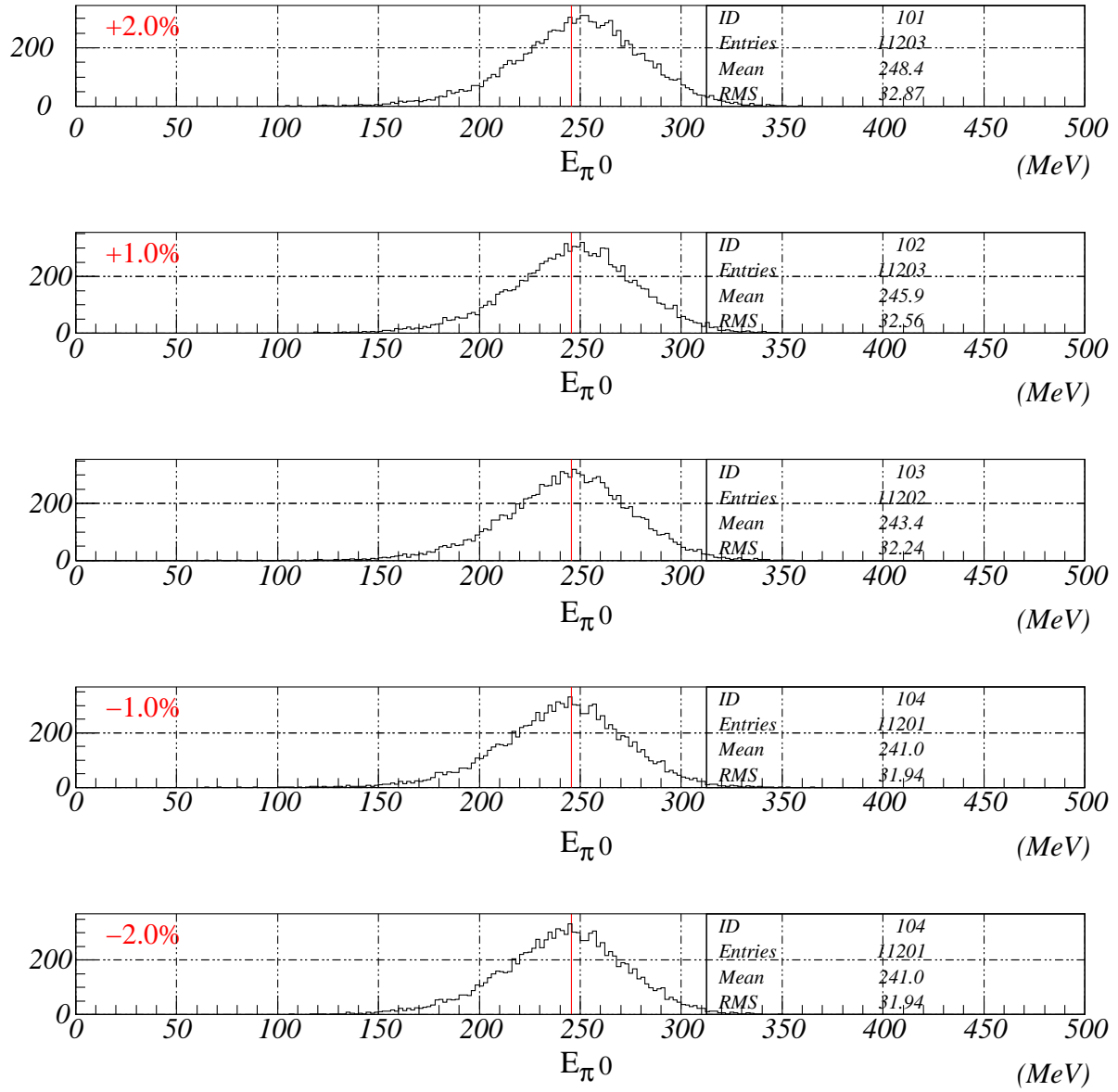


Figure 8.1: Variation in the visible fraction: distributions of the energy sum of the two photons from π^0 in K_{π^2} by changing the visible fraction from -2.0% to +2.0% by a 1.0% step.

8.2 BV z-measurement

The speed-of-light (17.44 cm/nsec) in the plastic scintillators of the BV counters was used in the analysis. Concerning the possible uncertainty, the value (17.1 cm/nsec) used in the the E787 analysis for the $K^+ \rightarrow \mu^+ \nu_\mu \gamma$ decay was tested. If the speed-of-light was changed, the values of the attenuation length were also moved due to the calibration process. Both parameters were varied and the double ratio of the acceptance factors was checked. The effects due to the z-measurement parameters ($\pm 1\%$) were summarized in Table 8.2.

	17.4 cm/nsec	17.1 cm/nsec
$K_{\mu 3\gamma}$	8157	8012
$K_{\pi 2\gamma}$	279785	277569
ratio	-	0.99005

Table 8.2: Systematic uncertainty related to the z measurement in the BV: the numbers in the $K_{\mu 3\gamma}$ and $K_{\pi 2\gamma}$ rows mean the numbers of event which survived all the offline cuts, and the number in “ratio” row means the double ratio of the acceptance factors.

8.3 BV Z-offset smearing

Judging from the distribution of the z-position accuracy in the BV (Fig. 8.2), the uncertainty in the z-offset smearing was estimated to be in between -10% and +15%. The parameter was varied between -10% and +15% and the the double ratio of the acceptance factors were checked. The effects due to the z-offset smearing ($\pm 1.7\%$) were summarized in Table 8.3.

	standard	+15%	-10%
$K_{\mu 3\gamma}$	8157	8185	8122
$K_{\pi 2\gamma}$	279785	276053	280901
ratio	-	1.0170	0.99173

Table 8.3: Systematic uncertainty related to the z-offset smearing in the Z measurement in the BV: the numbers in the $K_{\mu 3\gamma}$ and $K_{\pi 2\gamma}$ rows mean the number of events which survived all the offline cuts, and the number in the “ratio” row means the double ratio of the acceptance factors.

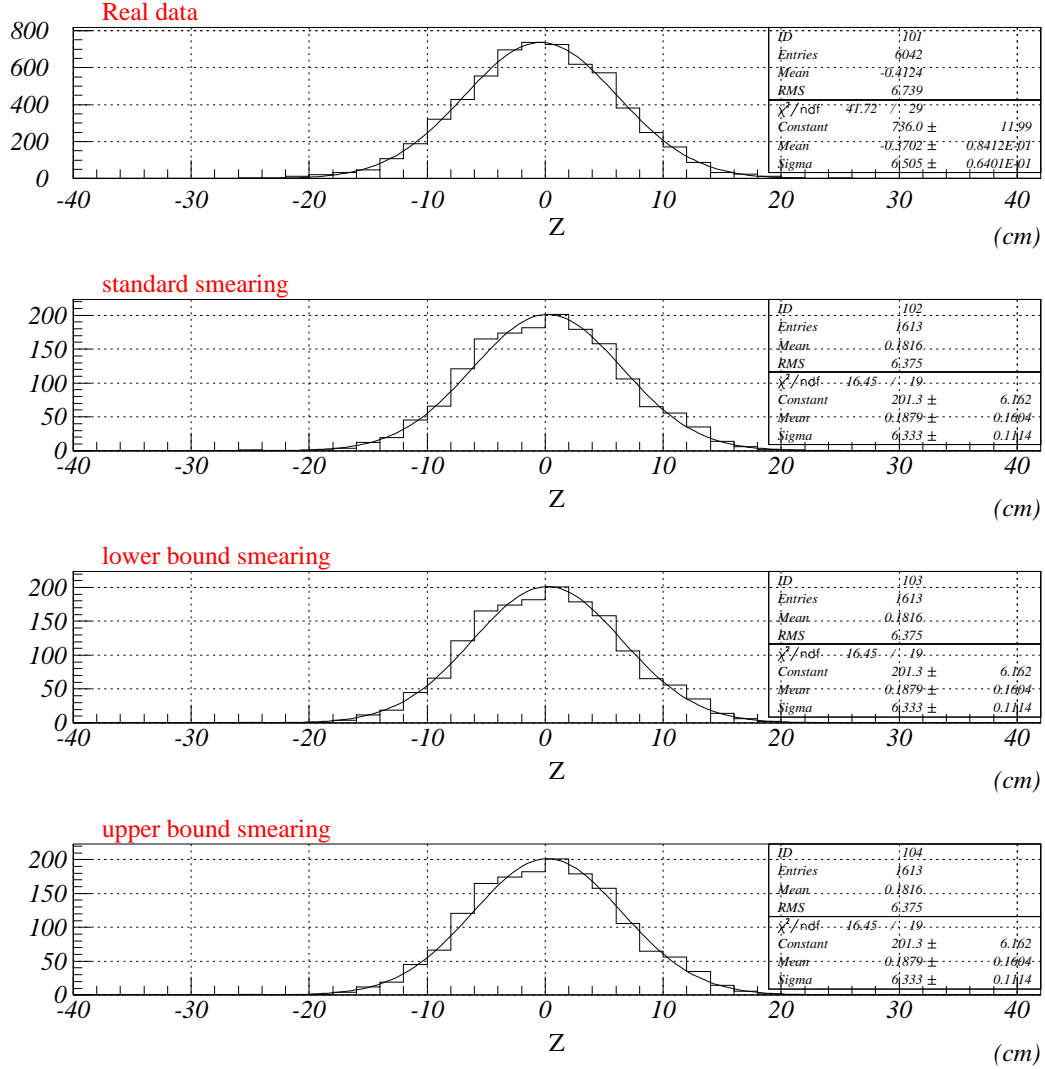


Figure 8.2: Variation in the z-offset smearing: distributions of the z-position accuracy. The “Sigma” obtained from the Gaussian fit was monitored by changing the smearing parameter.

8.4 BV energy smearing

The smearing parameter $P_{smearing}$ of the BV energy in the Monte Carlo was changed, and the double ratio of the acceptance factors was checked. The variation of $P_{smearing}$ was determined to be from 0.46 to 0.69, judging from the χ^2 probability distribution of the $K_{\pi 2\gamma}$ kinematic fit (see Fig. 3.10 in p.35). The effects due to the BV energy smearing ($\pm 1.5\%$) were summarized in Table 8.4.

	standard(0.55)	(0.69)	(0.46)
$K_{\mu 3\gamma}$	8157	7668	8461
$K_{\pi 2\gamma}$	279785	265559	286022
ratio	-	0.99040	1.0146

Table 8.4: Systematic uncertainty related to the photon energy smearing parameter of the BV: the numbers in the $K_{\mu 3\gamma}$ and $K_{\pi 2\gamma}$ rows mean the number of events which survived all the offline cuts, and the number in the “ratio” row means the double ratio of the acceptance factors.

8.5 charged track smearing

The smearing parameters of the charged track in the Monte Carlo in the kinematic fit were varied within $\pm 10\%$ and the double ratio of the acceptance factors was checked. The effects due to the charged track smearing ($\pm 2.8\%$) were summarized in Table 8.5.

	standard	Psmear1	Psmear2	Esmear1	Esmear2
$K_{\mu 3\gamma}$	8157	8176	8163	8129	8156
$K_{\pi 2\gamma}$	279785	288518	281180	286979	278320
ratio	-	0.97198	0.99575	0.97157	1.0051

Table 8.5: Systematic uncertainty related to the charged track smearing parameter: the numbers in the $K_{\mu 3\gamma}$ and $K_{\pi 2\gamma}$ row mean the numbers of event which survived all the offline cuts, and the number in the the “ratio” row mean the double ratio of the acceptance factors. “Psmear1” and “Psmear2” mean the shifts on the momentum smearing parameter by $\pm 10\%$, and “Esmear1” and “Esmear2” means the shifts on the kinetic energy smearing parameter by $\pm 10\%$, respectively.

8.6 dE/dx cut in the Range Stack

Since the Monte Carlo simulation did not reproduce the energy resolution of the RS counters perfectly, the edf distribution of Monte Carlo was different from that of real data. The cut position of the dE/dx cut in Monte Carlo was determined by comparing the edf distributions between $K_{\mu 3}$ from real data and the $K_{\mu 3}$ decays in Monte Carlo. To the systematic uncertainty, the cut position for the Monte Carlo analysis was varied within $\pm 5\%$ (see Fig. 8.3), and changes in the double ratio of the acceptance factors are checked (Table 8.6). The effects due to the cut position of the dE/dx cut ($< 1\%$) was negligible.

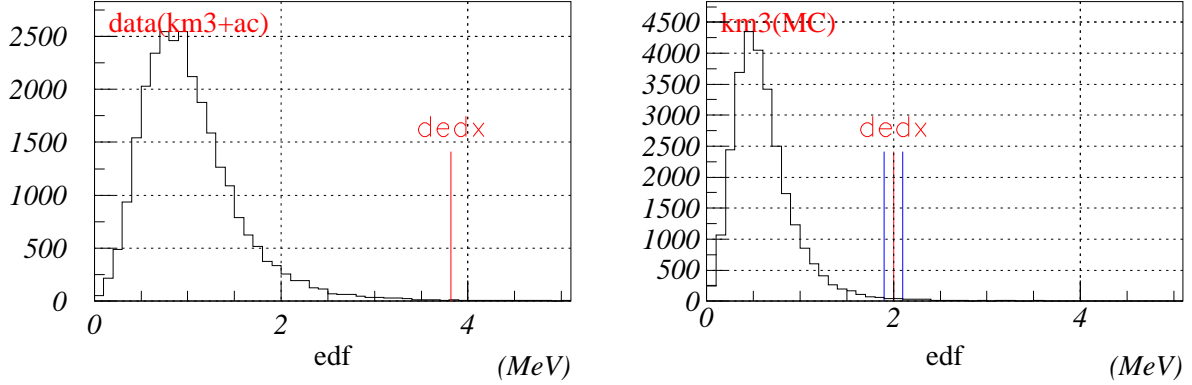


Figure 8.3: edf distributions used in the dE/dx cut: $K_{\mu 3}$ from the real data (left) and Monte Carlo $K_{\mu 3}$ decays (right).

	standard	+5.0%	-5.0%
$K_{\mu 3\gamma}$	8157	8160	8114
ratio	-	1.0004	0.99473

Table 8.6: Systematic uncertainty related to the dE/dx cut: the numbers in the $K_{\mu 3\gamma}$ row means the numbers of event which survived all the offline cuts, and the numbers in the “ratio” row mean the double ratio of the acceptance factors.

8.7 range-momentum relation cut

The cut position on the range-momentum relation cut for the Monte Carlo was determined by the comparison between the real data and the Monte Carlo data for the dr_ratio distribution used in the cut. The uncertainty due to the fitting error was taken as the source of systematic uncertainty (Table 8.7). The cut positions for the MC analysis were varied, and change in the double ratio of the acceptance factors was checked (Table 8.8). The effect due to the cut position of the cuts ($< 1\%$) was negligible.

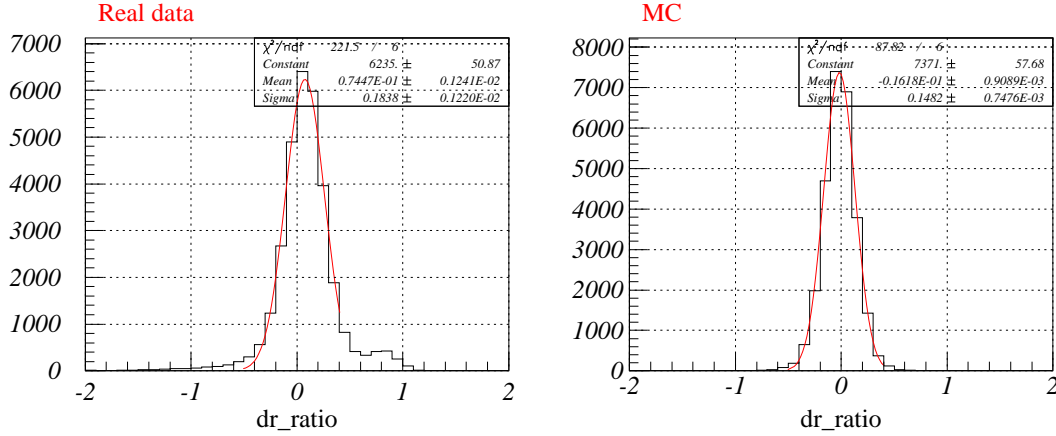


Figure 8.4: dr_ratio distribution for the muon tracks in real data (left); dr_ratio distribution of muon track in Monte Carlo Data (right).

-	lower end	upper end
standard	-0.47938	0.20599
sys1	-0.47613	0.20802
sys2	-0.48262	0.20396

Table 8.7: Systematic uncertainty related to the cut position of the muon band.

	standard	sys1	sys2
$K_{\mu 3\gamma}$	8157	8169	8146
ratio	-	1.0015	0.99865

Table 8.8: Systematic uncertainty related to the range-momentum relation cut: the numbers in the $K_{\mu 3\gamma}$ row mean the numbers of event which survived all the offline cuts, and the numbers in the “ratio” row mean the double ratio of the acceptance ratio.

8.8 e^+ bremsstrahlung cut

The variable *amings* was used in the e^+ bremsstrahlung cut. The fitting error in the comparison of the distributions of the real data and Monte Carlo was taken as the source of systematic uncertainty. The possible change for the MC cut position lies between 0.921 and 0.928, while the standard cut position was 0.925 as shown in Fig. 8.5. The effects due to the cut position of the e^+ bremsstrahlung cut ($\pm 1\%$) were summarized in Table 8.9.

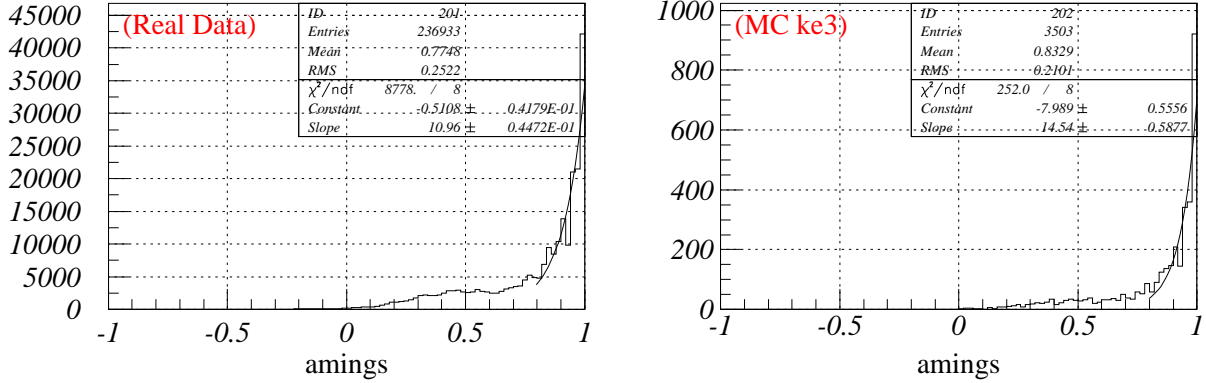


Figure 8.5: *amings* distributions of the electron events in real data (left) and in the Monte Carlo K_{e3} events (right).

	standard(0.925)	0.921	0.928
$K_{\mu 3\gamma}$	8157	8232	8070
ratio	-	1.0092	0.98933

Table 8.9: Systematic uncertainty related to *amings* cut: the numbers in the $K_{\mu 3\gamma}$ row mean the numbers of events which survived all the offline cuts. The numbers in the “ratio” row mean the double ratio of the acceptance factors.

8.9 photon timing cut

The cut position of the photon timing cut for the Monte Carlo data was determined from the comparison of photon timing distributions for the real and Monte Carlo for the lower energy photon in the $K_{\pi 2}$ decay. The error for the Gaussian fitting used in the comparison was taken as the source of the systematic uncertainty. The change in the double ratio of the acceptance factors was checked for the case of minimum(sys1) and maximum(sys2) interval for the photon timing cut position.

-	lower end	upper end
standard	-1.3587nsec	0.6850nsec
sys2	-1.3680nsec	0.6940nsec
sys1	-1.3480nsec	0.6760nsec

Table 8.10: photon timing cut position:

	standard	sys1	sys2
$K_{\mu 3\gamma}$	8157	8180	8126
$K_{\pi 2\gamma}$	279785	280640	278986
ratio	-	0.99976	0.99904

Table 8.11: Systematic uncertainty related to the photon timing : the numbers in the $K_{\mu 3\gamma}$ an $K_{\pi 2\gamma}$ rows mean the numbers of events which survived all the offline cuts. The numbers in the “ratio” row mean the double ratio of the acceptance factors.

8.10 summary

All the systematic uncertainties in the previous sections are summarized in Table 8.12. The statistical uncertainty of the Monte Carlo simulation in estimating the acceptance (1.1%) was also included. By adding them in quadrature, the total systematic uncertainty was estimated to be 4.9%.

sources	estimated systematic uncertainty (%).
BV visible fraction	2.7
BV z measurement	1.0
BV energy smearing	1.5
BV z-offset smearing	1.7
charged track smearing	2.8
dedx cut	0.1
e^+ bremsstrahlung cut	1.1
gamma timing	0.1
Monte Carlo statistics	1.1
total	4.9

Table 8.12: Summary of systematic uncertainties in the sensitivities.

This leads to

$$Br(K_{\mu 3\gamma}, E_\gamma > 20\text{MeV}) = (2.51 \pm 0.74(stat.) \pm 0.12(syst.)) \times 10^{-5},$$

$$Br(K_{\mu 3\gamma}, E_\gamma > 30\text{MeV}, \theta_{\mu\gamma} > 20^\circ) = (1.58 \pm 0.46(stat.) \pm 0.08(syst.)) \times 10^{-5}, \text{ and}$$

$$Br(K_{\mu 3\gamma}, 30 < E_\gamma < 60\text{MeV}) = (1.10 \pm 0.32(stat.) \pm 0.05(syst.)) \times 10^{-5}.$$

Chapter 9

Discussions

The experimental study of the $K_{\mu 3\gamma}$ decay in this thesis is a measurement of the branching ratio. The extraction of the structure-dependent component and a search for T-violation in $K_{\mu 3\gamma}$ were unable to be made because the number of $K_{\mu 3\gamma}$ events were not statistically enough; these studies will be pursued in future experiments. The differences among the predictions of chiral perturbation theory: $O(p^2)$, $O(p^4)$ without loop, and full $O(p^4)$ are at a level of 5 % (see Table 1.1(p.4)). More than 400 events would be necessary to determine whether higher order corrections are indispensable in the chiral perturbation calculation. In detecting a T-violating asymmetry of the order 10^{-4} , more than 10^8 events would be necessary.

For improvements in the future measurement with this experimental method, the following issues were figured out during the data analysis of this study.

- At first, the trigger conditions should be well designed, because it was turned out that about a half of the events accumulated in the trigger were from the $K_{\pi 2}$ decay whose π^+ had interactions in the Range Stack. A crude online momentum-measurement with UTC would help to reduce the trigger rate and thereby increase the available K^+ decays at rest. Another possible improvement about trigger is regarding the veto conditions within the trigger: $(9 + \dots + 21)$ and HEX from the RS and \overline{EC} from the endcap calorimeters. As shown in Table 6.2 (p.67), these trigger conditions reduced the photon trigger acceptance to be 5 % because an event was removed if the electromagnetic shower of one of three photons in the final state of $K_{\mu 3\gamma}$ started before reaching the BV. Requesting all of the three photons were detected in the BV reduced the acceptance further, which resulted in a very small photon-trigger acceptance in total (6.09×10^{-3}). The endcap calorimeters and the RS counters in the outer layers (e.g. layers from 10 to 21) would work as a part of photon detection, although the photon reconstruction would be more complicated and there would be a concern about high counting rates (and thereby accidental hits) in particular in the upstream endcap calorimeter.
- Secondly, a better resolution of photon energy measurement should be pursued in the BV, which was originally designed in E787 for the purpose of vetoing a photon from $K_{\pi 2}$ background in the $K^+ \rightarrow \pi^+ \nu \bar{\nu}$ study rather than measuring the energy and position of a photon as a calorimeter. The study of the $K_{\mu 3\gamma}$ decay would be made even without a complicated kinematic fit and calibration procedures of the parameters for it, and the proportion of the correct pairing of π^0 would also be improved.
- Thirdly, the control samples to study and monitor the accidental loss should be carefully designed and accumulated simultaneously with the physics trigger. The E787 experiment in

1998 was unable to run with such triggers, mainly due to a lack of flexibility in the Level-0 trigger system. Proper monitor-triggers, such as a prescaled trigger without conditions on the photons, would make the analysis simpler and more reliable.

Chapter 10

Conclusion

A new measurement of the $K^+ \rightarrow \pi^0 \mu^+ \nu_\mu \gamma$ branching ratio was performed in this thesis by using the E787 apparatus of the AGS of BNL. Forty candidate events were observed in the signal region with the expected background of (16.5 ± 2.7) events. The results of the measurement were:

$$\begin{aligned} Br(K_{\mu 3\gamma}, E_\gamma > 30\text{MeV}, \theta_{\mu\gamma} > 20^\circ) &= (1.58 \pm 0.46(\text{stat.}) \pm 0.08(\text{syst.})) \times 10^{-5}, \text{ and} \\ Br(K_{\mu 3\gamma}, 30 < E_\gamma < 60\text{MeV}) &= (1.10 \pm 0.32(\text{stat.}) \pm 0.08(\text{syst.})) \times 10^{-5}. \end{aligned}$$

The $Br(K_{\mu 3\gamma}, E_\gamma > 30 \text{ MeV}, \theta_{\mu\gamma} > 20^\circ)$ was consistent with the theoretical prediction 2.0×10^{-5} as well as the previous measurement $(2.4 \pm 0.5(\text{stat.}) \pm 0.6(\text{syst.})) \times 10^{-5}$ by the E470 experiment at KEK. The $Br(K_{\mu 3\gamma}, 30 < E_\gamma < 60 \text{ MeV})$ was consistent with the previous measurement $(1.5 \pm 0.4) \times 10^{-5}$ by the ISTR+ experiment. The results in this thesis provide better precision than the previous results.

Appendix A

Chiral Perturbation Theory

The theoretical techniques using chiral symmetry to the strong interactions of mesons were developed in the late 1960s and 1970s and were called Chiral Lagrangian or Chiral Dynamics. Weinberg, in 1979 [1], introduced the concepts of Effective Field Theory using an effective Lagrangian and proposed the application to strong interactions. In 1984 and 1985 Gasser and Leutwyler materialized the program by Weinberg and discussed Chiral Lagrangian by expanding it to the higher order ($O(p^4)$) [2, 3]; their approach is called Chiral Perturbation Theory (ChPT) and has been intensively studied in particle and nuclear physics as a theory of low energy QCD. There are some textbooks treating ChPT [4]. Many applications to the phenomenology of particle physics are collected in the DAΦNE Physics Handbook [5]. Radiative kaon decays in ChPT were discussed in [6, 7]; the matrix elements for the decays at $O(p^4)$ in ChPT were evaluated and the decay rates were calculated in [14, 15].

The chiral symmetry of quark-gluon interactions, i.e. invariance under separate global rotations among left- and right-handed up, down, and strange quarks called $SU(3)_L \times SU(3)_R$, is spontaneously broken in the QCD vacuum and is also explicitly broken by the existence of a non-zero quark. However, such effects can be included perturbatively and it is possible to construct an effective Lagrangian which describes the low energy interactions of Nambu-Goldstone bosons. The Lagrangian is given in an expansion in powers of derivatives (∂) to the boson fields, i.e. their external momenta (p), and/or quark masses; the interactions vanish in the limit $p \rightarrow 0$. Predictions are given in the relations between empirical observables, and large violation of ChPT predictions would be difficult to understand within the framework of QCD.

The Lagrangian based on chiral symmetry can be constructed with the nonlinear representation of the eight pseudoscalar fields in the form of a unitary 3×3 matrix, $U \equiv \exp(i\sqrt{2}\Phi/F_\pi)$ in which

$$\Phi = \begin{bmatrix} \frac{\pi^0}{\sqrt{2}} + \frac{\eta}{\sqrt{6}} & \pi^+ & K^+ \\ \pi^- & -\frac{\pi^0}{\sqrt{2}} + \frac{\eta}{\sqrt{6}} & K^0 \\ K^- & \bar{K}^0 & -\frac{2\eta}{\sqrt{6}} \end{bmatrix},$$

and the trace of the matrix terms using U . The simplest Chiral Lagrangian $\mathcal{L}^{(2)}$ with scalar (s), pseudo-scalar (p), vector (v_μ), and axial-vector (a_μ) external fields is

$$\mathcal{L}^{(2)} = \frac{1}{4} F_\pi^2 \cdot \text{Tr}[(D_\mu U)(D^\mu U^\dagger) + \chi^\dagger U + \chi U^\dagger]$$

where

$$\begin{aligned} D_\mu U &\equiv \partial_\mu U - i r_\mu U + i U l_\mu \\ \chi &= 2B_0(s + ip) \end{aligned}$$

with

$$\begin{aligned} r_\mu &\equiv v_\mu + a_\mu \\ l_\mu &\equiv v_\mu - a_\mu \end{aligned}$$

The quark mass matrix

$$\mathcal{M} \equiv \begin{bmatrix} m_u & 0 & 0 \\ 0 & m_d & 0 \\ 0 & 0 & m_s \end{bmatrix}$$

is contained in the scalar field s . The pion decay constant $F_\pi = 94$ MeV is the only coupling constant to the interactions in $\mathcal{L}^{(2)}$. B_0 is the constant related to the quark condensate. For the study of radiative semileptonic K^+ decay, we can use the following expressions:

$$\begin{aligned} s + ip &= \mathcal{M}, \\ r_\mu &= -e Q A_\mu, \\ l_\mu &= -e Q A_\mu - \frac{e}{\sqrt{2} \sin \theta_W} (W_\mu^+ T_+ + h.c.), \end{aligned}$$

where A_μ and W_μ are the photon and W bosons, and

$$\begin{aligned} T_+ &\equiv \begin{bmatrix} 0 & V_{ud} & V_{us} \\ 0 & 0 & 0 \\ 0 & 0 & 0 \end{bmatrix}, \\ Q &\equiv \begin{bmatrix} 2/3 & 0 & 0 \\ 0 & -1/3 & 0 \\ 0 & 0 & -1/3 \end{bmatrix}. \end{aligned}$$

The evaluation of $\mathcal{L}^{(2)}$ at the tree level of the meson fields yields the results to meson interactions derived by the lowest order Current Algebra and PCAC in 1960s. This is regarded as the leading order, at $O(p^2)$, in ChPT.

To go beyond the leading order, inclusion of the loop diagrams in $\mathcal{L}^{(2)}$ introduces divergences and does not work. Gasser and Leutwyler, in [2, 3], gave the most-general and chiral-invariant Lagrangian in the higher order, $\mathcal{L}^{(4)}$:

$$\begin{aligned} \mathcal{L}^{(4)} &= L_1 \cdot (Tr[D^\mu U^\dagger D_\mu U])^2 + L_2 \cdot Tr[D^\mu U^\dagger D^\nu U] Tr[D_\mu U^\dagger D_\nu U] + L_3 \cdot Tr[D^\mu U^\dagger D_\mu U D^\nu U^\dagger D_\nu U] \\ &+ L_4 \cdot Tr[D_\mu U D^\mu U^\dagger] Tr[\chi^\dagger U + \chi U^\dagger] + L_5 \cdot Tr[D^\mu U^\dagger D_\mu U (\chi^\dagger U + U^\dagger \chi)] \\ &+ L_6 \cdot (Tr[\chi^\dagger U + \chi U^\dagger])^2 + L_7 \cdot (Tr[\chi^\dagger U - \chi U^\dagger])^2 + L_8 \cdot Tr[\chi^\dagger U \chi^\dagger U + \chi U^\dagger \chi U^\dagger] \\ &- iL_9 \cdot Tr[R_{\mu\nu} D^\mu U D^\nu U^\dagger + L_{\mu\nu} D^\mu U^\dagger D^\nu U] + L_{10} \cdot Tr[U^\dagger R_{\mu\nu} U L^{\mu\nu}] \\ &+ L_{11} \cdot Tr[R_{\mu\nu} R^{\mu\nu} + L_{\mu\nu} L^{\mu\nu}] + L_{12} \cdot Tr[\chi^\dagger \chi], \end{aligned}$$

where $R^{\mu\nu}$ and $L^{\mu\nu}$ are the field strength tensors corresponding to the external fields r_μ and l_μ

$$\begin{aligned} R^{\mu\nu} &\equiv \partial^\mu r^\nu - \partial^\nu r^\mu - i [r^\mu, r^\nu], \\ L^{\mu\nu} &\equiv \partial^\mu l^\nu - \partial^\nu l^\mu - i [l^\mu, l^\nu] \end{aligned}$$

and with 10 phenomenological coupling constants L_1, \dots, L_{10} (and two more constants L_{11} and L_{12} , which are not directly accessible to experiments and needed as counterterms in the renormalization of the one-loop graphs). They obtained empirical values of L_1, \dots, L_{10} from the known experimental results of pion scatterings as well as pion and kaon decays. The Lagrangian \mathcal{L}_{anom} , which arises from the chiral anomaly and can be determined without extra coupling constant, should also be included. Finally, $\mathcal{L}^{(4)}$ can be used at the tree level together with \mathcal{L}_{anom} and with $\mathcal{L}^{(2)}$ at the tree and one-loop levels in order to study the low-energy meson interactions consistent with QCD. The evaluation with this scheme is the next-to-leading order, at $O(p^4)$, in ChPT.

Appendix B

The $K_{\mu 3\gamma}$ amplitude at $O(p^4)$ in ChPT

The tensors $V_{\mu\nu}^+$, $A_{\mu\nu}^+$ and F_ν^+ used in the matrix element for $K^+(p) \rightarrow \pi^0(p')l^+(p_l)\nu_l(p_{nu})\gamma(q)$, when the photon is on-shell ($q^2 = 0$), are decomposed as:

$$\begin{aligned} V_{\mu\nu}^+ &= \hat{V}_{\mu\nu}^+ + \frac{p_\mu}{pq} F_\nu^+, \\ \hat{V}_{\mu\nu}^+ &= V_1 \left(g_{\mu\nu} - \frac{W_\mu q_\nu}{qW} \right) + V_2 \left(p'_\mu q_\nu - \frac{p'q}{qW} W_\mu q_\nu \right) + V_3 \left(p'_\mu W_\nu - \frac{p'q}{qW} W_\mu W_\nu \right) + V_4 \left(p'_\mu p'_\nu - \frac{p'q}{qW} W_\mu p'_\nu \right), \\ A_{\mu\nu}^+ &= i\epsilon_{\mu\nu\rho\sigma} (A_1 p'^\rho q^\sigma + A_2 q^\rho W^\sigma) + i\epsilon_{\mu\lambda\rho\sigma} p'^\lambda q^\rho W^\sigma (A_3 W_\nu + A_4 p'_\nu), \\ F_\nu^+ &= C_1 p'_\nu + C_2 (p - p')_\nu, \end{aligned}$$

where $W \equiv (p_l + p_{nu})$ is equal to $(p - p' - q)$.

B.1 Preliminaries

Three functions $f_1(t)$, $f_2(t)$, and $f_3(t)$ are defined as:

$$\begin{aligned} f_1(t) &= \sqrt{2} + \frac{4\overline{L}_9}{\sqrt{2}F^2}t + 2 \sum_{I=1}^3 (c_2^I - c_1^I) B_2^I(t), \\ f_2(t) &= -\frac{4\overline{L}_9}{\sqrt{2}F^2} + \frac{1}{t} \sum_{I=1}^3 \left\{ (c_1^I - c_2^I) \left[2B_2^I(t) - \frac{(t + \Delta_I)\Delta_I J_I(t)}{2t} \right] - c_2^I \Delta_I J_I(t) \right\}, \\ f_3(t) &= \frac{F_K}{\sqrt{2}F_\pi} + \frac{1}{2t} \sum_{I=1}^3 \left\{ (c_1^I + c_2^I)(t + \Delta_I) - 2c_3^I \right\} \Delta_I J_I(t), \end{aligned}$$

where

$$\begin{aligned} \overline{L}_9 &= L_9^r(\mu) - \frac{1}{256\pi^2} \ln \frac{M_\pi M_K^2 M_\eta}{\mu^4}, \\ \Delta_I &= M_I^2 - m_l^2, \\ t &= (p - p')^2. \end{aligned}$$

\overline{L}_9 is a scale-independent coupling constant ($L_i^r(\mu)$ is the renormalized coefficients and μ is the scale introduced by dimensional regularization). The value of M_η is obtained from the Gell-Mann-Okubo mass relation: $3M_\eta^2 = 4M_K^2 - M_\pi^2$. The sum over I corresponds to the three loop diagrams in Fig. 1.2. The coefficients, c_i^I , are summarized in Table B.1.

I	M_I	m_I	c_1^I	c_2^I	c_3^I
1	M_K	M_π	1	-2	$-M_K^2 - 2M_\pi^2$
2	M_K	M_η	3	-6	$-M_K^2 - 2M_\pi^2$
3	M_π	M_η	0	-6	$-6M_\pi^2$

Table B.1: Coefficients for loop integrals; all c_i^I must be divided by $6\sqrt{2}F^2$.

The integral $\bar{J}(t)$ is defined with the loop integral $J(t)$ as $\bar{J}(t) \equiv J(t) - J(0)$ with $M = M_I$, $m = m_I$, and $t = k^2$. This leads to the following expression.

$$\bar{J}(t) = \frac{1}{32\pi^2} \left(2 + \frac{\Delta}{t} \log \frac{m^2}{M^2} - \frac{\Sigma}{\Delta} \log \frac{m^2}{M^2} - \frac{\sqrt{\lambda}}{t} \log \frac{(t + \sqrt{\lambda})^2 - \Delta^2}{(t - \sqrt{\lambda})^2 - \Delta^2} \right)$$

where

$$\begin{aligned} \Delta &= M^2 - m^2, \\ \Sigma &= M^2 + m^2, \\ \lambda(t, M^2, m^2) &= (t + \Delta)^2 - 4tM^2. \end{aligned}$$

These are used with subscripts as follows.

$$J_I(t) \equiv \bar{J}(t) \text{ with } M = M_I, m = m_I$$

The function $B_2^I(t)$ are defined as $B_2(t, M^2, m^2)$ with $M = M_I$, $m = m_I$ where

$$\begin{aligned} B_2(t, M^2, m^2) &= \frac{1}{288\pi^2} (3\Sigma - t) - \frac{\lambda(t, M^2, m^2)\bar{J}(t)}{12t} + \frac{t\Sigma - 8M^2m^2}{384\pi^2\Delta} \log \frac{M^2}{m^2}, \\ \Delta &= M^2 - m^2, \\ \Sigma &= M^2 + m^2, \\ \lambda(t, M^2, m^2) &= (t + \Delta)^2 - 4tM^2. \end{aligned}$$

M_I and m_I are also given in Table B.1. The decay constants F_π, F_K are empirical and the values are: $F_\pi = 93.2$ MeV and $F_K = 113.6$ MeV.

B.2 $V_{\mu\nu}^+$

The amplitudes for $V_{\mu\nu}^+$ are:

$$\begin{aligned} V_1 &= I_1 + p' W_q f_2(W_q^2) + f_3(W_q^2), \\ V_2 &= I_2 - \frac{1}{pq} \left[p' W_q f_2(W_q^2) + f_3(W_q^2) \right], \\ V_3 &= I_3 + \frac{1}{pq} \left[p' W f_2(W^2) + f_3(W^2) - p' W_q f_2(W_q^2) - f_3(W_q^2) \right], \\ V_4 &= \frac{f_1(W^2) - f_1(W_q^2)}{pq}, \\ W_q &= W + q = p - p'. \end{aligned}$$

I_1, I_2, I_3 are additional amplitudes given by

$$\begin{aligned}
I_1 &= \frac{4qW}{\sqrt{2}F^2}(\overline{L_9} + \overline{L_{10}}) + \frac{8p'q}{\sqrt{2}F^2}\overline{L_9} \\
&\quad + \sum_{I=1}^3 \left\{ \left[(W_q^2 + \Delta_I)(c_1^I + c_2^I) - 2(c_2^I p' W_q + c_3^I) \right] \left[\frac{(W_q^2 - \Delta_I)\hat{J}_I}{2W_q^2} - 2G_I \right] \right. \\
&\quad + \frac{c_2^I - c_1^I}{2} \left[\frac{p' W_q}{W_q^2} \left(\frac{W_q^4 - \Delta_I^2}{W_q^2} + 4\hat{B}_2^I \right) + p'(W - q)L_m^I \right] \\
&\quad \left. + \frac{2(c_2^I - c_1^I)}{qW} \left[p'q(F_I - (W_q^2 + \Delta_I)G_I) + p'W(\hat{B}_2^I - B_2^I) \right] \right\}, \\
I_2 &= -\frac{8\overline{L_9}}{\sqrt{2}F^2} + \frac{2}{qW} \sum_{I=1}^3 (c_2^I - c_1^I) [F_I - (W^2 + \Delta_I)G_I], \\
I_3 &= -\frac{4\overline{L_9}}{\sqrt{2}F^2} + \sum_{I=1}^3 \left\{ 2(c_2^I - c_1^I) \left[G_I + \frac{L_m^I}{4} + \frac{\hat{B}_2^I - B_2^I}{qW} \right] - c_1^I \frac{\Delta_I J_I}{W^2} \right\},
\end{aligned}$$

where

$$\begin{aligned}
\overline{L_{10}} &= L_{10}'(\mu) + \frac{1}{256\pi^2} \ln \frac{M_\pi M_K^2 M_\eta}{\mu^4}, \\
L_m^I &= \frac{\Sigma_I}{32\pi^2 \Delta_I} \ln \frac{m_I^2}{M_I^2}, \\
F_I &= \hat{B}_2^I - \frac{W^2}{4} L_m^I + \frac{1}{qW} (W^2 B_2^I - W_q^2 \hat{B}_2^I), \\
G_I &= \frac{M_I^2}{2} C(W_q^2, W^2, M_I^2, m_I^2) + \frac{1}{8qW} \left[(W_q^2 + \Delta_I)\hat{J}_I - (W^2 + \Delta_I)J_I + \frac{1}{64\pi^2} \right], \\
J_I &\equiv J_I(W^2) \\
\hat{J}_I &\equiv J_I(W_q^2), \\
B_2^I &\equiv B_2^I(W^2), \\
\hat{B}_2^I &\equiv B_2^I(W_q^2).
\end{aligned}$$

The function C used in G_I as $C(W_q^2, W^2, M_I^2, m_I^2)$ are:

$$C(t_1, t_2, M^2, m^2) = -i \int \frac{d^4 p}{(2\pi)^4} \frac{1}{(p^2 - M^2)[(p + q_1)^2 - M^2][(p + q_1 + q_2)^2 - m^2]},$$

where $t_1 = (q_1 + q_2)^2$, $t_2 = q_2^2$ and $q_1^2 = 0$.

B.3 $A_{\mu\nu}^+$

The chiral-anomaly contribution to $A_{\mu\nu}^+$ is given by

$$A_{\mu\nu} = \frac{i\sqrt{2}}{16\pi^2 F_\pi^2} \left\{ \epsilon_{\mu\nu\rho\sigma} q^\rho (4p' + W)^\sigma + \frac{4}{W^2 - M_K^2} \epsilon_{\mu\lambda\rho\sigma} W_\nu p'^\lambda q^\rho W^\sigma \right\}.$$

B.4 F_ν^+

The K_{l3} matrix element F_ν^+ is given by

$$F_\nu^+ = f_1(t)p'_\nu + \left[\frac{1}{2} (M_K^2 - M_\pi^2 - t) f_2(t) + f_3(t) \right] (p - p')_\nu .$$

where $t = (p - p')^2$.

Appendix C

Beam cuts

In this appendix, details of beam cuts in Section 4.1 are explained.

- “beam”
This is a package of the following cuts to remove the “double-beam” backgrounds events.
 - CKTRS
This cut required that, when another kaon was observed in the Čerenkov counters (CK) with more than four PMT hits, the timing should not coincide with the charged track time in the RS.
 - CPITRS
This cut required that, when an incoming pion was observed in the Čerenkov counters with more than four PMT hits, the timing should not coincide with the charged track time.
 - BWTRS
This cut required that, when another beam wire chamber hits were observed, the timing should not coincide with the charged track time.
 - BHTRS
This cut required that the timing of the hits in the beam hole counter should not coincide with the charged track time.
 - B4TRS
This cut required that the timing of the B4 hit closest to the kaon time in the target and the charged track time in the RS should be separated for at least 3nsec.
 - PBGLASS
This cut required that the number of hits in the lead glass counters should be less than 2. This reduced π^+ contamination in the beam as well as to detect extra photons to the beam direction.
- B4DEDX
This cut required that the energy deposit in the B4 counters should be larger than 1.5 MeV and be consistent with the kaon coming to rest. This reduced the π^+ in the beam to the target.
- KIC
This cut required that the I-counter neighboring the “kaon fibers” should not have a hit at the timing of B4.

- **TGGE0**
This cut removed the double-beam background events by using the timing information (TDC) and the wave-form information (TD) of the I-counters.
- **TIMCON**
This cut required the time consistency of the hits of the kaon coming to rest, recorded in the B4 and the target, as well as the time consistency of the hits of the outgoing charged track, recorded in the target and the RS.
- **TICCON**
This cut required the time consistency between the IC hits and the RS hits.
- **TGCCD**
This cut required the time consistency of each “kaon fiber” with the B4.
- **TGEDGE**
This cut required that the timing of each edge fiber should be consistent with the RS timing when the energy is large (>4 MeV).
- **B4EKZ**
This cut was on the kaon beam likelihood, which was formed by the B4 energy, the z position of the kaon decay vertex, and the total energy of K^+ in the target.
- **DELC**
This cut was a tight offline delayed coincidence, when the uncertainty in the measurement of T_K and T_π was large.

Appendix D

Target cuts

In this appendix, details of the target cuts in Section 4.1 are explained. In the E787 target analysis, the main interest was the $K^+ \rightarrow \pi^+ \nu \bar{\nu}$ decay and the target fibers hit by the charged particle from the K^+ decay at rest was conventionally classified as the “pion fiber”, regardless of the type of the charged track, while the fibers hit by the entering (and stopping) K^+ were classified as the “kaon fibers”. The other fibers in the extrapolated path of “pion” track were called the “opposite side pion” fibers, which could be due to a mistake in the determination of the kaon-decay vertex position in the X-Y plane. All the other fibers were called the “gamma fibers” because the electromagnetic shower in the target due to a photon from the K^+ decay was recorded as such, and were used for photon veto in the target (Section 4.3.3). The energy sums of the “pion” and “kaon” fibers were called as etg and ek , respectively. The estimated track length in the pion fibers was called rtg . The target cuts used in section 4.1 are the following cuts.

- EPITG
This cut required that the energy deposit in any “pion fiber” should be less than 5.0 MeV, because the charged particle should be a minimum ionizing particle (M.I.P.).
- TGER
This cut required that etg should be larger than 1.0 MeV when rtg is larger than 2.0 cm.
- TARGF
This cut required that the location of the “pion fiber” closest to the kaon decay vertex should be within 0.6 cm.
- RTDIF
This cut required that the uncertainty in the measurement of the “pion” path length should be less than 1.5 cm.
- TGZ
This cut required that the z position of K^+ decay vertex (tgz) should satisfy $-8.0 < tgz < 15.0$ cm.
- EKZ
This cut required that the tgz and the kaon energy (ek) should satisfy $|tgz - 0.22 \times ek + 16.4| \leq 10.0$ and be consistent with the kaon coming to rest.
- EPIMAXK
This cut required that the energy of the pion fibers near the vertex should be less than or equal to 3.0 MeV.

- **DRP**
This cut required that the width of the pion track should be small and a scattering of the charged track within the target should not happen.
- **PHIVTX**
This cut required that there should be no pion track to the opposite direction (back-to-back) of the kaon track.
- **EIC**
This cut required the consistency between the measured energy in the I-counters and the energy estimated from the length that the charged particle passed through in the I-counters.
- **TIC**
This cut required the consistency (± 5 nsec) of the timing of the I-counter hits with the charged track.
- **OPSVETO**
This cut required that the energy of the “other side pion” fibers should be less than 2.0 MeV.
- **TGDEDX**
This cut required that the range (rtg) and the energy (etg) in the target should satisfy the following conditions.
 - $rtg \leq 12.0$ cm,
 - $etg \leq 28.0$ MeV,
 - $etg \times 9.5 \leq rtg \times 28.0$, and
 - $etg \times 10.0 \geq (rtg - 2.0) \times 21.5$.

Bibliography

- [1] S. Weinberg, *Physica* **A96**, 327 (1979).
- [2] J. Gasser and H. Leutwyler, *Ann. Phys. (N.Y.)* **158**, 142 (1984).
- [3] J. Gasser and H. Leutwyler, *Nucl. Phys.* **B250**, 465 (1985).
- [4] J.F. Donoghue, E. Golowich, and B.R. Holstein, *Dynamics of the Standard Model* (Cambridge University Press, 1992), and references therein.
- [5] L. Maiani, G. Pancheri, and N. Paver, editors, *The DAΦNE Physics Handbook* (Laboratori Nazionali di Frascati, Frascati, 1992).
- [6] J.F. Donoghue and B.R. Holstein, *Phys. Rev.* **D40**, 3700 (1989).
- [7] B.R. Holstein, *Phys. Rev.* **D41**, 2829 (1990).
- [8] E. Fischbach and J. Smith, *Phys. Rev.* **184**, 1645 (1969).
- [9] H.W. Fearing, E. Fischbach, and J. Smith, *Phys. Rev. Lett.* **24**, 189 (1970).
- [10] H.W. Fearing, E. Fischbach, and J. Smith, *Phys. Rev.* **D2**, 542 (1970).
- [11] F.E. Low, *Phys. Rev.* **110**, 974 (1958).
- [12] S.L. Adler and Y. Dothan, *Phys. Rev.* **151**, 1267 (1966).
- [13] T.H. Burnett and N.M. Kroll, *Phys. Rev. Lett.* **20**, 86 (1968).
- [14] J. Bijnens, G. Ecker, and J. Gasser, in *DAΦNE Physics Handbook*, edited by L. Maiani, G. Pancheri, and N. Paver (Laboratori Nazionali di Frascati, Frascati, 1992).
- [15] J. Bijnens, G. Ecker, and J. Gasser, *Nucl. Phys. B* **396**, 81 (1993).
- [16] T.K. Komatsubara, E949 Technical Note K-048 (2005).
- [17] M.G. Doncel, *Phys. Lett.* **B32**, 623 (1970).
- [18] V.V. Braguta, A.A. Likhoded, and A.E. Chalov, *Phys. Rev.* **D65**, 054038 (2002).
- [19] J-L. Gervais, J. Iliopoulos, and J.M. Kaplan, *Phys. Lett.* **20**, 432 (1966).
- [20] V.V. Braguta, A.A. Likhoded, and A.E. Chalov, *Phys. Rev.* **D68**, 094008 (2003).
- [21] D. Ljung and D. Cline, *Phys. Rev.* **D8**, 1307 (1973).
- [22] O.G. Tchikilev *et al.*, arXiv:hep-ex/0506023, *Phys. Atom. Nucl.* **70**, 29 (2007).

- [23] Particle Data Group, C. Amsler *et al.*, Phys. Lett. **B667**, 1 (2008).
- [24] S. Shimizu *et al.*, Phys. Lett. **B633**, 190 (2006).
- [25] S. Adler *et al.*, Phys. Rev. Lett. **88**, 041803 (2002).
- [26] S. Adler *et al.*, Phys. Rev. **D77**, 052003 (2008).
- [27] M.S. Atiya *et al.*, Nucl. Instr. Meth. Phys. Res. **A321**, 129 (1992).
- [28] J. Doornbos *et al.*, Nucl. Instr. Meth. Phys. Res. **A444**, 546 (2000).
- [29] D.A. Bryman *et al.*, Nucl. Instr. Meth. Phys. Res. **A396**, 394 (1997).
- [30] M. Atiya *et al.*, Nucl. Instr. Meth. Phys. Res. **A279**, 180 (1989).
- [31] E.W. Blackmore *et al.*, Nucl. Instr. Meth. Phys. Res. **A404**, 295 (1998).
- [32] I-H. Chiang *et al.*, IEEE Trans. Nucl. Sci. **NS-42**, 394(1995).
- [33] T.K. Komatsubara *et al.*, Nucl. Instr. Meth. Phys. Res. **A404**, 315 (1998).
- [34] S. Kettel *et al.*, E787 Technical Note 314 (2000).
- [35] The EGS4 Code System, by W.R. Nelson, H. Hirayama, and D.W.O. Rogers, SLAC-265 (1985).
- [36] J.B. Birks, Proc. Phys. Soc. A64, 874 (1951).
- [37] M.M. Ito, E787 Technical Note 309 (1995).
- [38] A.G. Frodesen, O. Skjeggestad, and H.Tøfte, *Probabilty and statistics in particle physics* (Universitetsforlaget, Bergen, Norway, 1979).
- [39] R. Frühwirth, M. Regler, R.K. Bock, and H. Grote, *Data Analysis techniques for high-energy physics, Second edition* (Cambridge University Press, Cambridge, 2000).
- [40] S. Adler *et al.*, Phys. Rev. Lett. **85**, 4856 (2000).